Airbursts and Cratering Impacts

2026 | Volume 4 | Pages: 1–56 | e-location ID: e20260007
DOI: 10.14293/ACI.2026.0007



Research Article

Platinum-group elements, shocked quartz, and nanodiamonds in a Greenland ice-margin sequence at the Younger Dryas onset

James P. Kennett[1], Paul A. Mayewski[2], Andrei V. Kurbatov[2], Wendy S. Wolbach[3], Douglas C. Introne[4], Michael Handley[2], Malcolm A. LeCompte[5], Christopher R. Moore[6,7]*, Gunther Kletetschka[8,9], A. Victor Adedeji[10], Joshua J. Razink[11], Julie E. Chouinard[11], Jesus Paulo Perez[12], Brian van Devener[12], Randy C. Polson[12], Tim Witwer[13], Teresa M. Eaton[14], Matthew J. Valente[15], David B. Lanning[16], Yoav Rapoport[14], Kailey Ellison[14], Argyro Reyes[14], Ravi Holladay[14], Michelle Madrigal[14], Julian Albanil[14], Charlie Sanchez[14], Ileana Banatlao[14], Dallas H. Abbott[17], Allen West[13,*], Marc J. Defant[18], Mahbub Alam[19] and Mohammed Baalousha[19]

[1]Department of Earth Science and Marine Science Institute, University of California, Santa Barbara, Santa Barbara, CA 93106, USA; [2]Climate Change Institute, University of Maine, Orono, ME 04469-5790, USA; [3]Department of Chemistry and Biochemistry, DePaul University, Chicago, IL 60614, USA; [4]Stable Isotope Laboratory, University of Maine, Orono, ME 04469-5790, USA; [5]Elizabeth City State University, Center of Excellence in Remote Sensing Education and Research, Elizabeth City, NC 27909, USA; [6]South Carolina Institute of Archaeology and Anthropology, University of South Carolina, Columbia, SC 29208, USA; [7]SCDNR Heritage Trust Program, Land, Water, and Conservation Division, South Carolina Department of Natural Resources, Columbia, SC 29208, USA; [8]Geophysical Institute, University of Alaska, Fairbanks, AK 99775, USA; [9]Faculty of Science, Charles University, Albertov 6, Prague 12843, Czech Republic; [10]Department of Natural Sciences, Elizabeth City State University, Elizabeth City, NC, 27909, USA; [11]CAMCOR, University of Oregon, 1443 E 13th Ave, Eugene, OR 97403, USA; [12]Electron Microscopy and Surface Analysis Lab, Nanofab, University of Utah, Salt Lake City, UT 84112, USA; [13]Comet Research Group, Prescott, AZ 86301, USA; [14]Department of Biology and Chemistry, College of Arts & Sciences, Embry-Riddle University, Prescott, AZ 86301, USA; [15]Life Sciences Departments, Harford Community College, Bel Air, MD 21015, USA; [16]Department of Aerospace Engineering, College of Engineering, Embry-Riddle University, Prescott, AZ 86301, USA; [17]Lamont Doherty Earth Observatory of Columbia University, Palisades, NY 10964, USA; [18]School of Geosciences, University of South Florida, Tampa, FL 33620, USA; [19]Center for Environmental Nanoscience and Risk (CENR), Department of Environmental Health Sciences, Arnold School of Public Health, University of South Carolina, Columbia, SC 29208, USA

*Correspondence to: Christopher R. Moore, E-mail: moorecr@mailbox.sc.edu; Allen West, E-mail: allen7633@aol.com

Received: 7 April 2026; Revised: 7 April 2026; Accepted: 1 May 2026; Published online: 30 May 2026

How to cite: Kennett J.P., et al. Platinum-group elements, shocked quartz, and nanodiamonds in a Greenland ice-margin sequence at the Younger Dryas onset. *Airbursts and Cratering Impacts*. 2026 | Volume 4 | Issue 1 | Pages: 1–56 | DOI: 10.14293/ACI.2026.0007

ABSTRACT

Here, we present a multidisciplinary investigation of a late-Pleistocene Greenland ice-margin sequence near Kangerlussuaq that spans the Bølling-Allerød, Younger Dryas, and early Holocene. This study investigates the cause of the Younger Dryas (YD) cooling event (~12,800 years ago) and its possible relationship to a cosmic impact. The Kangerlussuaq interval was previously identified using visible dust stratigraphy, oxygen-isotope measurements, and a peak in nanocarbon particles interpreted as nanodiamonds. We expand that record using bulk ICP-MS, single-particle

© 2026 The Author(s). This work has been published open access under Creative Commons Attribution License CC BY 4.0 https://creativecommons.org/licenses/by/4.0/, which permits unrestricted use, distribution and reproduction in any medium, provided the original work is properly cited. Conditions, terms of use and publishing policy can be found at www.scienceopen.com.

ICP-time-of-flight mass spectrometry (SP-ICP-TOF-MS), microscopy, mineralogical observations, and hydrocode modeling. The Kangerlussuaq sequence preserves a dark, dust-rich YD interval bounded by clearer Holocene and Bølling-Allerød ice. Stable $\delta^{18}O$ values and dust-related geochemical changes support correlation of this interval with the YD cooling episode, although the ice-margin setting introduces uncertainties related to compression, ablation, meltwater infiltration, and multi-season sample alignment. Within this framework, the Greenland record resolves three superimposed signals. First, bulk geochemistry and nanoparticle mineral-phase associations document a sustained YD-scale reorganization of atmospheric dust provenance and transport, consistent with colder, drier, and windier conditions and enhanced mineral-dust flux throughout much of the ~1,200–1,300-year YD interval. Second, a narrow proxy-rich horizon at the YDB layer (~5.5 m along the sloping ice) contains peak abundances of multiple particulate proxies, including nanocarbon particles previously interpreted as nanodiamonds, quartz grains with shocked planar microstructures, meltglass, glass-filled lithic aggregates, Fe- and Si-rich spherules, carbon-rich spherules, glasslike carbon, charcoal, and soot. Third, nanoparticle concentrations begin to rise at the YDB layer (~5.5 m), marking the onset of enrichment, but reach their maximum immediately above, at ~5.2 m. SP-ICP-TOF-MS identifies this overlying interval as the peak in nanoparticle-scale terrestrial and siderophile components, including Nb, Ta, U, As, Pb, Sb, PGEs, Ni, Co, and Re. Elemental behavior across the nanoparticle dataset can be grouped into three principal populations: climate-driven terrestrial mineral dust, high-temperature plume-derived possible ET condensates, and lower-temperature terrestrial plume derivatives. This offset between the boundary layer and the nanoparticle maximum is a key observation: concentrations are lowest within the YDB layer, increase at the boundary, and peak in the overlying sample, indicating temporally structured deposition involving initial boundary-layer input followed by delayed fallout or redistribution of fine particles. This delay is supported by independent evidence from the GISP2 ice core of a platinum anomaly coincident with the onset of Younger Dryas climate change, including a delayed peak over ~21 years, supporting non-instantaneous deposition of impact-related material and suggesting a temporal link to YD climate change. The PGE-bearing nanoparticle population provides the strongest geochemical evidence for a non-crustal contribution. At ~5.2 m, PGE sum, Ir, Pt, Os, Pd, Ni, Co, and Re are enriched relative to the YDB layer; these elements are strongly enriched in extraterrestrial (ET) materials relative to crustal abundances, suggesting a non-terrestrial source. Ratio-ratio diagrams and PGE fractionation versus Ir/Fe comparisons indicate that the YDB nanoparticle population is compositionally distinct from Greenland background dust and typical terrestrial reservoirs. The Greenland YDB value of (Os+Ir+Ru)/(Rh+Pd+Pt) is sub-chondritic, while Ir/Fe is highly elevated, consistent with a heterogeneous mixture containing a refractory PGE-rich component, possibly from ET refractory metal nuggets (RMNs), together with more volatile PGE-bearing material. This signature does not match any single impactor class (e.g., bulk chondrite, iron meteorite, or achondrite), but is consistent with a mixed, fractionated nanoparticle population superimposed on background cosmic dust influx. Hydrocode modeling demonstrates that a high-velocity impact or airburst interacting with an ice-sheet target can plausibly generate high pressures, elevated temperatures, shocked quartz, melt products, spherules, and widespread nanoparticle dispersal; however, this modeling is intended to illustrate a viable mechanism for proxy formation and does not imply that such an impact occurred at the Greenland site. Instead, these results are consistent with broader Younger Dryas Impact Hypothesis scenarios involving regionally or globally distributed impact and airburst phenomena. The combined proxy assemblage is difficult to explain by volcanism, biomass burning, authigenesis, anthropogenic contamination, or climate-driven dust deposition alone. No single proxy is uniquely diagnostic of impact; rather, the interpretation rests on the stratigraphic co-occurrence of multiple high-temperature, shocked, carbonaceous, siderophile-enriched, and PGE-bearing materials within the YD onset interval. Together, the Greenland record is consistent with a short-duration, high-energy airburst or impact-related depositional episode superimposed on and possibly a major trigger of the broader climatic transition into the Younger Dryas.

KEYWORDS

Younger Dryas, Greenland, platinum-group elements, shocked quartz, nanodiamonds, extraterrestrial impact, airburst, Glacial ice-margin stratigraphy, Kangerlussuaq

Introduction

The Younger Dryas (YD) marks a major and abrupt climatic reversal at the end of the Pleistocene, interrupting the final phase of the last deglaciation. Beginning at approximately 12.9 ka and persisting for ~1,200–1,300 years, the event followed rapid warming during the Bølling-Allerød interstadial and was characterized by a sudden return to colder conditions

across much of the Northern Hemisphere. Temperature declines of ~5–10 °C in Greenland and the North Atlantic were accompanied by widespread environmental reorganization [1, 2]. In Greenland ice-core stratigraphy, this interval is designated Greenland Stadial 1 (GS-1) and is marked by abrupt shifts in $\delta^{18}O$ values, increased dust concentrations, and changes in atmospheric circulation.

Within the broader context of late-glacial climate variability, the Younger Dryas represents the final and most recent of a series of abrupt stadial events that punctuated the last glacial period, many of which are associated with Heinrich events and millennial-scale reorganizations of North Atlantic circulation. These stadials are characterized by rapid cooling onsets, enhanced ice-rafted debris, and reduced Atlantic Meridional Overturning Circulation (AMOC), reflecting the sensitivity of the climate system to freshwater forcing and ocean-atmosphere feedbacks [3–7]. Climatic impacts associated with the YD include a pronounced weakening of the AMOC, expansion of North Atlantic sea ice, southward displacement of the Intertropical Convergence Zone, and reorganized mid-latitude and polar atmospheric circulation [7, 8]. Notably, while the Northern Hemisphere experienced strong cooling, many Southern Hemisphere records indicate contemporaneous warming, consistent with a bipolar seesaw response to reduced northward heat transport and further implicating large-scale ocean circulation changes as a central component of the event [9, 10].

Both the onset and termination of the Younger Dryas were extremely abrupt. High-resolution Greenland ice-core records constrain the boundaries of GS-1 to decadal or sub-decadal timescales, and precisely dated speleothem records from Europe confirm near-synchronicity of the transition across much of the North Atlantic region [11–14]. The rapid warming at the end of the YD underscores the nonlinear nature of the climate system and the role of threshold behavior in glacial-interglacial transitions.

Despite broad agreement on the magnitude, timing, and widespread expression of Younger Dryas climate change, the mechanism responsible for initiating this abrupt cooling remains unresolved. The most widely accepted explanation invokes freshwater forcing of the North Atlantic, through meltwater discharge or rerouting from retreating Laurentide and/or Fennoscandian ice sheets, leading to suppressed deep-water formation and AMOC weakening [5, 15]. Alternative hypotheses include volcanic forcing, large Northern Hemisphere eruptions capable of producing short-lived radiative cooling, followed by longer-term feedbacks involving sea ice and ocean circulation [14], as well as a proposed extraterrestrial airburst or impact event near the YD onset, inferred from a distinctive suite of geochemical and mineralogical proxies reported at multiple sites [16–18].

In this context, Greenland ice occupies a uniquely important position in evaluating competing hypotheses for the Younger Dryas onset, because it preserves annually to decadally resolved records of atmospheric composition, dust loading, and geochemical anomalies directly linked to climate transitions. Earlier work by Kurbatov et al. [19] identified several key impact-inferred proxies in a stratigraphically discrete Younger Dryas boundary layer in Greenland ice; this study investigates whether a broader suite of impact-related proxies is preserved at this key climatic transition.

In 1992, Yates et al. [20] reported carbon-isotopic signatures in acid-resistant residues from Greenland cryoconite that were interpreted as consistent with a minor presolar diamond component; however, the nanodiamonds were identified only indirectly. In 2010, Kurbatov et al. [19] reported a stratigraphically discrete layer enriched in nanocarbon particles interpreted as nanodiamonds in Greenland ice, representing the earliest reported occurrence of free NDs preserved within glacial ice and providing initial evidence consistent with a high-energy extraterrestrial (ET) airburst or impact near the Younger Dryas (YD) onset.

The present investigation significantly extends the results of a previous study [19] on a late-glacial to early-Holocene stratigraphic sequence along the West Greenland ice margin near Kangerlussuaq, sampled during expeditions from 2008 to 2014. Stable-oxygen-isotope profiles and dust stratigraphy indicate that the ND-bearing layer dates close to the onset of the Younger Dryas cooling episode at ~12,800 ± 100 cal BP [19, 21, 22].

A previous study (Kurbatov et al.) [19] reported sharply defined peaks in particles interpreted as cubic nanodiamonds, *n*-diamonds, and lonsdaleite with abundances up to ~5×10^6 over background. Kinzie et al. [23] reported similar observations using comparable analytical approaches; however, these identifications and abundance estimates have been challenged in the literature. The reported 2–40 nm grain sizes and commonly rounded morphologies of these particles are consistent with high-temperature formation processes; however, such morphologies are not diagnostic and can arise from multiple formation and alteration pathways [24, 25]. Lonsdaleite has been widely reported in association with hypervelocity impact processes, although its occurrence and diagnostic significance remain debated in some contexts [26, 27]. These results are consistent with the hypothesis of a multi-continental ET airburst/impact near the YD onset [16, 28–31], but do not uniquely require one.

Similar assemblages of nanocarbon particles interpreted as nanodiamonds, shocked quartz, and other impact-related proxies have been reported at numerous YDB sites on four continents, although several of these identifications and their interpretations remain debated. Figure 1 compares ten principal YDB proxies across nineteen sites [16, 18, 23, 32–60]. For context, Figure 1 also compares these proxies with those from confirmed or widely accepted impact-related events, including Chicxulub and the Ries crater, as well as the Australasian tektite field and the Libyan Desert glass field, which are widely discussed in the context of impact-related processes. The number of proxies reported at many YDB sites is comparable to or exceeds that reported for these accepted

YDB SITES (26)	Country	Modeled ages	Uncertainty (68%)	Dark Impact Layer	Nanodiamonds	Shocked Quartz	Meltglass	Fe, Si Spherules	Carbon Spherules	Glasslike Carbon	Charcoal / Soot	PGEs, Ni, Co, Cr	Crater	TOTALS
Kangerlussuaq	DEN	12800	50	•	•	•	•	•	•	•	•	•		9
Alsterhut	NETH	12780	35	•		•					•			3
Abu Hureyra	SYRIA	12825	55	•	•	•	•	•	•	•	•	•		9
Arlington Cyn	US, CA	12805	55	•	•	•	•	•	•	•	•	•		9
Blackville	US, SC	12820	1080	•	•	•	•	•	•	•	•	•		9
Blackwater Draw	US, NM	12775	365	•		•		•		•	•	•		6
Bowser Road	US, NY	12868	--	•	•	•	•	•	•	•	•	•		9
Flamingo Bay	US, SC	~12,800	--	•		•		•				•		4
Guil-Mt.Viso	FR/ITAL	12787	34	•		•		•	•	•		•		7
Halls Cave	US, TX	12873	55	•	•	•	•	•	•	•	•	•		9
Lingen	GERM	12735	85	•	•	•		•	•	•	•			7
Lommel	BELG	12735	790	•	•	•	•	•	•	•	•			7
Mucunuque	VENEZ	12787	34	•		•	•	•	•			•		7
Murray Spgs	US, AZ	12750	235	•	•	•	•	•	•	•	•	•		9
Ossendrecht	NETH	~13050	--	•		•	•		•	•	•			6
Parsons Island	US, MD	12731	14	•		•	•	•				•		5
Perkins	US, LA	12794	69	•		•	•	•	•	•	•	•	•	9
Pilauco	CHILE	12770	160	•		•	•	•	•	•	•	•		8
UP-Newtonville	US, NJ	12783	29	•	•	•	•	•	•	•	•	•		9
TOTALS		12770		19	10	19	14	17	15	15	17	15	1	
Chiczulub (K-Pg)	MEX	65 Ma	--	•	•	•	•	•	•	•	•	•	•	10
Ries Crater	GERM	14.8 Ma	--	•	•	•	•	•				•	•	7
Australasian tektites	SE ASIA	790 ka	--	•		•	•	•				•		5
Libyan Desert glass	EGYPT	29 Ma	--			•	•	•				•		4

Figure 1: Reported YDB proxy assemblages compared with selected accepted impact events. The Kangerlussuaq ice-margin sequence contains most of the proxy classes reported at other YDB sites, as well as four accepted impact craters.

events, although the identification and interpretation of some proxy classes remain subjects of ongoing debate.

The Younger Dryas Impact Hypothesis has been extensively debated, and its principal criticisms have been addressed in prior publications. Rather than revisiting those arguments here, we focus on presenting new observational and geochemical constraints from the Greenland ice-margin record. Although the Younger Dryas Impact Hypothesis (YDIH) has been criticized for, among other things, the absence of a confirmed crater [61, 62], six candidate end-Pleistocene craters have been proposed with ages that overlap the YDB: Corossol, Canada [63]; Charity Shoal, Canada [16, 64]; Bloody Creek, Canada [65]; Brushy Creek, Louisiana, USA [66]; Perkins, Louisiana, USA [57]; and the Iturralde, Bolivia [67]. Though the ages of these crater candidates remain uncertain and continue to be debated, some are independently proposed to be YDB-aged and if confirmed, they are consistent with multiple coeval small impacts, as predicted by the YDIH. In any event, the lack of a confirmed crater does not preclude an impact origin, as both the Australasian tektite field and the Libyan Desert glass field are often interpreted as evidence of an impact event, currently lack a confirmed source crater [68, 69].

The particles interpreted as nanodiamonds at Kangerlussuaq exhibit morphologies, reported polytypes, and Raman signatures that have been compared with those described for YDB sites globally and at the Cretaceous-Paleogene boundary [70, 71]. However, such identifications remain subject to

analytical uncertainty. Background ND abundances in adjacent ice are orders of magnitude lower, underscoring the layer's uniqueness. The nanodiamond-like particles previously reported by Kurbatov et al. [19] represent a proposed early occurrence of such materials in polar or alpine ice, although their identification remains debated.

In addition, the quartz grains reported here exhibit microstructural features interpreted as shock-related (e.g., planar deformation features and planar fractures), although such identifications require careful distinction from non-shock planar structures. Because planar features in quartz can also arise from tectonic deformation, diagenesis, or sample preparation, identification of shock-related features requires crystallographic orientation analysis and multiple sets of planar deformation features. Interpretations presented here are, therefore, based on features consistent with shock metamorphism rather than other formation mechanisms. Their presence is consistent with aerial transport and deposition, potentially preserving an atmospheric record of particulate input associated with high-temperature or high-energy processes. They may represent an instance of shocked quartz grains preserved directly within glacial ice following atmospheric transport and deposition, rather than through incorporation into sedimentary deposits. This differs from reports associated with the Hiawatha structure, where shocked quartz has been recovered only from glaciofluvial sediments [72, 73].

Together, the stratigraphically discrete nanocarbon particles interpreted as nanodiamonds, shocked quartz, and associated proxies preserved in Greenland ice provide evidence consistent with a brief, high-energy event at the Younger Dryas onset, although the origin and interpretation of some proxy classes remain debated.

Nineteen sites exhibit the YDB layer containing 10 reported proxies, including nanocarbon particles interpreted as nanodiamonds, shocked quartz, meltglass, Fe- and Si-rich spherules, carbon spherules, glasslike carbon, charcoal/soot, a dark post-impact layer, PGEs with Ni and Co, and one proposed crater [57].

The YDB Greenland ice at Kangerlussuaq contains 9 of these 10 proxies, with only a confirmed crater missing. The Greenland site preserves a broad suite of proxies reported from other YDB sites on four continents. The average YDB age for the 19 sites is 12,770 cal BP, and all fall within the proposed YD impact age range of 12,850–12,750 cal BP [17]. The 19 YDB sites exhibit as many or more impact proxies that have been reported for the four other widely accepted impact-related events, including the K-Pg Chicxulub crater. Each proxy is consistent with elevated-temperature processes, and their co-occurrence within a narrow stratigraphic interval is characteristic of impact-related assemblages.

Ice sampling during multiple field expeditions

Several expeditions relevant to this investigation were conducted within a few hundred meters of one another at the same ice-margin location east of Kangerlussuaq at 67.156361° N, 50.023278° W (Figure 2).

In 2008, 2009, 2014, and 2017, we collected ice samples from a sloping exposure of late-glacial to early Holocene ice

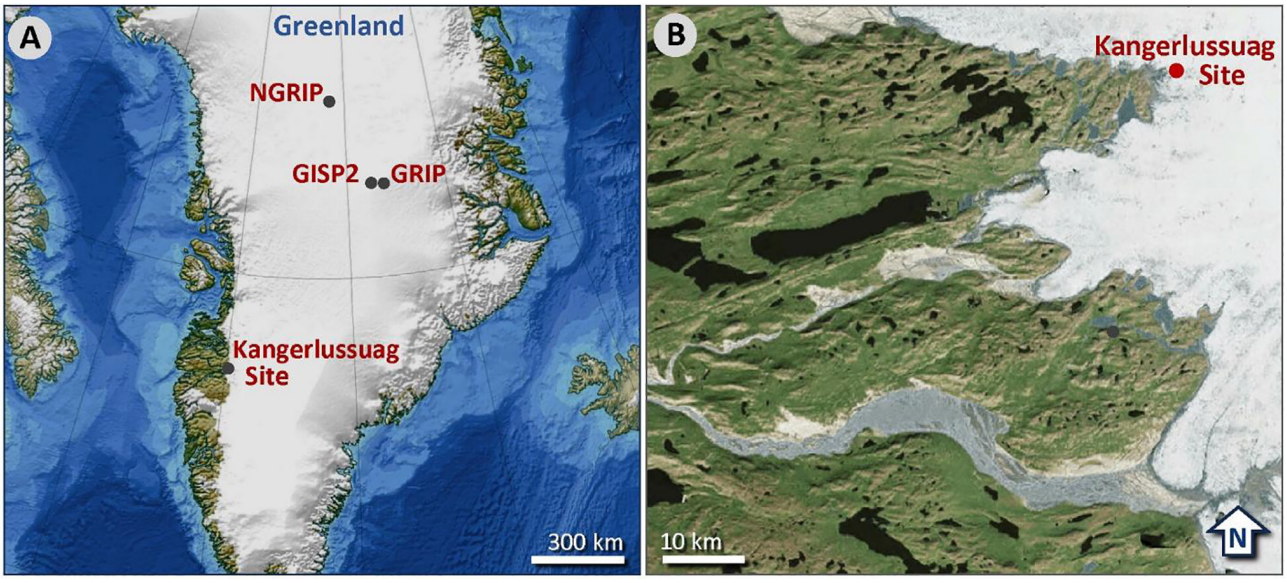


Figure 2: Location of the Kangerlussuaq site. (A) The Kangerlussuaq sampling site is located on the ice-sheet margin, 166 km inland from the west coast of Greenland. Also shown are the deep ice core sites of GISP2, GRIP, and NGRIP. Image modified from Uwe Dedering, 2010, Wikipedia.com, usable under the Creative Commons Attribution-Share Alike 3.0 license. (B) Satellite image of the Kangerlussuaq sampling site at the western Greenland ice margin. Panel B adapted from Yde, 2018 [74], usable under Creative Commons 4.0 International.

near Kangerlussuaq, West Greenland (Figure 2). The section lies along the western margin of the Greenland Ice Sheet (GIS), approximately 166 km from the coast, and exposes alternating dust-rich and relatively dust-poor layers that have been used previously to identify the Bølling-Allerød (BA), Younger Dryas (YD), and early Holocene climatic intervals [19, 21, 22].

Because direct absolute dating is not possible at ice-margin exposures, stratigraphic attribution relies on correlation with dated Greenland ice-core records using multiple lines of evidence, including ice-layer structure, dust stratigraphy, $\delta^{18}O$ trends, and geochemical markers rather than any single proxy alone. The exposed profile contains a visually prominent, darker, dust-rich layer that correlates with the previously described Younger Dryas boundary (YDB) layer [19].

Sampling was conducted along the cleanest available exposures, avoiding meltwater channels, fractures, and modern surface contamination. Ice blocks were excavated, sealed in clean polyethylene bags, and maintained frozen during transport. One sample at the top of the sequence exhibited clear evidence of contamination from meltwater infiltration along fractures and was excluded from all nanoparticle calculations to avoid biasing the results.

Because sampling was conducted over multiple field seasons along a retreating ice-margin exposure, no fixed physical datum exists from which to measure slope distance. As a result, the absolute distance scales of the three independently collected sample sets differed. To enable direct comparison, all datasets were aligned using internal stratigraphic markers. Specifically, the onset of the Younger Dryas, expressed as a coupled shift in $\delta^{18}O$ values and dust-related geochemical signals, was used to define a common reference horizon extending across the full YD interval. Following alignment, residual positional uncertainty is estimated at ≤ 5 cm, smaller than the 15-cm sampling interval, and does not affect identification of the principal stratigraphic features discussed here, including the position and relative offset of peak nanoparticle concentrations. Although local deformation, ablation, and meltwater infiltration can modify $\delta^{18}O$ and dust stratigraphy, interpretation is based on the primary transition signal rather than fine-scale variability. Accordingly, interpretations emphasize stratigraphic clustering and multiproxy co-occurrence rather than precise centimeter-scale alignment.

Samples were collected at 15-cm intervals along the exposure, corresponding to ~180–200 years per sample based on correlations with the GISP2 core and published age models [21, 22]. This resolution captures multi-decadal to centennial-scale variability but does not resolve sub-decadal events; thus, the YDB layer represents an integrated signal over multiple decades rather than a single depositional year and, therefore, does not resolve deposition at annual or sub-annual timescales.

In the laboratory, ice samples were melted in acid-cleaned containers under HEPA-filtered conditions. Dust fractions were isolated by filtration and analyzed using bulk geochemical methods, single-particle inductively coupled plasma time-of-flight mass spectrometry (SP-ICP-TOF-MS), microscopy, and mineralogical techniques, as described below. Aliquots of meltwater were retained for stable isotope analysis.

Sampling across multiple expeditions contributed complementary datasets. Initial collections in 2008 included ice for ICP-MS and $\delta^{18}O$ measurements, as well as large blocks for analysis of impact-related proxies. Additional sampling in late 2008 and 2009 expanded elemental and isotopic coverage. Higher-resolution trench sampling in 2014 enabled laser ablation ICP-MS analyses, and a short core retrieved in 2017 further improved stratigraphic resolution. Together, these datasets provide a consistent and internally correlated record across the studied interval.

Primary objectives and analytical framework

This study reevaluates and expands upon earlier evidence reported from the Greenland Ice Sheet by Kurbatov et al. [19] for a potential cosmic impact event at the onset of the Younger Dryas (YD) by applying a broader suite of YDB impact-related proxies now recognized at more than 50 sites worldwide. The objectives are to: (i) refine the chronology of the Younger Dryas boundary (YDB) layer using stable oxygen-isotope ($\delta^{18}O$) profiles and dust stratigraphy; and (ii) determine whether the ice samples at Kangerlussuaq display the same proposed impact-related proxies as found at other YDB sites, including shocked quartz, nanodiamonds, melt-glass, microspherules, platinum-group elements (PGEs), glass-filled fractured quartz grains, carbon spherules, and glasslike carbon; and (iii) if so, whether these proxies constitute robust evidence for a high-energy airburst or impact event synchronous with the onset of the YD.

Results and interpretations

The proxies examined in this study can be grouped into three functional categories: (a) stratigraphic and chronological markers (e.g., $\delta^{18}O$ and dust stratigraphy), (b) high-temperature and impact-related particulate proxies, and (c) ancillary geochemical indicators that constrain depositional conditions and post-depositional processes. This organization highlights the primary line of argument, in which a stratigraphically confined suite of impact-related proxies occurs within the Younger Dryas onset interval, independently defined by ice-core climate markers.

Identification of Younger Dryas interval using dust geochemistry

The onset of the Younger Dryas (YD) marks an abrupt climatic reversal near the end of the Pleistocene, characterized by a rapid return to colder and drier conditions in the Northern Hemisphere and by increased wind strength over

Greenland [75, 76]. A prominent stratigraphic expression of this interval in Greenland ice cores is the darker, dust-enriched layer produced by intensified atmospheric circulation and enhanced aridity in distal dust-source regions [75, 76].

At the Pakitsoq site north of Kangerlussuaq, Petrenko et al. [77] identified YD-age ice, while Reeh et al. [78] documented YD layers at 15 ice-margin localities around Greenland.

A comparable stratigraphic sequence is present at Kangerlussuaq (Figure 3), where the YD layer appears as a darker, dust-rich interval between lighter Holocene and BA ice. This visual contrast has been interpreted as reflecting enhanced aeolian deposition during the YD, associated with increased wind intensity and arid conditions [19, 45, 76, 79]. Such stratigraphic markers provide consistent visual criteria for locating YD-age ice across multiple Greenland sites. Another site, at Kronprins Christian Land in northeastern Greenland, displays a similar visually distinct, darker, dust-rich YD layer directly above relatively dust-free Bølling-Allerød (BA) ice and below colder, dustier end-glacial ice. Overlying the YD layer is clearer, low-dust Holocene ice [78, 80] (Figure 4).

Younger Dryas identification using oxygen isotope stratigraphy ($\delta^{18}O$)

Significant environmental, biotic, and atmospheric changes accompanied the onset of the Younger Dryas (YD). In Greenland and northwestern Europe, this transition is characterized by an abrupt temperature decline of approximately 5–10 °C [5, 7]. To assist in locating the YD onset within the Kangerlussuaq sequence, we examined stratigraphic shifts in $\delta^{18}O$ values from ice samples collected in 2008 (Figure 5). Because $\delta^{18}O$ serves as an established proxy for past temperature variability, these measurements provide an independent means of identifying major climatic transitions. The Kangerlussuaq $\delta^{18}O$ profile was then compared with published records from the GISP2, GRIP, and NGRIP ice cores [11, 81], which offer well-constrained reference frameworks for Greenland paleoclimatic stratigraphy.

Interpretation. The $\delta^{18}O$ profiles from Kangerlussuaq and the three Greenland ice cores all show a distinct negative shift at the inferred onset of the Younger Dryas (YD), consistent with a rapid regional cooling. This isotopic excursion is a well-established indicator of an abrupt temperature decline and is consistent with field observations suggesting that the darker ice layer at Kangerlussuaq corresponds to the YD interval [19].

In the Kangerlussuaq sequence (Figure 5A), a brief return to less negative $\delta^{18}O$ values appears at ~5 m depth within the mid-interval of the YD episode preserved in this section. Because this interval displays no geochemical changes, this feature is likely an artifact rather than a genuine climatic fluctuation. We evaluate implications of these site-specific uncertainties for duration and synchronicity in the Discussion. Numerous surface cracks were noted during sample collection, suggesting localized Holocene meltwater infiltration, a process previously documented at this site [19]. Refreezing of such water within older layers would elevate

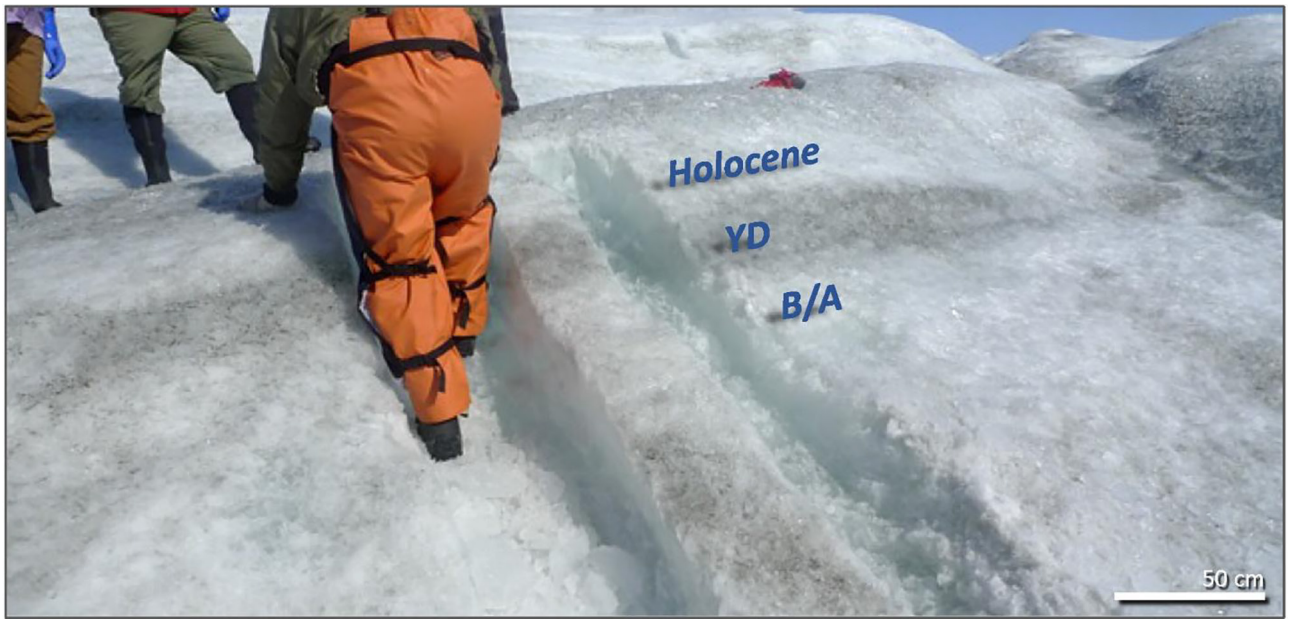


Figure 3: Visible ice layering at Kangerlussuaq. Photograph of the 2008 Kangerlussuaq ice sampling site showing stratigraphic layers: clear Holocene (top), a dark dust-rich YD layer (middle), and clear Bølling-Allerød Interstadial ice (bottom). The Younger Dryas boundary (YDB) is placed at the base of the dark dust band.

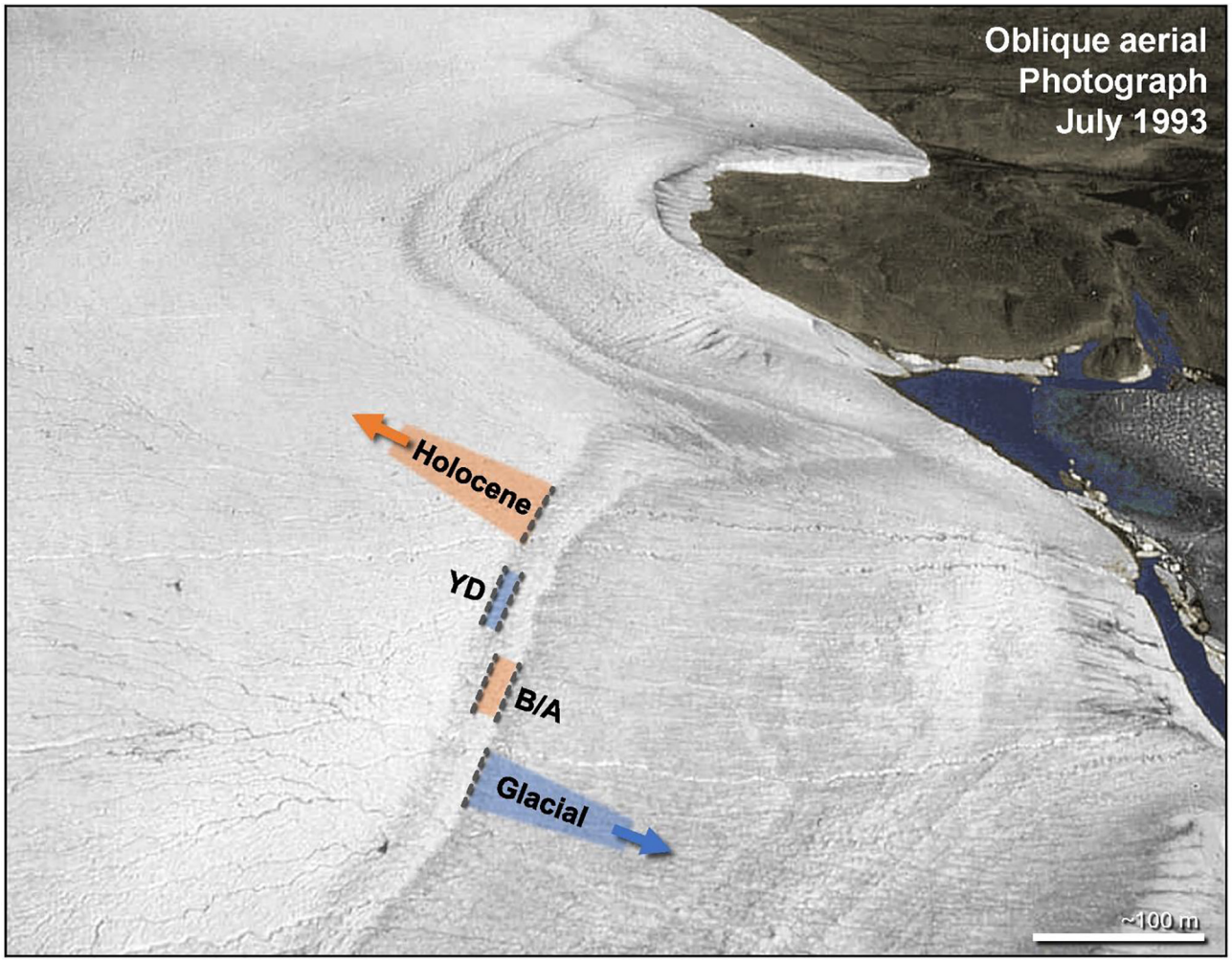


Figure 4: Kronprins Christian Land, NE Greenland, shows a darker YD layer. This aerial photograph of the ice sheet in Kronprins Christian Land shows a stratigraphy of ice layers from the warmer Holocene (top), the colder YD (dark dust-rich middle layer), the warmer Bølling-Allerød Interstadial (lighter ice below the YD), and the colder glacial interval (very thick, darker dust-rich bottom layer). The sequence is similar, although much thicker than the Kangerlussuaq sequence. Credit: H. Oerter [78, 80], usable under Creative Commons 4.0.

$\delta^{18}O$ values, producing an apparent warming signal despite careful efforts to minimize sampling of compromised ice. In addition, $\delta^{18}O$ values in the Kangerlussuaq YD interval are generally less negative than those from higher-elevation cores on the ice-sheet plateau. This difference may reflect a combination of post-depositional isotopic diffusion and fractionation [82], infiltration and refreezing of isotopically heavier meltwater, and the effects of initial deposition at lower elevation, followed by lateral ice transport toward the margin.

Despite these complexities, the amplitude and direction of the $\delta^{18}O$ change across the YD interval preserved at Kangerlussuaq closely parallel those in GISP2, GRIP, and NGRIP. This correspondence is consistent with the interpretation that the dark, dust-rich ice layer at Kangerlussuaq represents the Younger Dryas cooling episode and its basal contact, the Younger Dryas Boundary (YDB).

Geochemical changes in dust across the Younger Dryas boundary

We further evaluated whether the dust-rich ice layer at Kangerlussuaq corresponds to the Younger Dryas (YD) interval by examining geochemical evidence for changes in atmospheric dust composition and provenance across the transition. Specifically, we assessed three complementary lines of evidence: (1) climate-driven shifts in dust provenance associated with intensified winds and aridity that began at the onset of the YD and persisted ~1,200–1,300 years until its end; (2) short-lived compositional changes reflecting increased entrainment of terrestrial sediments into the atmosphere; and (3) short-lived potential contributions from non-terrestrial material introduced during a high-energy event. This framework allows us to distinguish between background, climate-controlled variations in dust flux and composition and any superimposed geochemical anomalies

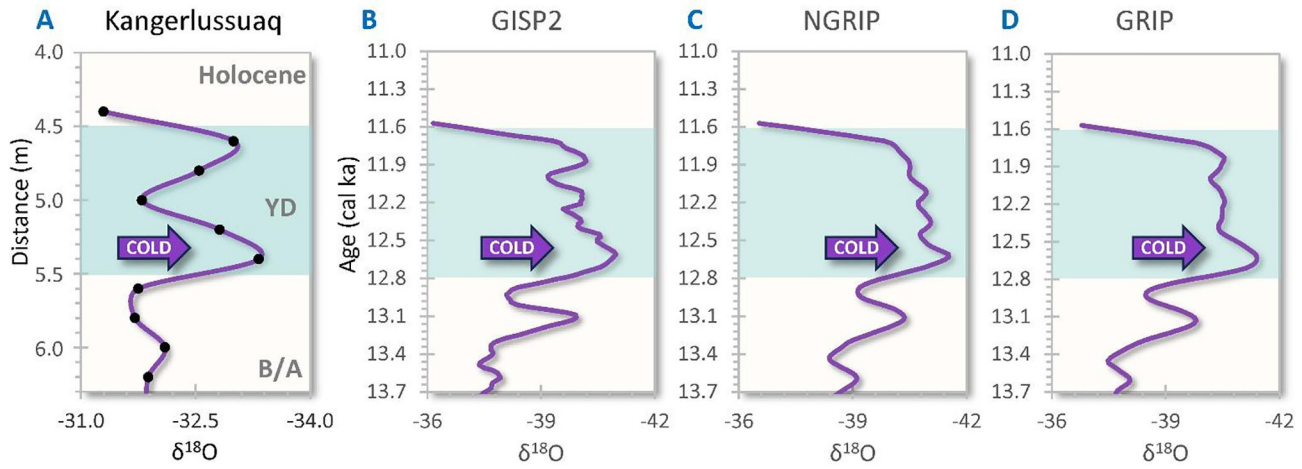


Figure 5: $\delta^{18}O$ values from ice in four Greenland sites. (A) $\delta^{18}O$ values by age from the Kangerlussuaq ice-margin section. (B) $\delta^{18}O$ values by age from the GISP2 core. (C) $\delta^{18}O$ values by age from the NGRIP core. (D) $\delta^{18}O$ values by age from the GRIP core. GISP2, GRIP, and NGRIP data from Rasmussen et al. [11]. For Kangerlussuaq, (A) $\delta^{18}O$ values are plotted as a function of slope distance along the ice surface, as first reported by Kurbatov et al. [19]. Because the slope distances to the inferred YD layer varied across multiple expeditions, we use a generalized scale that places the lower boundary of the YD episode at 5.5 m and the upper boundary at 4.5 m, representing the slope distance from an arbitrary point on the Holocene ice.

that may reflect additional inputs or processes operating at the YD boundary.

First, we conducted a detailed elemental analysis of ice samples using inductively coupled plasma mass spectrometry (ICP-MS). The resulting geochemical profiles (Figure 6) were compared with equivalent datasets from the well-documented GISP2 ice core [76, 83].

Elemental ratios (Figure 6A, B), particularly potassium-to-calcium (K/Ca), were used as indicators of dust provenance and transport intensity. Additional ratios, including La/Ca, Cs/Ca, As/Ca, Zn/Ca, Sr/Ca, and Na/Ca, were measured to assess compositional variations across the inferred YD onset and to investigate potential changes in atmospheric circulation, weathering regimes, and source-region contributions during this climatic transition. The primary results are shown in Figure 6. Selected PGEs and Zn are normalized to Ca and to each other in SI, Figure S1. Full ICP-MS datasets are provided in SI, Table S1.

Interpretation. Systematic changes in elemental ratios across the transition from the Bølling-Allerød (BA) to the lower Younger Dryas (YD) indicate shifts in the composition and provenance of atmospheric dust reaching the Kangerlussuaq site. Declines in K/Ca, La/Ca, and Cs/Ca at the YD onset suggest a reduced contribution from alkali-rich, chemically weathered continental materials typically associated with mature soils and sedimentary sources. The similarity of these trends to those in the GISP2 core is consistent with both the proposed stratigraphic correlation and the regional expression of this geochemical pattern.

In contrast, increases in As/Ca, Zn/Ca, Sr/Ca, and Na/Ca during the YD imply the involvement of additional or shifting source regions. Elevated Na/Ca and Sr/Ca values are consistent with greater inputs of marine-derived aerosol, potentially reflecting changes in storm frequency or sea-ice conditions, while higher As/Ca and Zn/Ca ratios may indicate enhanced contributions from volcanic emissions, intensified rock weathering, or altered long-distance transport pathways. The relatively sharp boundaries at the BA-YD transition suggest a rapid reorganization of the atmospheric circulation rather than a gradual, progressive climatic shift.

Other elemental mass ratios measured by ICP-MS, including Pt/Ca, Ir/Ca, Ru/Ca, Zn/Ca, and inter-element ratios such as Pt/Pd, Ir/Pt, Pt/Ru, and Pt/Rh (SI, Figure S3), exhibit broad peaks beginning near the YD onset and extending through part of the interval. These patterns are consistent with sustained enrichment of PGE- and Zn-bearing material, paralleling the trends observed in Figure 6, and may reflect climate-driven changes in the mobilization or transport of trace-metal-rich dust.

Taken together, these geochemical variations indicate a marked shift in dust-source characteristics, transport dynamics, and depositional processes at the onset of the YD. The coherent behavior of multiple independent elemental ratios is consistent with the interpretation that the Kangerlussuaq sequence preserves a primary atmospheric signal associated with YD climatic change, including its onset.

Nanoparticle evidence for abrupt climate-driven dust enrichment at the YD onset

To further evaluate the relationship between climate-driven dust changes and particle-scale geochemical behavior, we

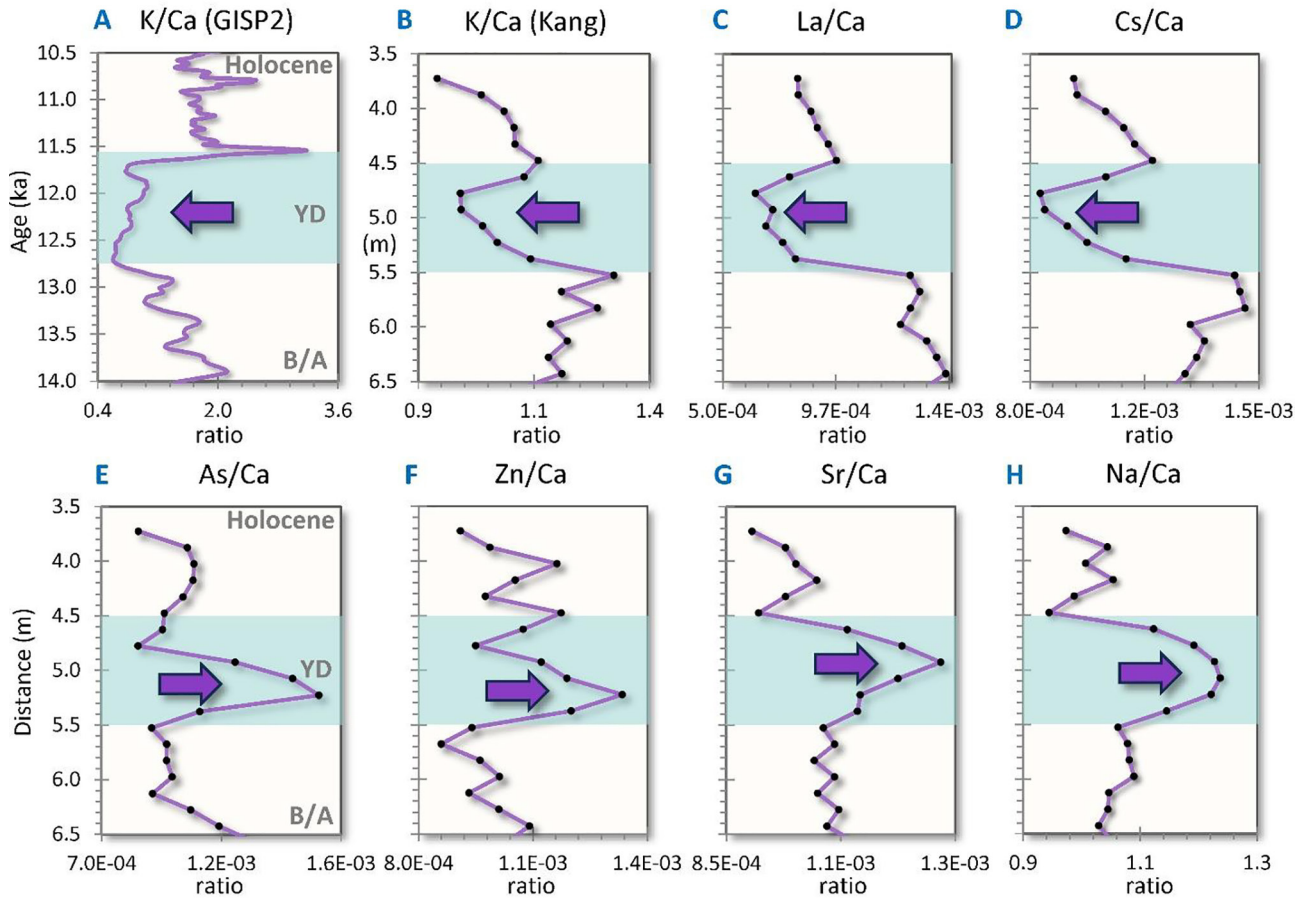


Figure 6: ICP-MS bulk elemental ratio variations across the Younger Dryas boundary reveal systematic changes in dust geochemistry. For the Kangerlussuaq samples, the blue bar represents the ~1-m-thick YD episode. (A) The K/Ca ratio from the GISP2 ice core exhibits a sharp decline at the YD onset and remains low throughout the YD interval. (B) The K/Ca ratio from Kangerlussuaq displays a comparable decrease across the YD boundary, confirming stratigraphic correlation. (C, D) Additional elemental ratios (La/Ca and Cs/Ca) from Kangerlussuaq exhibit similar significant declines coincident with the onset of the darker, dust-rich YD episode. (E-H) In contrast, ratios of As/Ca, Zn/Ca, Sr/Ca, and Na/Ca exhibit pronounced increases during the YD, consistent with enhanced influx of marine-derived aerosols and changes in terrestrial dust sources. These systematic geochemical shifts indicate a significant change in dust provenance and atmospheric transport dynamics at the YD onset.

examined elemental ratios within individual nanoparticles across the Bølling-Allerød (BA), Younger Dryas (YD), and Holocene intervals using SP-ICP-TOF-MS. Unlike bulk ICP-MS data, which integrate all material within a sample, this approach resolves compositional changes at the level of individual particles, providing a more sensitive indicator of shifts in dust source, transport, and atmospheric processing.

Here, we explore compositional variability using Fe/Si, Mn/Si, Ba/Si, and Ti/Si ratios as representative tracers of major mineral dust components (Figure 7). These elements are predominantly associated with terrestrial silicate and oxide phases and are not uniquely diagnostic of extraterrestrial input. Instead, they provide a robust framework for evaluating whether the onset of the YD was accompanied by abrupt changes in terrestrial dust composition and loading that persisted throughout the ~1,200–1,300 year-long YD interval. At the same time, any systematic enrichment above the YDB layer may also be consistent with the additional introduction of fine-grained terrestrial material derived from high-temperature processes, including possible non-ET impact-related dust. See Figure 7.

Interpretation. The nanoparticle data show a clear and reproducible pattern across all four elemental ratios: a sharp increase in Fe/Si, Mn/Si, Ba/Si, and Ti/Si immediately above the YDB layer, followed by sustained elevated values throughout much of the Younger Dryas interval, sometimes continuing into the Holocene. This behavior closely parallels the bulk geochemical trends observed in Figure 6 but is resolved here at the nanoparticle level, confirming that the signal reflects a real change in dust composition rather than averaging effects.

The most significant feature is that the enrichment initiates at the YDB (~5.5 m) and peaks at ~5.2 m. This offset

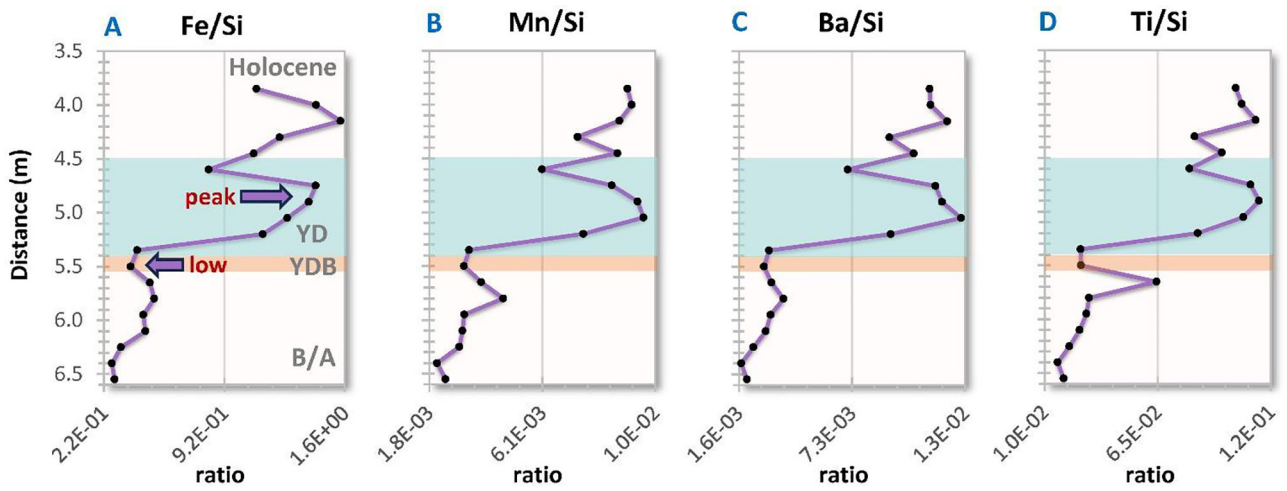


Figure 7: Nanoparticle elemental ratios reveal abrupt enrichment above the Younger Dryas Boundary. (A-D) Single-particle ICP-TOF-MS profiles of Fe/Si, Mn/Si, Ba/Si, and Ti/Si ratios across the Bølling-Allerød (BA), Younger Dryas (YD), and Holocene intervals. The YD interval is shaded in blue, and the Younger Dryas Boundary (YDB) layer is indicated by the orange band at ~5.5 m. All four elemental ratios exhibit a pronounced increase in the interval immediately above the YDB (~5.2 m), followed by sustained elevated values through much of the YD. Relative to the YDB layer at 5.5 m, the overlying 5.2 m interval is enriched by factors of 3.0 (Fe/Si), 2.4 (Mn/Si), 3.2 (Ba/Si), and 3.1 (Ti/Si), consistent with a rapid and substantial increase in nanoparticle-associated dust immediately following the boundary. For comparison, estimated extraterrestrial (ET) material exhibits enrichments relative to average crustal abundance of approximately 5.0× (Fe/Si), 2.9× (Mn/Si), 0.0043× (Ba/Si), and 0.13× (Ti/Si), illustrating that the observed enrichments are broadly consistent with increased dust loading dominated by terrestrial silicate phases, rather than uniquely diagnostic ET signatures.

indicates that the peak in nanoparticle-associated dust does not coincide exactly with the boundary layer itself but occurs immediately afterward. Such a relationship is consistent with a rapid transition into a regime of enhanced dust mobilization and transport, likely driven by the onset of colder, drier, and windier conditions characteristic of the Younger Dryas.

At the same time, the magnitude and synchronicity of the enrichments across multiple independent elements are consistent with a rapid reorganization of atmospheric dust flux rather than a gradual adjustment. Importantly, these elements are predominantly associated with terrestrial mineral sources, and their relative enrichments do not uniquely indicate extraterrestrial input. However, the stratigraphic position of the enrichment, immediately above a boundary layer containing high-temperature impact-related proxies (shown below), raises the possibility that part of the fine-grained dust population includes material generated or mobilized by high-energy processes. In this context, the nanoparticle record may reflect a combination of climate-driven dust intensification and the atmospheric redistribution of fine particulate material introduced at or near the YD onset.

Taken together, the nanoparticle data provide strong, particle-resolved evidence for an abrupt increase in dust loading and a reorganization of atmospheric transport at the onset of the Younger Dryas, while also establishing a stratigraphic framework that distinguishes the broader climate-driven signal from the discrete, impact-related proxy peak at the YDB layer.

Dust provenance shift as an atmospheric marker of the Younger Dryas onset

To further constrain the identification of the Younger Dryas (YD) interval and evaluate changes in atmospheric dust sources, we conducted SP-ICP-TOF-MS on nanoparticles extracted from the Greenland ice sequence. This approach provides particle-resolved compositional data, allowing quantification of elemental associations within individual particles over a size range of ~20 nm to 2 μm, thereby offering substantially higher resolution than bulk geochemical methods.

Nanoparticles were analyzed across three climatically defined intervals: the Bølling-Allerød (BA; 5.63–6.68 m), the Younger Dryas (YD; 4.57–5.47 m), and the Holocene (3.82–4.42 m). The dataset comprises more than 1.2 million individual particles (~60,000 per sample across 20 samples), enabling robust statistical characterization of compositional trends.

For clarity of interpretation, elemental associations were grouped into two dominant dust-phase populations based on their stratigraphic behavior: (1) phases that increase during the YD, dominated by quartz-, chromite-, and zircon-associated particles; and (2) phases that decrease during the YD, dominated by Fe-oxide-rich, Al-rich, and mica-amphibole-associated particles. This simplified grouping captures the principal structure of the dataset and allows direct evaluation of changes in dust provenance and atmospheric transport across the YD transition. Results in Figure 8.

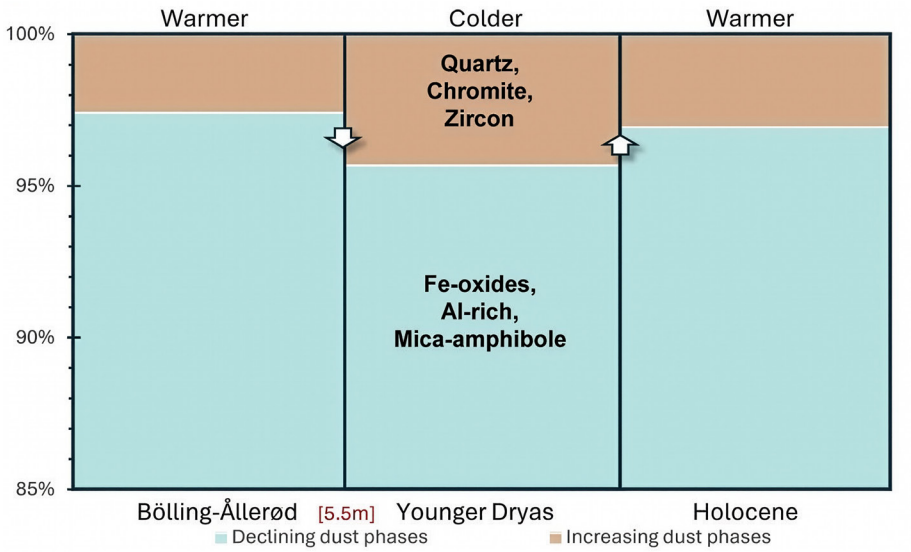


Figure 8: Binary dust-phase shifts across the Younger Dryas interval. Single-particle ICP-TOF-MS analyses reveal systematic changes in two dust-phase populations grouped by composition across the Bølling-Allerød (BA), Younger Dryas (YD), and Holocene intervals. Relative abundances are normalized to 100%. Quartz-, chromite-, and zircon-associated phases increase at the YD onset, while Fe-oxide-rich, Al-rich, and mica-amphibole-associated phases show a complementary decline. The transition is abrupt at the BA-YD boundary and reverses at the onset of the Holocene. These opposing trends indicate a major reorganization of dust composition and provenance coincident with the YD onset, consistent with intensified atmospheric circulation and changing source-region contributions.

Interpretation. The onset of the Younger Dryas is marked by a pronounced and internally consistent shift between two dominant dust-phase populations, consistent with a fundamental reorganization of atmospheric dust sources rather than a simple increase in dust flux. The most diagnostic feature is the strong inverse relationship between the two groups: quartz-, chromite-, and zircon-associated phases increase at the YD onset, while Fe-oxide-rich, Al-rich, and mica-amphibole-associated phases decline in a complementary manner.

This binary shift indicates a change in dust provenance and transport processes. During the Bølling-Allerød, the relatively higher abundance of Fe-oxide-rich, Al-rich, and mica-amphibole-associated particles is consistent with inputs from more chemically altered or compositionally mature dust populations under warmer interstadial conditions. At the YD onset, the rapid enrichment in quartz, chromite-, and zircon-associated particles suggests increased delivery of more refractory and less chemically altered mineral components, consistent with intensified physical erosion, stronger winds, and greater entrainment of primary mineral dust under colder and more arid conditions.

The observed phase relationships are consistent with strengthened atmospheric circulation during the YD, which enhanced long-range dust transport that altered the relative contributions of major source regions [75, 76]. Independent studies indicate that dust reaching Greenland during the Bølling-Allerød was largely dominated by North African sources, whereas during the YD, contributions from East Asian deserts increased substantially [84–86]. The increase in quartz-, chromite-, and zircon-associated phases is consistent with such a shift in source-region mixing and with enhanced transport of refractory mineral assemblages.

At the onset of the Holocene, this pattern reverses: quartz-, chromite-, and zircon-associated phases decline, while Fe-oxide-rich, Al-rich, and mica-amphibole-associated phases increase. This reversal is consistent with reduced wind intensity, diminished physical dust mobilization, increased vegetation cover, and a renewed dominance of warmer-climate dust regimes.

Together, the abrupt and inverse behavior of these two dust-phase populations provides a clear and independent atmospheric marker of the Younger Dryas onset. The data indicate that the dark, dust-rich interval records not only increased dust loading but also a substantial shift in dust provenance and transport dynamics. In that respect, the nanoparticle record strengthens the interpretation that this interval has been correctly identified as the YD onset layer.

Nanoparticle evidence for a transient impact-related dust pulse at the YD onset

To determine whether the abrupt, climate-driven increase in dust at the onset of the Younger Dryas included an additional input of thermally processed material, we analyzed nanoparticle-scale distributions of elements with contrasting geochemical behaviors using SP-ICP-TOF-MS. These include refractory lithophile elements (Nb, Ta, U), typically retained

in silicate phases, and more mobile chalcophile elements (As, Pb, Sb), which can be redistributed during heating, vaporization, and condensation. Unlike the lithophile-dominated elements in Figure 7 that primarily track dust provenance and transport, this combination enables evaluation of both entrained crustal material and components modified by high-temperature processes (Figure 9).

Interpretation. The nanoparticle records for Nb, Ta, U, As, Pb, and Sb display a coherent and diagnostic pattern: a sharp enrichment beginning immediately above the YDB layer, followed by elevated values that persist into the early Younger Dryas interval. This behavior differs from the lithophile-dominated trends shown in Figure 7, which primarily reflect a sustained, climate-driven increase in dust flux. In contrast, the profiles here exhibit a localized, higher-amplitude peak centered near ~5.2 m.

The magnitude and synchronicity of the enrichment across both refractory lithophile (Nb, Ta, U) and moderately volatile (As, Pb, Sb) elements indicate a rapid introduction of nanoparticle-scale material affecting multiple geochemical fractions simultaneously. Because refractory elements are typically transported as part of mineral dust, this enrichment is consistent with increased entrainment of crustal material and does not by itself require high-temperature mobilization, although it does not preclude it.

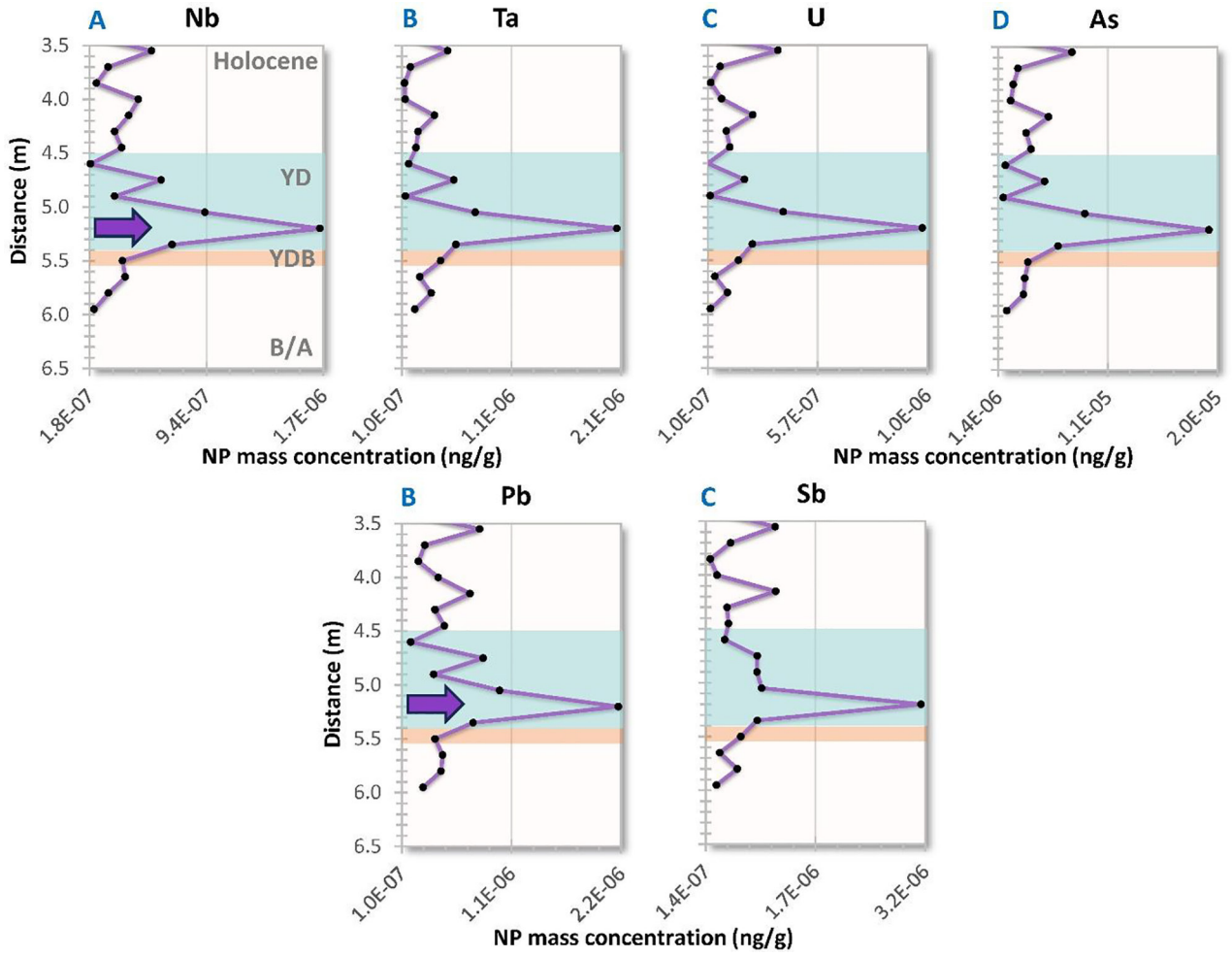


Figure 9: Nanoparticle mass concentrations of refractory lithophile and moderately volatile elements show a sharp enrichment above the Younger Dryas Boundary. (A-F) SP-ICP-TOF-MS mass concentration profiles of Nb, Ta, U, As, Pb, and Sb across the Bølling-Allerød (BA), Younger Dryas (YD), and Holocene intervals. The YD interval is shaded in blue, and the Younger Dryas Boundary (YDB) layer is marked by the orange band at ~5.5 m. All six elements exhibit a pronounced peak immediately above the YDB (~5.2 m), followed by elevated but variable concentrations within the YD interval. Relative to the YDB layer at 5.5 m, the overlying 5.2 m interval is enriched by ~4.2× (Nb), 4.5× (Ta), 4.4× (U), 4.9× (As), 5.2× (Pb), and 5.0× (Sb), consistent with a rapid and substantial increase in nanoparticle-associated material immediately following the boundary. Compared to average upper continental crust and CI chondritic (extraterrestrial) abundances, Nb, Ta, and U are strongly depleted in extraterrestrial materials (ET/crust < 1), while As, Pb, and Sb are near or below unity. This indicates that the observed enrichment is inconsistent with a direct extraterrestrial compositional signal, but instead reflects concentration of predominantly crustal material.

At the same time, the co-enrichment of As, Pb, and Sb indicates that at least part of the material experienced thermal processing, as these elements can be mobilized during heating and subsequently incorporated into nanoparticles during cooling. The combined behavior of refractory and more mobile elements is therefore consistent with a mixed particle population composed of entrained silicate dust and thermally processed components.

The stratigraphic position of the peak, immediately above the YDB layer, demonstrates that this enrichment does not represent the boundary layer itself, but rather a short-lived pulse of material deposited shortly after the initial event. This offset is consistent with rapid atmospheric injection followed by transport and settling of fine particles.

The enrichment patterns further argue against a direct extraterrestrial source for these elements. Because Nb, Ta, and U are strongly depleted in extraterrestrial materials relative to the crust, their coordinated enrichment requires a predominantly terrestrial origin. The data are therefore best explained by mobilization, entrainment, and redistribution of crustal material under high-energy conditions.

A key feature of the dataset is that concentrations of both these predominantly terrestrial elements and siderophile- and PGE-bearing particles (Ir, Pt, Ni, Co) are lowest within the YDB layer itself and rise sharply to maximum values in the immediately overlying sample (~5.2 m). This pattern indicates that the boundary layer marks the onset of deposition rather than its peak and requires a temporally structured, multi-phase process.

Several mechanisms may account for this structure. One possibility is that the boundary layer reflects rapid deposition of coarse or early-forming material, followed by delayed atmospheric residence and fallout of finer particles. Alternatively, enhanced precipitation or meltwater scavenging during boundary formation may have preferentially removed fine-grained or metal-bearing particles, producing a relative depletion within the YDB layer. A third possibility is that two closely spaced influxes occurred: an initial pulse dominated by high-temperature proxy materials, followed by a slightly delayed influx of entrained terrestrial dust and extraterrestrial nanoparticles.

These observations require a temporally extended depositional sequence rather than a single instantaneous event. This interpretation is supported by independent observations from the GISP2 ice core, where a large Pt anomaly as part of a "cataclysmic" impact event coincident with the onset of Younger Dryas climate change was identified [87]. In that record, platinum concentrations rise gradually over approximately 14 years to a delayed peak, followed by a decline over ~7 years, indicating a ~21-year interval of enhanced deposition. The anomaly occurs contemporaneously with a sharp decrease in $\delta^{18}O$ values marking the onset of Younger Dryas cooling and was interpreted as the result of a cosmic impact event. Notably, the elevated Pt/Ir ratio in that study was considered inconsistent with a chondritic source, instead suggesting a more fractionated or metal-rich component. The temporal structure of the GISP2 platinum anomaly closely parallels the delayed nanoparticle peaks observed in the Greenland ice-margin record, providing independent support for a multi-phase depositional process involving prolonged atmospheric residence and fallout of impact-derived material. Possible mechanisms include multiple airbursts or impacts occurring over a short interval, sustained accretion of fine debris from a cometary dust stream, or delayed reaccretion of impact-generated material. In particular, impact modeling studies have proposed that ejecta from a large impact could form transient, ring-like structures around Earth, analogous to planetary rings, which would gradually decay and deliver material back to the surface over time, as previously proposed [88]. Such a mechanism could prolong the atmospheric residence and deposition of fine-grained material and is consistent with the observed offset between the boundary layer and the overlying nanoparticle peaks. While these mechanisms remain hypothetical, they are consistent with the multi-phase deposition inferred from the Greenland record.

Multiple lines of evidence consistent with a YDB impact layer

The geochemical and particle-resolved results above demonstrate that the onset of the Younger Dryas is marked by a rapid and sustained reorganization of atmospheric dust composition, provenance, and transport. These changes reflect a climate-driven shift toward colder, more arid, and windier conditions, resulting in enhanced delivery of mineral dust to the Greenland ice sheet. Superimposed on this broader atmospheric signal, however, is a stratigraphically confined interval at the base of the YD that contains a distinct assemblage of high-temperature and impact-related materials. To evaluate whether this interval represents a discrete event separate from the longer-term climate-driven dust regime, we next examine the distribution of key impact proxies across the same stratigraphic section.

To assist in understanding the scope of an extensive, highly complex dataset and to provide context for the proxies discussed in the sections below, we present plots of four of the ten potential impact indicators, including nanodiamonds (1414×10^6/mL of ice), from Kurbatov et al. [19]. From this study, we plot shocked quartz (47/kg), meltglass fragments (43/kg), and spherules (34/kg). Results are shown in Figure 10 and subsequent figures (proxy data in SI, Table S2). These proxy abundances were normalized to sample ice volumes. All macro-scale proxies reach peak abundances within a narrow interval centered on the 5.5-m YDB layer, while nanoparticle populations reach maximum values slightly above this boundary.

Interpretation. The four proxy records shown in Figure 10 exhibit a tightly co-located peak at the ~5.5-m YDB layer, with sharply reduced abundances both above and below this interval. This stratigraphic confinement indicates that these

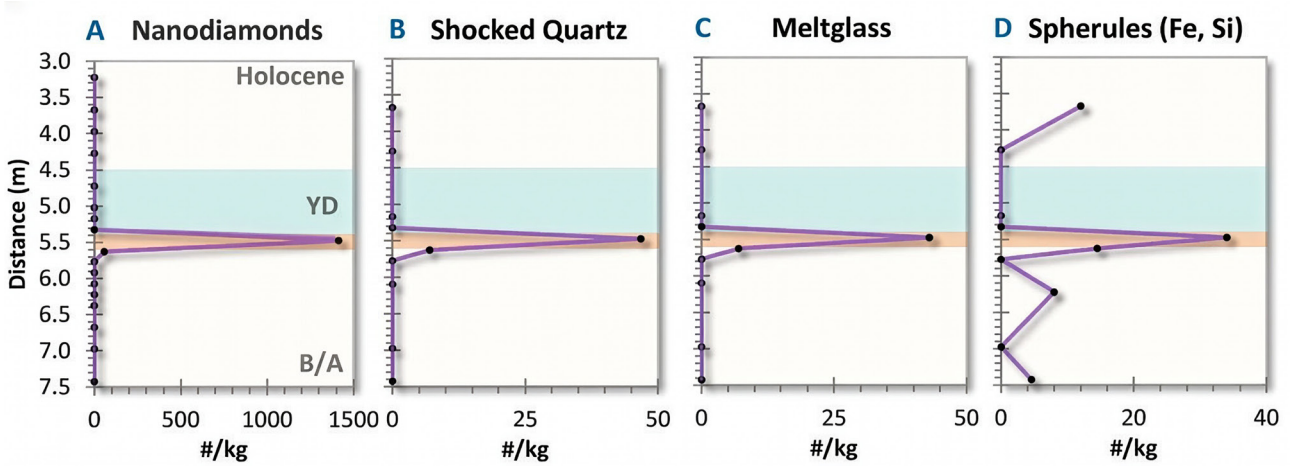


Figure 10: Four key impact-related proxies exhibit peaks in YDB ice at Kangerlussuaq. (A-D) These proxies (nanodiamonds, shocked quartz, meltglass, and spherules) exhibit abundance peaks at the YD onset centered at 5.5 m in the stratigraphic section (orange bar). YD interval in blue. Six other proxies not shown here also increase in abundance at the YD onset, as discussed below.

materials were introduced during a brief and discrete depositional episode rather than through sustained background processes. The co-occurrence of nanodiamonds, shocked quartz, meltglass, and spherules, each associated with high-temperature formation and, in some cases, high-pressure conditions, suggests a common origin involving elevated-energy processes. Importantly, these peaks are superimposed on the broader Younger Dryas dust interval identified above, indicating that they do not simply reflect the longer-term climate-driven increase in dust flux. Instead, their narrow stratigraphic distribution and coincidence across multiple independent proxy classes are consistent with a short-lived event at or near the onset of the Younger Dryas.

While the proxies shown here are tightly confined to the YDB layer, particle-resolved geochemical analyses presented below indicate that some components, particularly PGE-bearing nanoparticles, reach peak abundances slightly above this boundary. This offset suggests that impact-related materials were not deposited as a single, instantaneous pulse, but rather through a more complex, multi-phase atmospheric process involving both immediate deposition at the boundary and delayed fallout in the interval above. The following sections examine each proxy in detail to assess their formation conditions and evaluate potential origins.

YDB nanodiamond peak

Nanodiamonds have previously been reported in the YDB layer at 9 of 19 investigated sites, many of which also contain shocked quartz [23]. Kurbatov et al. [19] first identified a distinct peak in nanodiamond abundance, including particles interpreted as lonsdaleite, in YDB ice from Kangerlussuaq, Greenland. These findings were subsequently confirmed by Kinzie et al. [23]. Comparable diamond polymorphs have been reported in other impact-related settings, including the Cretaceous-Paleogene (K-Pg) boundary and the Ries impact structure [70, 71, 89–91].

Here, we report additional nanodiamond evidence from the Kangerlussuaq YDB layer, including cubic diamond, *n*-diamond, *i*-carbon, and a lattice-resolved particle exhibiting spacings consistent with hexagonal diamond (lonsdaleite-like structure), a phase not previously documented in detail from this site.

Nanodiamond allotropes were investigated using high-resolution transmission electron microscopy (HRTEM), scanning transmission electron microscopy (STEM), and selected-area electron diffraction (SAED), supplemented by fast Fourier transform (FFT) analysis of lattice-resolved images. These methods enable measurement of interplanar spacings and crystallographic relationships characteristic of known carbon allotropes (cubic diamond, *n*-diamond, *i*-carbon, and hexagonal diamond) [19, 23]. Results are shown in Figure 11, with measured lattice spacings reported in SI Table S3.

Interpretation. Nanodiamonds have been reported at numerous YDB sites across North America [23, 32–36], Europe [16, 23, 36–38], and Asia [23, 36, 39]. Quantitative nanodiamond abundances for Greenland were previously published in Table 2 of Kurbatov et al. [19]. The crystallographic spacings measured in the present study for cubic diamond, *n*-diamond, *i*-carbon, and lonsdaleite-like structures correspond closely to those reported in prior investigations [19, 23] (Figure 11; SI Table S3).

One lattice-resolved particle (Figure 11B) exhibits spacings of ~2.18 Å, ~2.06 Å, and ~1.93 Å, consistent with reported values for hexagonal diamond (lonsdaleite-like). The corresponding FFT pattern shows a coherent set of reflections compatible with a hexagonal lattice. However, some expected higher-order reflections are weak or absent,

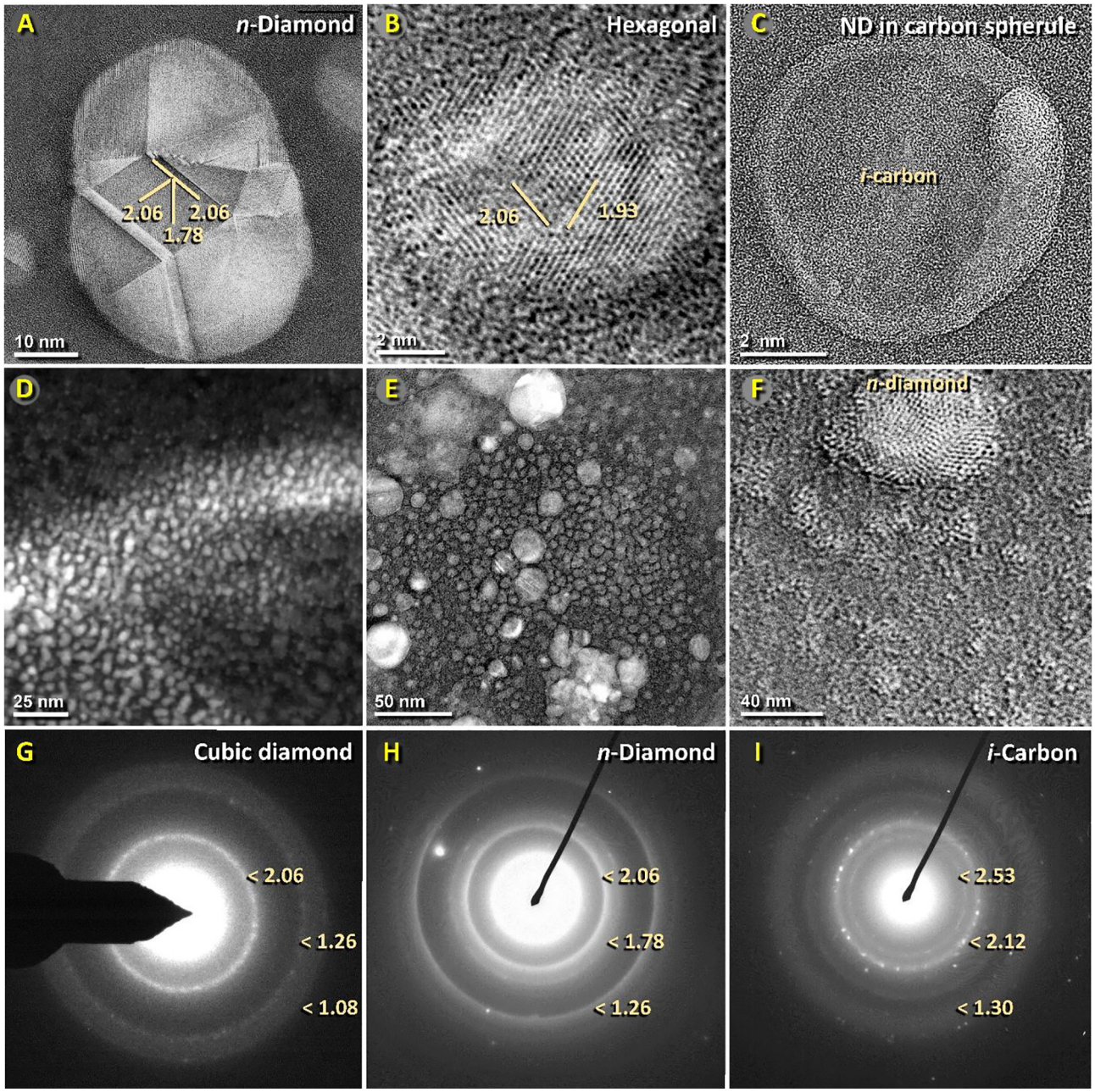


Figure 11: Nanodiamonds in YDB ice revealed by transmission electron microscopy. (A) Polycrystalline *n*-diamond. Panel modified from Kinzie et al. [23]. (B) Lattice-resolved nanocarbon particle exhibiting spacings consistent with hexagonal diamond (lonsdaleite-like). Measured lattice spacings of ~2.18 Å, ~2.06 Å, and ~1.93 Å were obtained from HRTEM imaging and corresponding FFT analysis, consistent with reported (100), (002), and (101) reflections of hexagonal diamond. (C) Carbon spherule, or possible carbon onion, containing an embedded *i*-carbon nanocrystal. (D-F) TEM images showing abundant mixed nanodiamond populations. (G) SAED pattern for cubic diamond from Kangerlussuaq, showing rings consistent with ~2.06, ~1.26, and ~1.08 Å spacings. (H) SAED pattern for *n*-diamond, with rings consistent with ~2.06, ~1.78, and ~1.26 Å spacings. (I) SAED pattern for *i*-carbon, with rings consistent with ~2.53, ~2.12, and ~1.30 Å spacings. Images in panels A-F were inverted for clarity. Lattice spacings are consistent with previously reported values for nanodiamond polymorphs [19, 23].

likely reflecting limited crystallite size, slight off-zone orientation, or imaging conditions.

Importantly, similar diffraction and lattice-spacing relationships can arise from stacking-disordered cubic diamond or intergrowths of cubic and hexagonal stacking sequences, which are well documented in both synthetic and impact-related nanodiamonds. Such structures can produce lonsdaleite-like diffraction signatures without requiring a fully ordered hexagonal diamond phase. Accordingly, we interpret this particle conservatively as exhibiting a lonsdaleite-like

structure or hexagonal stacking component rather than as definitive evidence for pure lonsdaleite.

Nanophase carbon-rich spherules or carbon-rich, ring-like structures observed in the Kangerlussuaq YDB ice (Figure 11C) consist of shells of sp^2-bonded carbon, typically <10 nm in diameter, in contrast to the sp^3-bonded nanodiamond structures. Several carbon rings were found enclosing nanodiamonds, a configuration consistent with high-pressure transformation processes. Tian et al. [37] reported that similar carbon-rich structures, called carbon onions, can generate internal pressures sufficient to induce graphite-to-diamond transitions, representing one possible high-energy transformation pathway discussed in the literature.

The HRTEM, FFT, and SAED results are consistent with the presence of carbon phases exhibiting lattice spacings compatible with reported nanodiamond polymorphs, including cubic diamond, *n*-diamond, *i*-carbon, and lonsdaleite-like structures. Although such features are not uniquely diagnostic and may reflect stacking disorder or nanoscale intergrowths, we conclude that current evidence supports the presence of nanodiamond-like carbon phases formed under high-temperature and, in some cases, high-pressure conditions.

Shock metamorphism of Younger Dryas boundary quartz grains

Shocked quartz is a well-established indicator of high-pressure events, including cosmic impacts. It has been previously reported in the YDB at 18 sites, on four continents, including 11 in North America [57, 58, 92], 2 in South America [47], 4 in Europe [44, 93], and 1 in Asia [94], collectively spanning distances up to ~12,000 km. This widespread distribution suggests that similar grains could be present in Greenland's YDB-age ice.

To investigate the presence of impact-related proxies in Greenland ice, we examined dust residues extracted from 20 samples, each averaging 344 mL of meltwater and yielding a dry dust mass of 0.243 g. Candidate grains exhibiting features consistent with shock metamorphism were identified through initial optical screening. These candidates were further analyzed using polarized light microscopy and a universal stage to evaluate diagnostic planar deformation features (PDFs) indicative of high-pressure shock. We further examined these sample particles using SEM, transmission electron microscopy (TEM and STEM), electron backscatter diffraction (EBSD), and cathodoluminescence (CL) imaging. In total, we identified 13 quartz grains with planar fractures (47/kg) from the YDB layer at a slope distance of approximately 5.5 meters, with two grains immediately below. Results are shown in Figures 12–15.

Planar deformation features observed using optical microscopy. The first step we took in searching for shocked quartz was to examine thin-sectioned grains using transmission and epi-illuminated optical microscopy to identify potential candidates. The objective was to locate quartz grains displaying parallel or slightly subparallel lamellae that are closely spaced, typically less than a few μm apart, and often containing material that is isotropic under crossed polars. The results are shown in Figure 12. Subsequently, it was necessary to examine the grains using additional analytical techniques, as described and discussed in the following sections.

Interpretation. The shocked quartz grains in the Kangerlussuaq samples represent, to our knowledge, the first direct report of such grains preserved within glacial ice, suggesting that shock-metamorphosed material can be transported by atmospheric processes and incorporated into ice-margin deposits. The measured crystallographic orientations are consistent with those commonly documented at confirmed impact sites [95]. Most grains contain a single set of planar deformation features (PDFs), consistent with lower shock pressures beginning at ~5 GPa. In contrast, a subset (e.g., Figure 12C, 12H, 12I) displays two intersecting PDF sets, consistent with exposure to higher shock pressures.

All examined grains also exhibit dark isotropic zones consistent with localized silica melting within or around the quartz grains, suggesting transient exposure to elevated temperatures. Approximately half of the grains (e.g., Figure 12D–12F, 12I) occur within glass-filled lithic aggregates composed of mineral fragments set in an amorphous matrix, a texture frequently associated with high-temperature conditions.

The distribution of measured crystallographic orientations includes one grain with (0001), 3 with $\{10\bar{1}3\}$ 1 with $\{10\bar{1}2\}$ with $\{10\bar{1}1\}$, 2 with $\{10\bar{1}0\}$, and 4 with $\{11\bar{2}1\}$. These orientations fall within the range of PDF plane families typically reported for experimentally shocked and naturally shocked quartz at confirmed impact structures [95].

Shock lamellae identified using transmission electron microscopy

To further characterize the microstructure of shocked quartz grain candidates, we used HRTEM, selected-area electron diffraction (TEM-SAED), fast Fourier transform (FFT), inverse fast Fourier transform (IFFT), and scanning transmission electron microscopy (STEM). This enabled us to identify and characterize planar deformation features (PDFs), amorphous silica, and glass-filled fractures in quartz grains that may have been affected by hypervelocity impact processes. The resulting TEM images are shown in Figure 13.

Interpretation. HRTEM analyses show that all of the candidate shocked quartz grains contain pervasive shock-related microstructures, including planar deformation features (PDFs) and regions of shock-induced amorphous silica. Brightfield HRTEM images (Figure 13A–13F) display crystallographically aligned lamellae, with amorphous silica recorded in areas labeled "glass," whereas

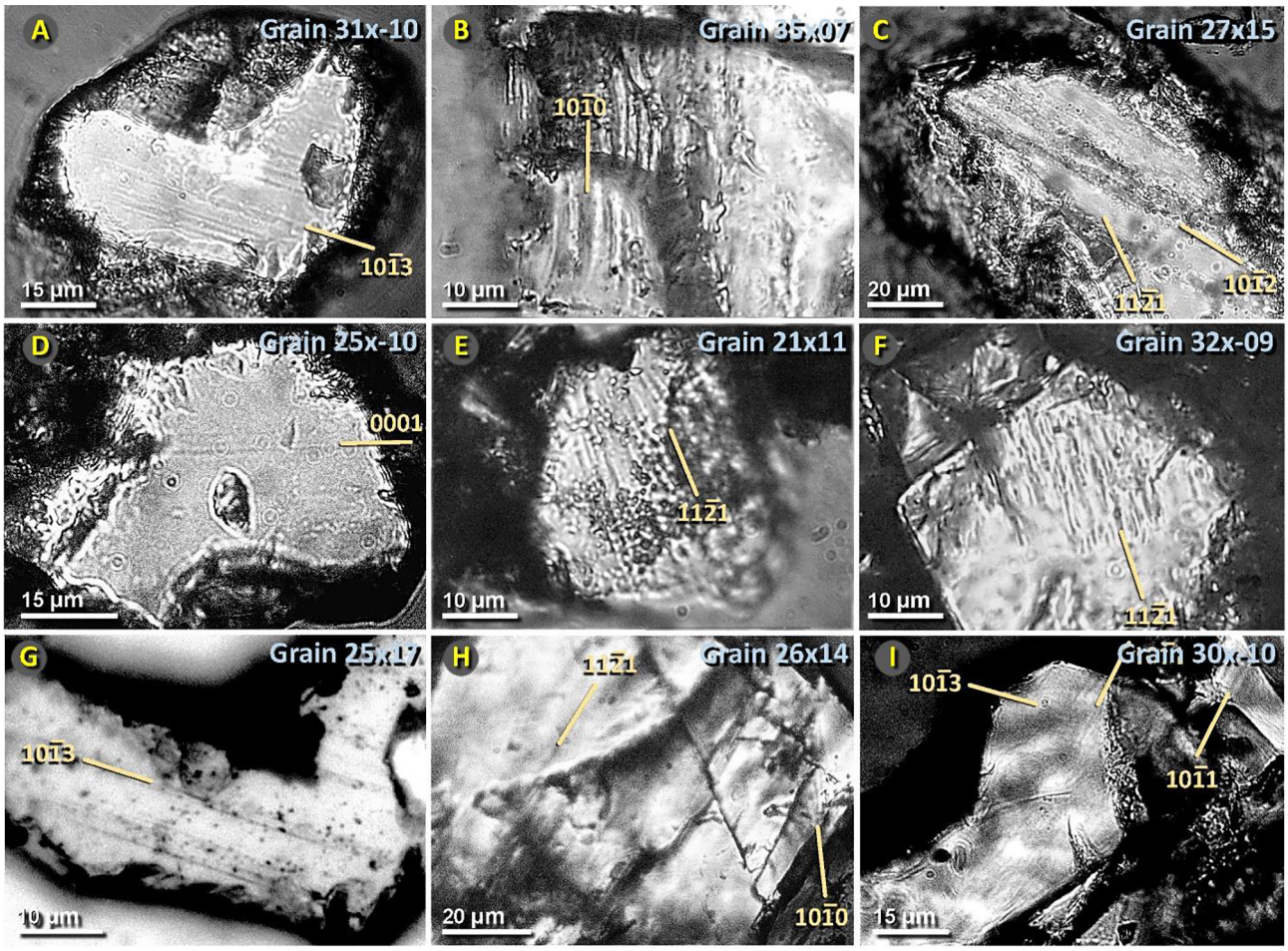


Figure 12: Optical microscopy images of quartz grains exhibiting planar features interpreted as planar deformation features (PDFs). (A-I) Cross-polarized (XPL) photomicrographs of examples extracted from the Kangerlussuaq YDB layer at ~5.5-m slope distance. The universal stage was used to determine crystallographic orientations (indicated by yellow lines) of the planar features.

adjacent "crystalline" regions retain the ordered lattice typical of unshocked quartz. Melted silica was observed in every grain, consistent with optical observations under crossed polars and with HRTEM characterization.

Fractures and lamellae in the Kangerlussuaq YDB quartz grains commonly contain amorphous silica. Crystallographic indices determined using the Miller-Bravais (hkil) system indicate lamellae ranging from <1 µm to >10 µm in width, consistent with previously documented shock features [95]. These microstructures are compatible with deformation under elevated pressures.

Elemental analyses of material within fractures, conducted using TEM-EDS and SEM-EDS, indicate that Si and O dominate the compositions (98–99 wt%). Oxygen abundances were consistently lower than the stoichiometric O/Si ratio of quartz. For example, grain 21 × –08 yielded an O/Si ratio of 43.70/56.30 wt%, approximately 10 wt% below the ideal 53.26/46.74 wt% ratio. This oxygen deficiency is inconsistent with hydrated silica phases such as hyalite or quartz overgrowths, which contain ~66 wt% O^2, and instead, is consistent with the presence of melted or amorphized silica. Although localized electron-beam damage in SEM/TEM can reduce O/Si ratios, multiple independent measurements and comparisons with adjacent unaltered crystalline quartz are consistent with oxygen depletion in these features.

Selected-area diffraction (TEM-SAD) and FFT analyses of glassy regions did not yield discrete diffraction spots; instead, they produced diffuse halos characteristic of amorphous structure and the loss of long-range atomic order. In some grains, small crystalline domains were detectable by HRTEM, though they lacked complete lattice reflections. Amorphous zones are commonly graded into crystalline quartz over distances of several hundred nanometers, consistent with partial thermal transformation from melt to crystal.

IFFT imagery (Figure 13G–13I) further supports this mixed structure: darker regions correspond to structurally compromised or melted quartz, whereas lighter areas indicate preserved crystallinity. The coexistence of these domains within individual grains is consistent with rapid melting and quenching.

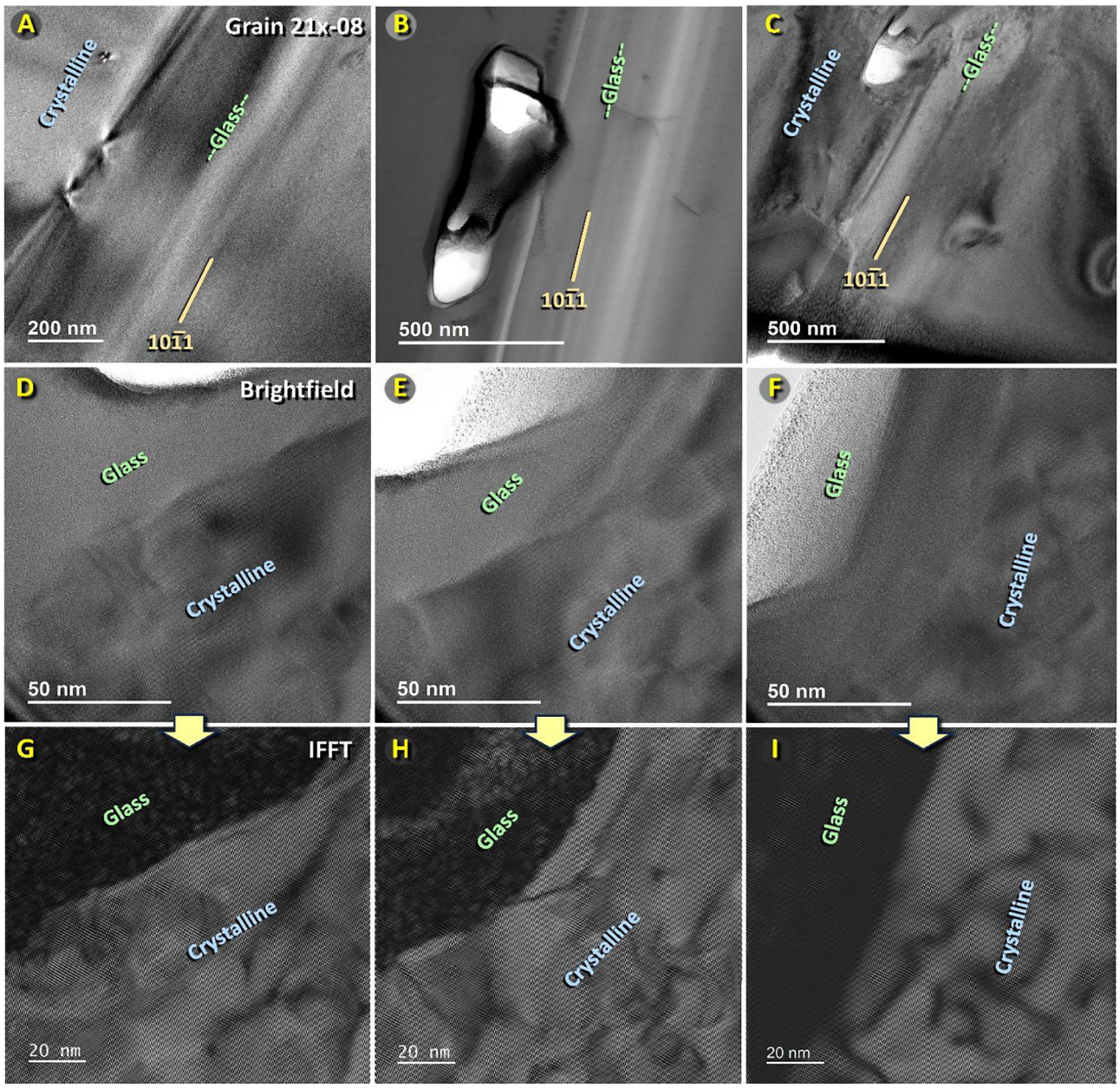


Figure 13: Transmission electron microscopy images of quartz grains exhibiting features consistent with shock metamorphism in the YDB layer. All images are of grain 21 × –08. (A-F) Brightfield HRTEM images show planar features interpreted as PDFs and amorphous quartz ("Glass") consistent with shock-altered regions. "Crystalline" denotes an intact lattice. (G-I) IFFT images of panels D-F highlight darker zones of amorphous quartz and lighter zones of normal crystalline quartz. TEM-measured Miller-Bravais indices (e.g., $\{10\bar{1}1\}$) are consistent with PDFs with inter-lamellae spacing of <1–2 μm. All images display features consistent with silica melting and shock-related damage.

Quartz grains from Greenland that we have identified as shocked also exhibit PDFs, as investigated by optical microscopy, TEM, and EBSD, features known to form under peak pressures ≥5 GPa and loading rates on the order of 10^6–10^7 GPa/s. In contrast, tectonic deformation (faulting, metamorphism) does not generate PDFs and typically produces dislocations without amorphous silica [96–98]. Several dozen tectonically deformed quartz grains examined for comparison lacked PDFs, PFs, and amorphous silica veins, allowing them to be distinguished from the shocked grains.

Hypervelocity impacts and airbursts are known to produce PDFs in both experimental shock-recovery studies and field settings at confirmed impact structures. Similar features have been reported in YDB deposits at multiple sites worldwide [40, 42]. In the Greenland samples, PDFs occur alongside nanodiamonds, meltglass, PGEs, and other established YDB proxy materials, with no evidence of tectonic

or diagenetic alteration. Collectively, these observations are consistent with a shock-related origin for the quartz grains.

Crystalline disruption revealed using electron backscatter diffraction

Electron Backscatter Diffraction (EBSD) is a powerful technique for characterizing crystallographic deformation in shocked quartz. This method enables high-resolution analysis of planar deformation features (PDFs) and other microstructures resulting from high-pressure impact events. EBSD provides insight into the shock-induced damage observed in quartz grains subjected to extreme pressures, such as those associated with a cosmic airburst or impact event. The results are shown in Figure 14.

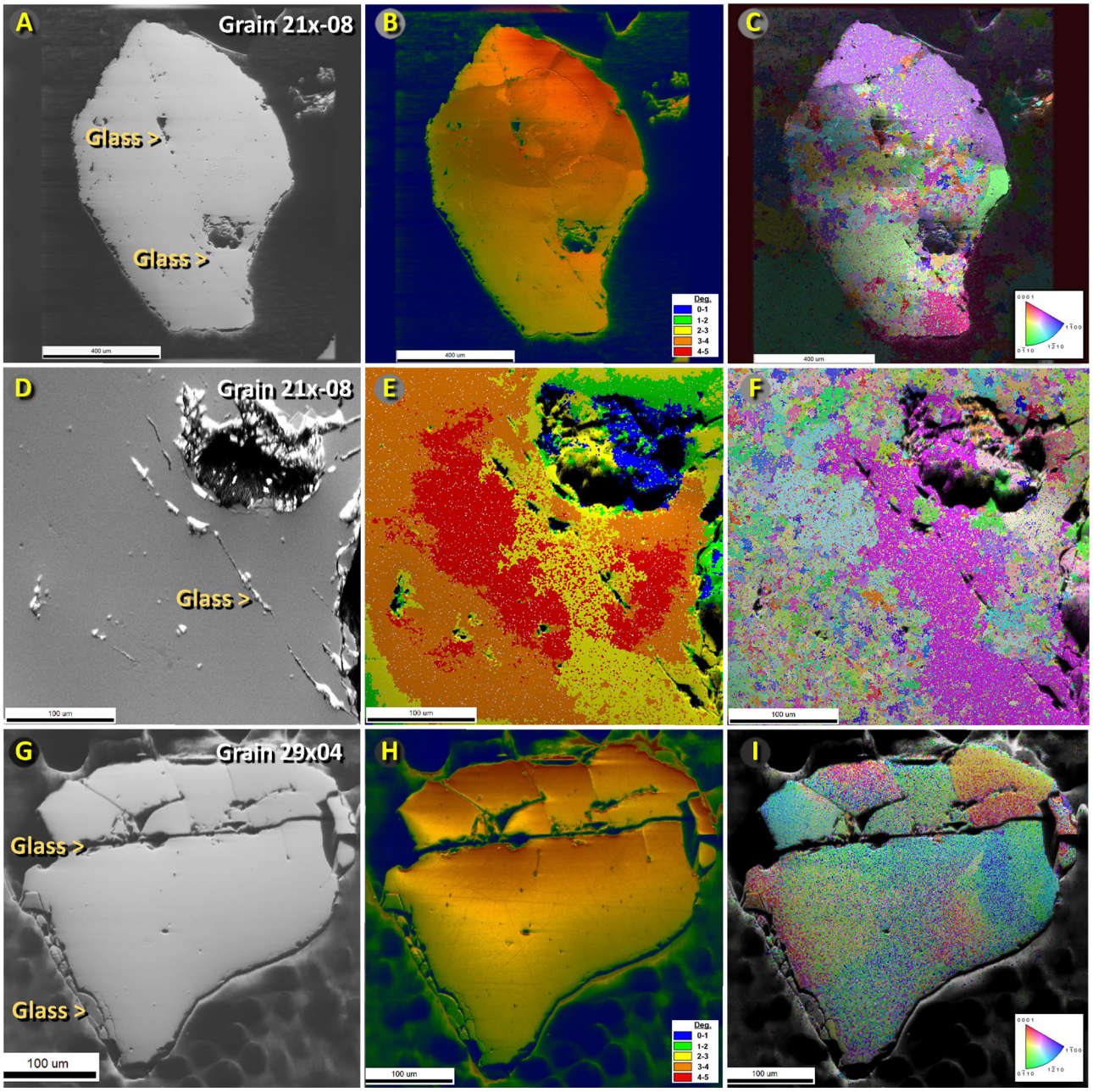


Figure 14: Electron Backscatter Diffraction (EBSD) images exhibiting crystalline damage in YDB quartz grains. (A, D), and (G): SEM-like PRIASB images display grain surface topography. (B, E), and (H): PRIASB-IQ images are color-coded by degree of lattice distortion (0–5°, as shown in legends). (C, F), and (I): PRIASB-IPF image illustrates short-range changes in crystallographic orientation, as shown in legends. Yellow arrows mark glass-filled cracks. These images collectively reveal extensive fracturing, lattice distortion, and axial rotation consistent with shock metamorphism.

Interpretation. Quartz grains extracted from the YDB interval were examined using EBSD imaging (Figure 14) to evaluate the extent and character of crystallographic deformation. For each representative grain (21 × –08 and 29 × 04), three complementary data products were generated: (1) PRIASB SEM-like images showing surface topography; (2) PRIASB-IQ images indicating degrees of lattice distortion; and (3) PRIASB-IPF images illustrating crystallographic orientations.

The PRIASB SEM-like images (left column) reveal pronounced fracturing and surface disruption in both grains. PRIASB-IQ images (middle column), color-coded according to the degree of misorientation, show lattice distortions of up to ~5°, with values ranging from low deviation (green, ~0–1°) to higher deviation (red, ~4–5°). These patterns indicate localized deformation consistent with shock-related microstructures. The PRIASB-IPF images (right column) display a broad range of crystallographic orientations over micron-scale distances, reflecting substantial axial rotation and internal strain.

EBSD mapping also allowed assessment of c-axis orientations. Grain 21 × –08 exhibits multiple c-axes but lacks clearly defined grain boundaries, suggesting recrystallization into submicron domains. Grain 29 × 04 appears largely monocrystalline but still shows internal rotational strain. These characteristics are consistent with partial melting followed by rapid quenching, producing fine-scale recrystallized regions with heterogeneous orientations.

Taken together, the EBSD observations, fracturing, misorientation patterns, and microdomain recrystallization are consistent with high-pressure, high-temperature shock metamorphism. These microstructural features align with those documented in experimentally shocked quartz and in quartz from confirmed impact structures.

Thermal alteration in quartz grains revealed by cathodoluminescence

Cathodoluminescence (CL) imaging is a powerful technique for identifying structural and thermal damage in quartz grains subjected to high-pressure events. Quartz subjected to shock waves is accepted to exhibit planar deformation features (PDFs), intragranular fracturing, and partial or complete amorphization, all of which modify the crystal lattice and its luminescence response. CL microscopy exploits this by detecting visible light emitted when the quartz lattice is excited by an electron beam. Intact crystalline quartz typically emits blue-to-red luminescence, depending on trace-element content and crystallinity. In contrast, domains interpreted as shock-modified, e.g., those displaying particularly melt-zoned and heavily damaged regions, often appear non-luminescent (black).

However, CL imaging alone is not sufficient to uniquely diagnose shock metamorphism, as non-luminescent quartz may also occur in low-temperature authigenic (diagenetic) quartz formed under sedimentary conditions. Accordingly, CL is used here as a spatial mapping and screening tool to identify regions of interest, which are then evaluated using complementary techniques. Optical microscopy under crossed polars is employed to assess crystallinity and deformation textures, while transmission electron microscopy (TEM) and electron backscatter diffraction (EBSD) are used to confirm the presence, orientation, and crystallographic nature of PDFs and to distinguish crystalline quartz from amorphous or recrystallized silica. The combined use of these methods provides a robust basis for differentiating shock-related microstructures from those produced by non-impact processes.

In this study, paired scanning electron microscopy (SEM) and CL images were obtained from quartz grains extracted from the Younger Dryas Boundary (YDB) ice layer. Figure 15 displays representative grains 16 × 06 and 27 × 08, interpreted as displaying fractures, planar to subplanar lamellae, and regions of luminescence quenching.

Interpretation. The cathodoluminescence (CL) images show that the dark regions in Panels D-F are non-luminescent and correspond to amorphous silica, consistent with shock melting followed by rapid quenching. Blue luminescence denotes unaltered quartz, whereas red-to-orange regions indicate thermally recrystallized silica. These patterns are consistent with previously documented CL responses of shock-modified quartz [99–102].

Elemental measurements are consistent with this interpretation. SEM-EDS analyses show that glass-filled fractures in Grain 16 × 06 have an O/Si ratio of 33.51/66.48 wt%, while Grain 27 × 08 records 30.14/69.86 wt%. These oxygen abundances are substantially lower than the stoichiometric O/Si ratio of ~53.26/46.74 wt% measured in unaltered crystal regions of the same grains, indicating ~20–23 wt% oxygen loss. Such depletion is consistent with high-temperature dissociation of silica, during which oxygen is released from the lattice.

These low O/Si ratios are inconsistent with hydrated amorphous silica phases such as opal-A or hyalite, which typically exhibit O/Si values near 66/34 wt%. The absence of CL emission, together with oxygen-deficient compositions, indicates that the glassy zones are anhydrous and unrelated to low-temperature aqueous alteration or biogenic silica. Likewise, diagenetic features such as quartz overgrowths or silica cements can be excluded because they are crystalline and would normally luminesce under CL imaging.

The combined structural and chemical signatures, including non-luminescent amorphous zones, intragranular fracturing, planar lamellae, and oxygen depletion, are consistent with shock-related modification of the quartz grains. Their co-occurrence within the YDB interval, along with other proxy evidence, is consistent with an interpretation that the grains experienced high-temperature, high-pressure conditions. No currently known volcanic,

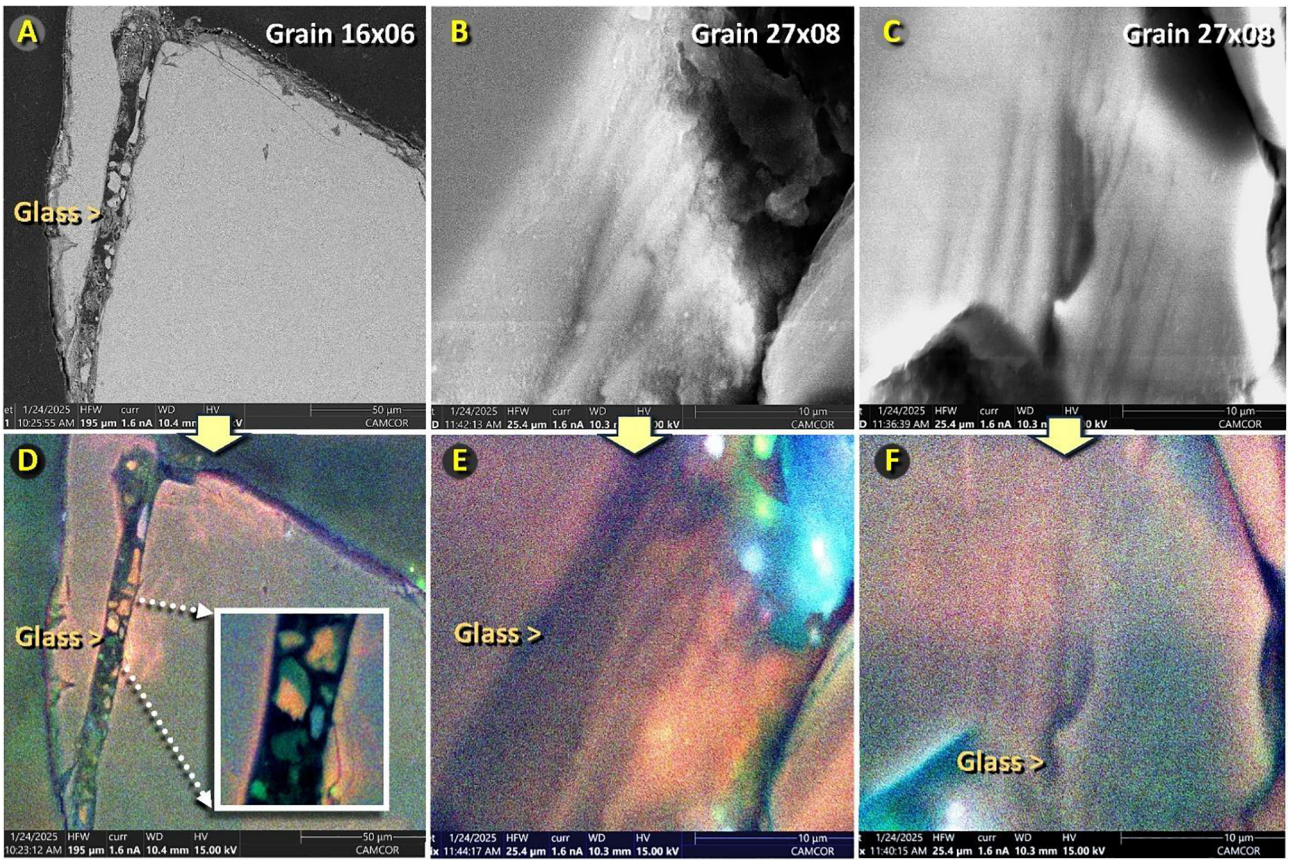


Figure 15: Cathodoluminescence (CL) and SEM images show evidence interpreted as crystalline damage. Images are of quartz grains 16 × 06 and 27 × 08 from the YDB layer. Panels A-C: SEM images showing features interpreted as intragranular fracturing and planar lamellae. Panels D-F: Corresponding CL images of the same regions. Red and orange regions represent thermally recrystallized quartz; blue areas denote unaltered quartz; black regions correspond to non-luminescent amorphous silica. The inset in Panel D shows micron-scale quartz and other mineral fragments embedded in a glassy silica matrix, identified via SEM-EDS. These results document structural and thermal alteration consistent with shock metamorphism. The limited visibility of diagnostic planar deformation features (PDFs) in SEM images reflects the inherent limitations of SEM for resolving PDFs in thin-sectioned quartz without acid etching. The presence of PDFs is independently supported by higher-resolution TEM and EBSD analyses (Figures 12–14) Because similar features can arise from non-impact processes, these observations are interpreted alongside crystallographic and microstructural analyses.

diagenetic, or anthropogenic process adequately explains the combination of features within near-surface ice environments at the onset of the Younger Dryas.

Glass-filled fractures in quartz

Optical microscopy is a widely accepted method for identifying high-temperature alteration features in quartz grains, including amorphous silica. Under cross-polarized light, unaltered quartz exhibits characteristic birefringence, transitioning in and out of extinction as the stage is rotated. In contrast, amorphous or melted silica appears optically dark and isotropic throughout rotation. Because some unmelted silica phases may also exhibit isotropic behavior, further analysis is required for confirmation, including SEM-EDS, TEM, CL, and EBSB.

Of particular interest are glass-filled fractures in quartz, also referred to as silica glass veins, observed in grains extracted from the YDB ice layer. These fractures are notable because the melting point of quartz (~1713 °C) exceeds the thermal limits of biomass burning and most volcanic processes, including rhyolitic eruptions. As a result, the presence of glassy silica suggests exposure to extreme thermal conditions. Such features are typically associated with high-energy phenomena, including lightning strikes, anthropogenic processes, or cosmic impacts. To investigate these features, we analyzed quartz grains from the YDB layer using plane-polarized optical microscopy. Selected images are shown in Figure 16.

Interpretation. The non-planar, glass-filled fractures observed in Figure 16 display textures consistent with high-temperature modification of quartz. One plausible formation mechanism involves two stages: (1) initial grain fracturing generated by a high-stress pulse, followed by

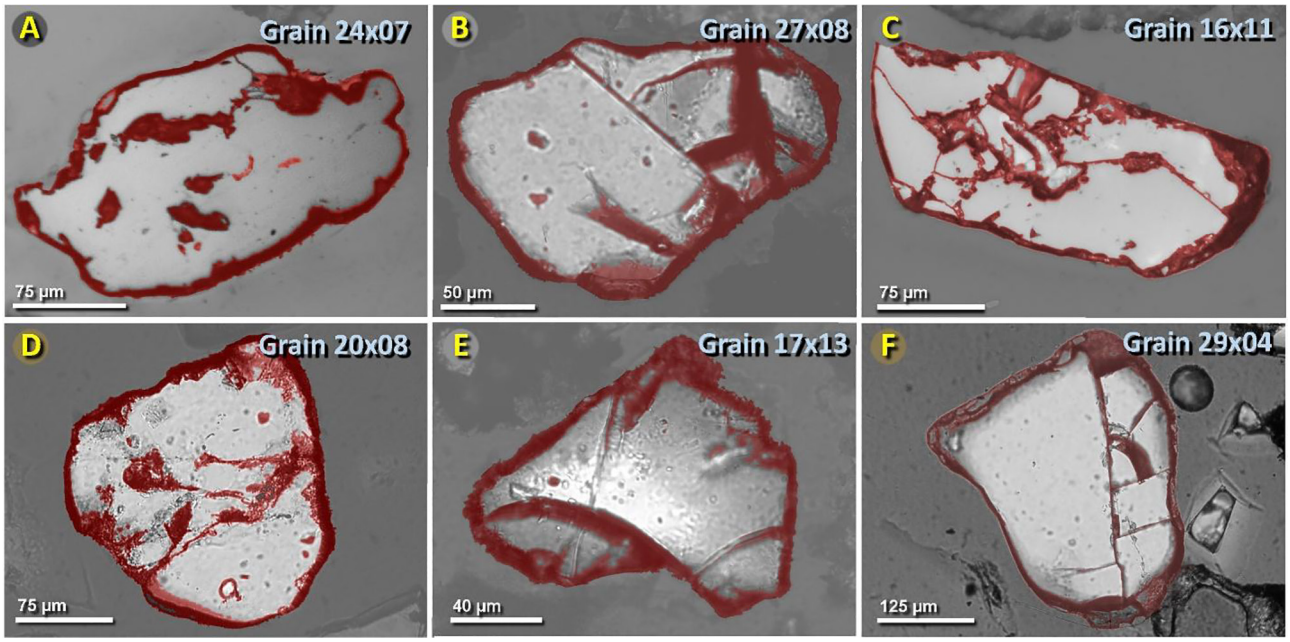


Figure 16: Optical images of quartz grains displaying non-planar, glass-filled fractures. Panels A-F: Plane-polarized optical microscope images of quartz grains with fractures filled by amorphous silica (silica glass veins). Red false-colored regions denote isotropic, optically dark zones consistent with melted and rapidly quenched silica. These features are consistent with high-temperature modification that can produce amorphous silica within fractures and are compatible with shock-related processes as a plausible mechanism.

(2) infilling of these fractures by molten silica under elevated pressure. Comparable melt-injection textures have been described at Meteor Crater, where silica melt penetrated shock-induced fractures via "jetting" processes [103]. Related mechanisms, including early-stage melt injection and fracture formation associated with spallation or rarefaction waves, have been documented in experimental and field studies [104–107].

SEM and TEM analyses indicate that the fracture-fill material is amorphous and lacks crystalline order, distinguishing it from quartz overgrowths or silica cement. The absence of submicron spherical crystallites also excludes cryptocrystalline silica varieties such as chert, agate, or chalcedony [108]. SEM-EDS measurements yield O/Si ratios consistently below 53/47, reflecting oxygen-deficient compositions. These values differ markedly from hydrated silica phases such as hyalite or opal-A, which exhibit O/Si ratios near 66/34 wt% [92, 94, 96, 109]. The low oxygen content, combined with the amorphous structure, is consistent with an origin involving high-temperature silica melting rather than low-temperature aqueous alteration.

Anthropogenic processes are unlikely given the absence of similar glass-filled grains outside the YDB interval. Lightning can produce localized silica melting, but typically generates tubular fulgurites with distinctive morphologies and does not create the combination of fracture-fill textures and co-occurring enrichments in PGEs, Ni, and Co observed at the YDB layer. Volcanic and biomass-burning processes are also inconsistent with the observed mineralogies and thermal conditions, as well as with the absence of accompanying tephra or other volcanic components.

Taken together, the glass-filled fractures, when considered alongside their amorphous composition, oxygen-deficient chemistry, and co-occurrence with other proxy materials within the YDB interval, are consistent with formation under high-temperature, high-pressure conditions. These features most plausibly reflect shock-related processes followed by rapid quenching during the Younger Dryas onset.

Impact meltglass in the Younger Dryas Boundary layer

Meltglass has previously been reported at 14 of 19 YDB sites containing shocked quartz and is widely regarded as an important diagnostic indicator of extreme thermal events, including cosmic impacts [110, 111]. These meltglass fragments often exhibit vesicular morphologies and contain inclusions of high-temperature minerals, such as zircon, quartz, magnetite, kaolinite, and baddeleyite.

We investigated whether high-temperature meltglass is present by optically selecting candidates. Numerous glassy fragments were observed in the YDB layer, but not in the layers above or below it. To characterize the physical and chemical properties of these meltglass candidates, we used a combination of plane-polarized and epi-illuminated optical microscopy, scanning electron microscopy (SEM), and SEM-energy-dispersive spectroscopy (EDS). As shown in

Figure 17, these methods enabled assessment of isotropy, surface textures, vesicle structure, mineral inclusions, and major-element composition, thereby allowing discrimination between anthropogenic, volcanic, and impact-related origins.

Interpretation. Under crossed polarizers, all examined fragments appear isotropic, consistent with a noncrystalline, glassy composition. Plane-polarized and reflected-light photomicrographs show diagnostic high-temperature textures, including vesicles, melted relict planar deformation features (PDFs, partially erased by grain melting), and irregular flow structures. SEM-BSE images and SEM-EDS maps reveal compositional heterogeneity within individual fragments, with aluminosilicate-rich matrices containing localized concentrations of Fe, Si, Al, Ca, and O. Elemental abundances typically range up to ~47 wt% Si, ~53–71 wt% O, ≤10 wt% Fe, and ≤4 wt% Al. One fragment contains a melted quartz grain within a lithic aggregate (Figure 17E), consistent with melt incorporation during deposition.

The combination of vesicular textures, remnant PFs, and flow structures, together with aluminosilicate-dominant compositions and mineral inclusions, is consistent with rapid melting followed by high-temperature quenching. The occurrence of meltglass within lithic aggregates is consistent with formation in a high-energy environment capable of partially melting and dispersing mineral grains.

While volcanic processes can also produce glassy materials, the observed suite of features, including relict PDFs, melt-filled fractures, and association with lithic aggregates, differs from typical volcanic glasses and is not accompanied by tephra or other volcanic indicators. Considering these characteristics collectively, the meltglass fragments are most plausibly interpreted as products of high-temperature processes, such as those associated with an airburst or surface-impact event at the Younger Dryas onset.

Glass-filled lithic aggregates in the YDB layer

Lithic aggregates within a matrix of amorphous silica have been reported at several other YDB sites that also contain shocked quartz [43, 57]. However, most YDB localities have not been systematically investigated for this proxy. They have now been observed in the YDB at Kangerlussuaq (Figure 18) but not above or below it. Lithic aggregates consist of composite particles in which multiple mineral fragments are bound together into a single sand-sized grain by an amorphous cementing matrix. Such aggregates can form in high-stress geological environments where intense fragmentation is accompanied by localized melting or rapid cementation, including fault zones, volcanic settings, and impact environments, at both macro- and microscales.

In high-energy impact settings, lithic aggregates may incorporate angular fragments of quartz and other minerals welded together by isotropic, amorphous silicate material

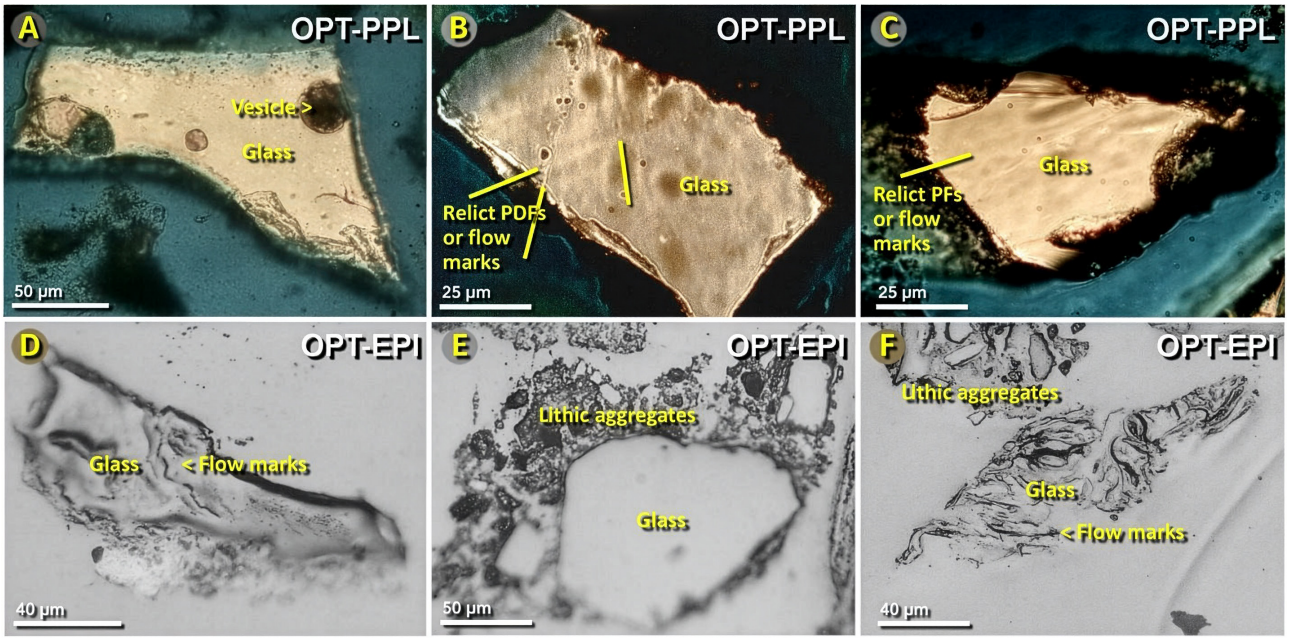


Figure 17: Meltglass fragments from the Kangerlussuaq YDB layer. (A-C) Plane-polarized transmission photomicrographs displaying vesicular structures and melted relict PDFs or high-temperature flow features. Unlike shock-deformed grains, normal quartz grains do not display parallel cleavage, as seen in these figures. (D-F) Epi-illuminated photomicrographs highlighting flow structures; (E) A meltglass fragment embedded in glass-filled lithic aggregates.

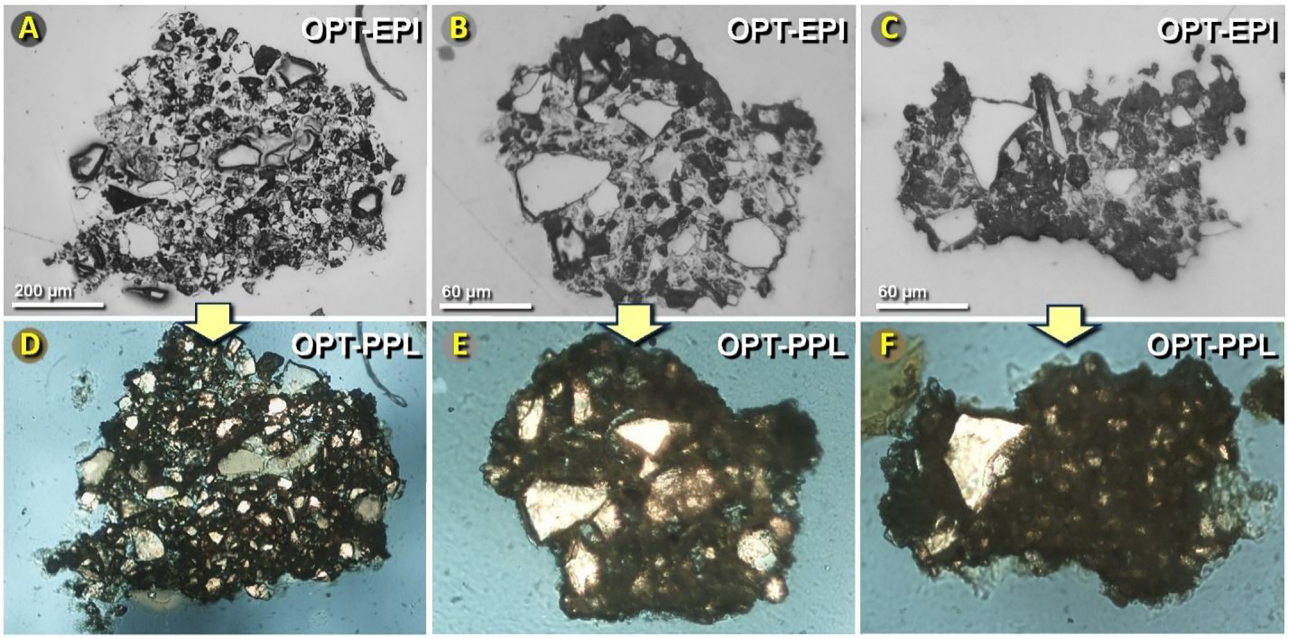


Figure 18: Glass-filled lithic aggregates composed of quartz and other mineral fragments in an amorphous silica matrix from the Kangerlussuaq YDB layer. Panels A-C: Optical epi-illuminated images of lithic aggregates. Panels D-F: Corresponding cross-polarized optical microscope images. Crossed polarizers and SEM-EDS analyses reveal that the grains are bonded by isotropic, amorphous silica, interpreted as melted SiO_2. No evidence of microcrystalline, cryptocrystalline, or hydrated silica phases was observed.

produced during transient melting and rapid quenching. When composed entirely of quartz fragments, such aggregates reflect fragmentation and re-welding of a single lithology; when multiple mineral phases are present, they record incorporation of heterogeneous target material. The binding matrix in these aggregates is commonly noncrystalline, isotropic under crossed polarizers, and locally vesicular, consistent with formation from melt rather than low-temperature cementation. Shocked quartz incorporated within lithic aggregates has been documented in impact-related deposits, including Libyan Desert Glass [69] and the YDB-aged site of Abu Hureyra, Syria [43].

We observed glass-filled lithic aggregates within the YDB layer, as illustrated in Figure 18. Optical and cross-polarized microscopy show that these angular mineral fragments are bound by isotropic material lacking internal birefringence. SEM-EDS analyses indicate that the binding matrix is dominated by SiO_2 with minor Al, Ca, and Fe contributions. High-resolution SEM imaging revealed no evidence of microcrystalline or cryptocrystalline silica phases, ruling out chert, chalcedony, agate, or quartz cement as binding agents.

SEM-EDS measurements consistently yield O/Si weight ratios <53/47 in the glass-rich domains, lower than the stoichiometric ratio for crystalline quartz. These oxygen-deficient compositions differ markedly from hydrated amorphous silica phases such as opal-A or hyalite, which typically exhibit O/Si ratios near 66/34 [92, 94, 96, 109, 112]. The absence of hydration, combined with the lack of cathodoluminescence, indicates an anhydrous, melt-derived silicate glass rather than silica precipitated through low-temperature aqueous or diagenetic processes.

Interpretation. Lithic aggregates containing angular quartz fragments welded within dense silicate glass matrices have been reported from YDB sediments [43, 57] and from several confirmed impact structures, including Ries [113], Chicxulub [114], and Popigai [115]. In these settings, high-pressure shock deformation and localized melting generate glassy matrices that bind fragmented mineral components into cohesive glass-filled aggregates. Texturally similar aggregates incorporating melted aluminosilicate glass and multiple mineral phases are likewise characteristic of short-duration, high-temperature, high-strain processes.

Alternative terrestrial origins were evaluated. Volcanic tephra and glass typically contain pumiceous or vesicular matrices and do not exhibit the dense, anhydrous silica glass observed here [116, 117]. Tectonic fragmentation produces angular grains but does not generate silica melt or glass, nor does it produce shock-related microstructures such as PDFs [118]. Frictional melting during faulting can generate pseudotachylites, but these occur as vein-like features with distinct textures and mineralogy [119]. Lightning-generated fulgurites form tubular or branching glassy structures in near-surface sediments and lack shock-metamorphic features [111, 120].

While several high-energy terrestrial processes can produce partial melting, none are known to generate

dense glass-filled lithic aggregates characterized by anhydrous, oxygen-deficient silicate glass in combination with shocked quartz. When considered alongside co-occurring YDB proxies, including meltglass, nanodiamonds, microspherules, and platinum-group element enrichments, the lithic aggregates documented here are most consistent with formation under short-duration, high-temperature, high-pressure conditions associated with a high-energy event.

Microspherules in the Younger Dryas Boundary layer

Silicon- and iron-rich microspherules have been reported at many Younger Dryas Boundary (YDB) sites across multiple continents, where they are commonly interpreted as indicators of exposure to high temperatures, such as those generated by cosmic impacts or atmospheric airbursts [16, 34, 40, 42, 58]. These spherules have been documented at more than 50 sites worldwide and occur within the YDB layer at 17 of the 19 locations where shocked quartz has also been identified. YDB spherules reported from 18 YDB sites ranged from ~5 μm to 5.5 mm in diameter, with mean sizes near 135 μm [18], and display subrounded to spherical morphologies and surface textures consistent with rapid melting and cooling [18]. Although such characteristics are often associated with high-temperature formation processes, they are not diagnostic in themselves and require contextual evaluation alongside other proxies.

Microspherules were also identified in the Kangerlussuaq YDB layer through optical microscopy, SEM, and SEM-EDS. Both silicon-rich and iron-rich particles were characterized, permitting compositional and morphological comparison with spherules reported from other YDB sites. Representative examples are shown in Figure 19. These observations provide additional evidence for evaluating the depositional environment and potential high-temperature processes at the onset of the Younger Dryas.

Interpretation. Microspherules recovered from the YDB interval at Kangerlussuaq display a range of morphologies, including smooth, teardrop-shaped, and hollow forms. Many exhibit surface flow textures and vesicular interiors, features consistent with melting followed by rapid quenching. Spherule diameters range from ~10 to 30 μm (mean ~17 μm), considerably smaller than many spherules reported at other YDB sites, where diameters may reach several millimeters (average ~135 μm) [18]. Their comparatively small size is consistent with long-range atmospheric transport from more distant melt-producing processes.

Compositional analyses indicate two principal spherule types: Si-rich and Fe-rich. The Fe-rich spherule in Figure 19A contains ~80 wt% Fe and ~20 wt% O, consistent with wüstite, an oxygen-deficient FeO phase uncommon at Earth's surface but present in some meteorites and impact structures. The Si-rich spherule in Figure 19B is composed

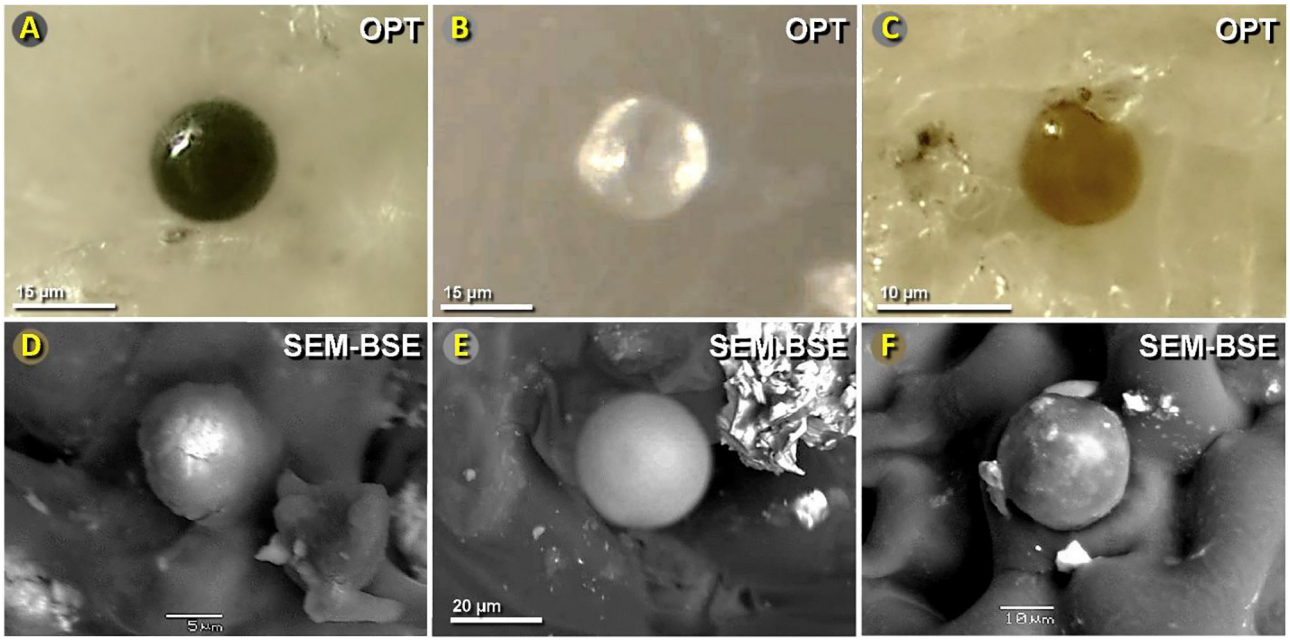


Figure 19: Images of microspherules from the YDB layer. Panels A-C are optical images. Panels D-F are SEM-BSE images. (A) Fe-rich spherule (~80 wt% Fe, ~20 wt% O), consistent with wüstite. (B) Si-rich spherule (~95 wt% Si and O), isotropic and melted. (C) High-silica spherule with Fe, Al, Cr (3800 ppm), and Ni (1500 ppm). (D) FeO spherule with aluminosilicate coating is enriched in Cr and Ni. (E) High-silica spherule (O = 71.39 wt%, Si = 26.99 wt%, S = 1.62 wt%). (F) Coated Fe-rich spherule; coating composition: O = 54.99, Si = 41.50, Ca = 1.38, Mn = 1.84, Fe = 0.29 wt%).

primarily of Si and O (≈95 wt%), with minor Fe and Al, and is isotropic under crossed polarizers, consistent with a noncrystalline, melt-derived origin. The aluminosilicate spherule in Figure 19C contains elevated Fe (35.91 wt%), Al (3.81 wt%), and Si (3.44 wt%), with trace Cr (3800 ppm) and Ni (1500 ppm). Another FeO spherule (Figure 19D) exhibits a silicate coating that is similarly enriched in Cr and Ni. These Cr and Ni abundances exceed typical crustal values and are compatible with high-temperature processes involving mixed terrestrial and potentially extraterrestrial components. Additional examples include a high-Si spherule (Figure 19E) and an Fe-rich spherule with a silicate-rich coating (Figure 19F).

The Kangerlussuaq spherules differ In both composition and texture from micrometeorite ablation spherules produced during atmospheric entry. Cosmic spherules derived from iron meteorites typically exhibit high Ni contents (≥5 wt%), whereas those derived from chondritic meteorites commonly contain elevated MgO (>10 wt%) due to olivine-pyroxene melting [121–124]. The Kangerlussuaq spherules lack these diagnostic signatures. Instead, their compositions are dominated by FeO or SiO_2, with only moderate or trace Cr and Ni, and minimal Mg. These patterns suggest formation under thermal conditions distinct from those of steady-state meteoritic ablation.

Morphologically, the spherules also lack common ablation-related features such as mineralogical zoning, magnetite-rich rims, or progressive oxidation textures that develop during prolonged atmospheric transit [121–124]. Instead, their vesicular textures, oxygen-deficient iron-oxide phases, and amorphous silica compositions are consistent with melting under short-duration, high-temperature conditions.

The collective characteristics of the Kangerlussuaq microspherules, including their small diameters, vesicular form, amorphous silica and wüstite phases, and elevated Cr and Ni, indicate formation under extreme thermal disequilibrium. These features closely resemble those reported in microspherules from other YDB sites. Their co-occurrence with shocked quartz and other high-temperature proxy materials within the same stratigraphic layer is consistent with production during a transient, high-energy event at the onset of the Younger Dryas.

Carbon spherules and glasslike carbon in Younger Dryas Boundary ice

Carbon spherules and glassy carbon are two types of carbon-rich materials commonly found within the YDB layer at multiple sites across North America and Europe [16, 23, 34]. Alternative interpretations of some carbon spherules as fungal sclerotia have been proposed in the literature [125], but counterarguments report that an origin as sclerotia cannot explain the presence of embedded nanodiamond particles [23, 34]. These materials are present at 15 of 19 YDB sites that also contain shocked quartz (Figure 1); the other four 4 of 19 sites have not been investigated. Carbon spherules are typically hollow, rounded to ovoid in shape, and composed predominantly of elemental carbon. They frequently exhibit surface cracking, internal vesicles, and layered morphologies, consistent with rapid heating and cooling associated with biomass combustion.

Glasslike carbon occurs as irregular, dense fragments, typically millimeter-scale, with smooth to conchoidal fracture surfaces and no observable cellular structure, thereby distinguishing it from cellular charcoal. SEM-EDS and Raman spectroscopy have confirmed its high-carbon composition and amorphous structure, and occasionally elevated levels of platinum-group elements (PGEs), suggesting the incorporation of ET material.

Both carbon spherules and glasslike carbon are considered to have been produced during widespread biomass burning, as inferred from their peak abundances at most YDB sites investigated [45, 46]. We also observed these carbon forms in the YDB layer at Kangerlussuaq. Images are shown in Figure 20. SEM-BSE imaging documented various morphologies of the Kangerlussuaq YDB carbon spherules, including hollow and vesicular structures (Figure 20A–20F). Additional SEM-BSE images (Figure 20G–20I) depict representative fragments of glasslike carbon.

Elemental analysis using SEM-EDS showed that both carbon spherules and glasslike carbon are primarily composed of carbon (85–99 wt%), along with oxygen (1–10 wt%), silicon (1–8 wt%), and aluminum (1–4 wt%). While some YDB carbon spherules have been reported to contain nanodiamonds [23], we did not examine their presence in Kangerlussuaq spherules.

Interpretation. The morphology and composition of carbon spherules and glasslike carbon recovered from the Kangerlussuaq YDB interval indicate exposure to high temperatures. Their rounded forms, vitrified textures, and internal structures are consistent with carbonaceous material that has undergone intense thermal alteration. Similar carbon phases have been reported at multiple YDB sites and interpreted as products of high-temperature processes affecting biomass [45, 46].

Independent paleochemical records from three Greenland ice cores provide additional context. Concentrations of ammonium and nitrate, widely used as indicators of large-scale biomass burning, show marked increases at the onset of YD cooling [76, 79, 126, 127]. The co-occurrence of thermally altered carbon particles in the Kangerlussuaq samples with elevated biomass-burning proxies in regional ice-core records is consistent with a significant, high-temperature combustion event at this time. While several mechanisms could generate widespread biomass burning, these combined observations are compatible with scenarios involving rapid, high-energy processes, including the possibility of an impact-related airburst at the Younger Dryas onset.

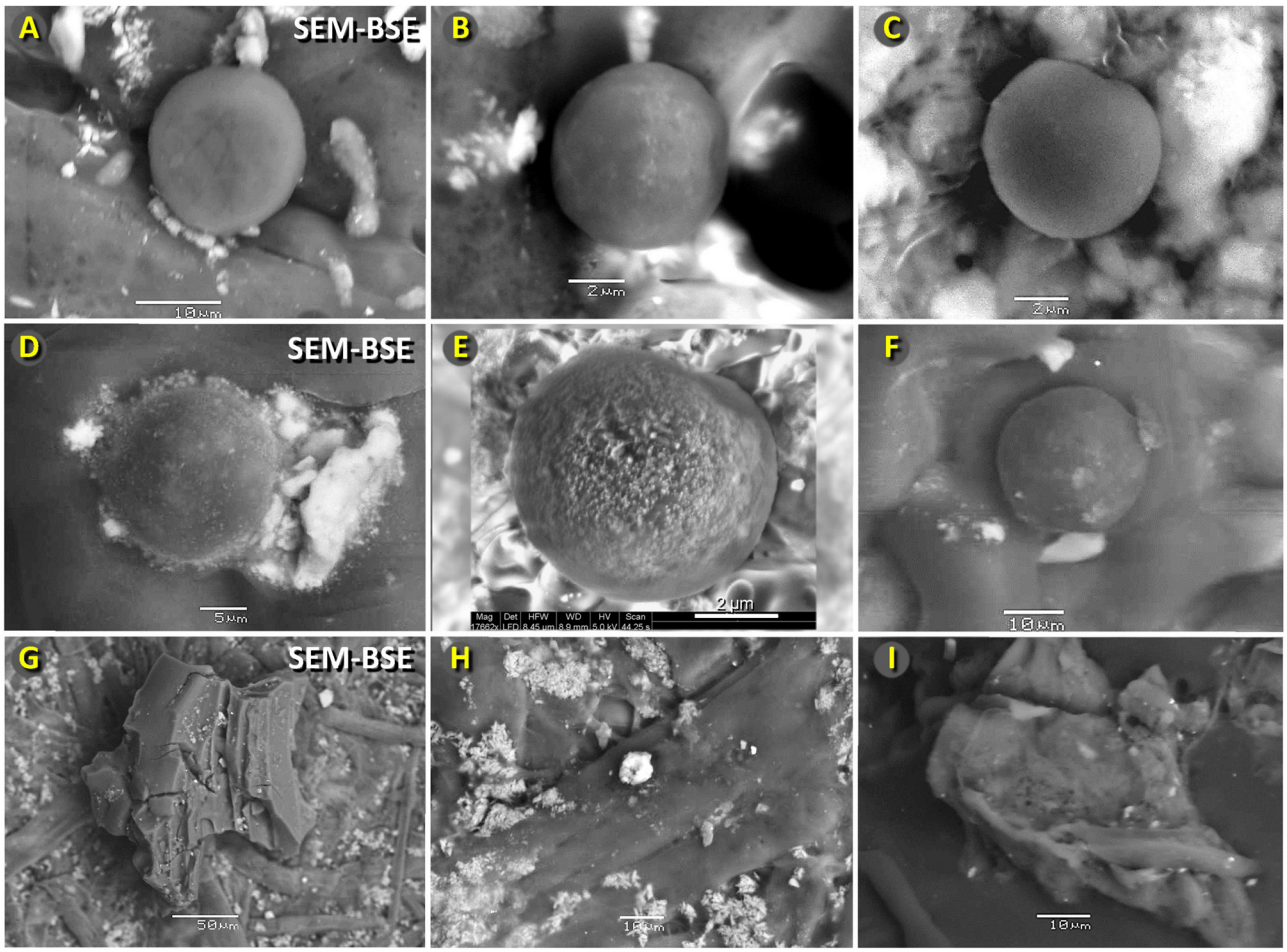


Figure 20: Carbon-rich particles recovered from the YDB layer. Panels A-F: SEM-BSE images of carbon spherules showing hollow and vesicular textures. Panels G-I: SEM-BSE images of glasslike carbon fragments. Elemental compositions range from 85–99 wt% C, with minor amounts of O (1–10 wt%), Si (1–8 wt%), and Al (1–4 wt%). The characteristics of these materials are consistent with their formation through high-temperature biomass burning.

Nanoparticles enriched in platinum-group elements and siderophile metals

To evaluate whether the Younger Dryas onset interval contains a nanoparticle population with a potential extraterrestrial (ET) or high-temperature component, we examined particle-resolved mass concentrations of platinum-group elements (PGEs) and associated siderophile metals using SP-ICP-TOF-MS. Unlike lithophile-dominated elements that primarily track terrestrial dust sources, PGEs, Ni, Co, and Re are strongly enriched in meteoritic materials relative to average crustal compositions and can be concentrated during high-temperature vaporization, condensation, and nanoparticle-forming processes. Accordingly, these elements provide sensitive tracers for detecting a chemically distinct nanoparticle population that may include a non-crustal component or material fractionated in an impact-generated plume. Here, we compare PGE sum, Ir, Pt, Os, Pd, Ni, Co, and Re mass concentration profiles across the Bølling-Allerød, Younger Dryas, and Holocene intervals to assess whether a distinct siderophile-rich nanoparticle peak occurs at or immediately above the Younger Dryas Boundary (YDB) (Figure 21).

Interpretation. The PGE-bearing and siderophile nanoparticle records display a coherent and diagnostic pattern: a sharp enrichment centered at ~5.2 m, immediately above the YDB layer at ~5.5 m. This peak is expressed across multiple independent elements, including Ir, Pt, Os, Pd, Ni, Co, and Re, as well as the summed PGE signal. The synchronicity of these profiles argues against random analytical scatter and instead indicates a stratigraphically discrete increase in siderophile-rich nanoparticles.

The magnitude of enrichment relative to the YDB layer ranges from ~2.3× to ~15.9×, with the strongest response in Os and substantial increases in Ir, Pt, Re, Ni, and Co. Because these elements are enriched in extraterrestrial materials relative to average crustal compositions, their coordinated

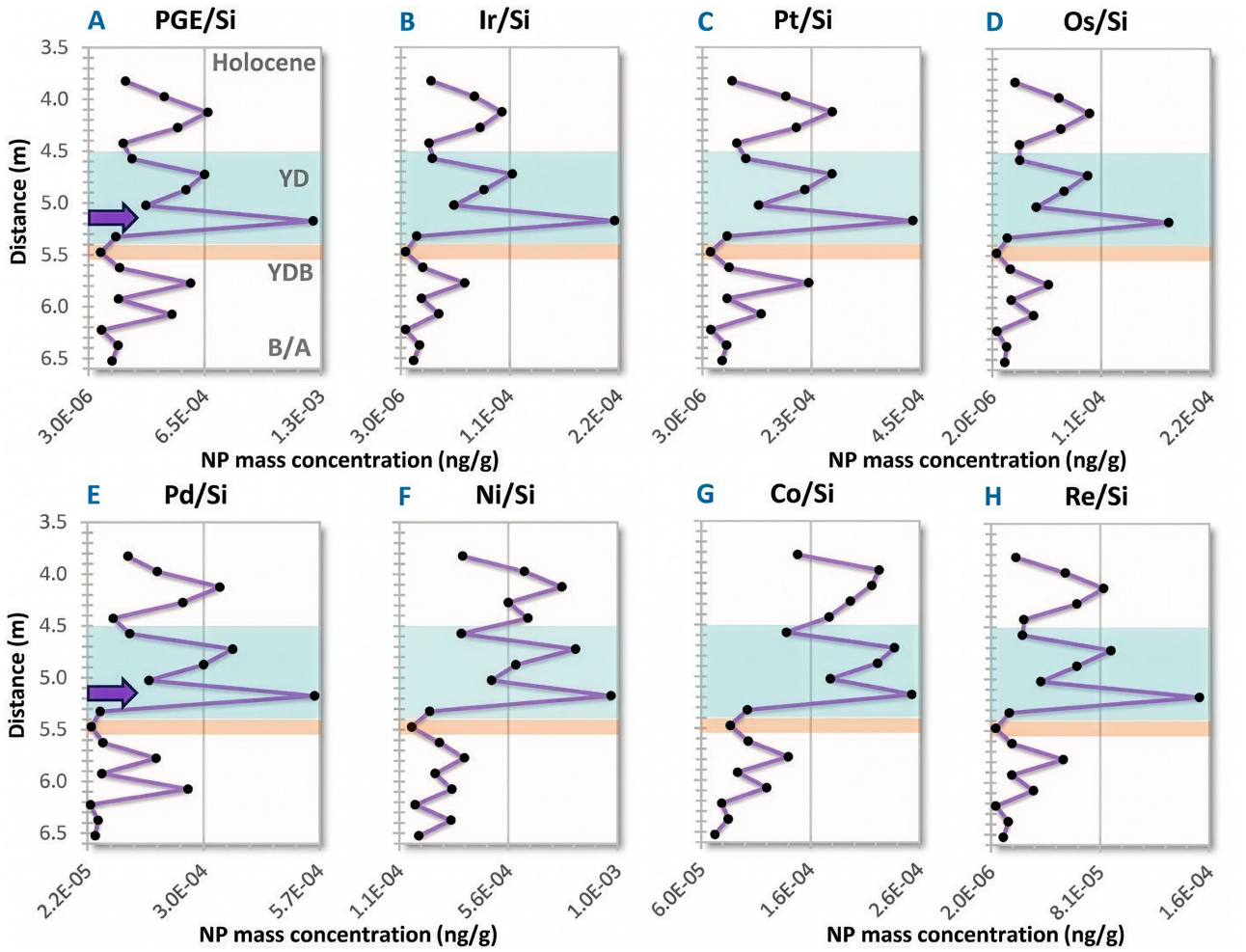


Figure 21: Platinum-group element-bearing nanoparticles show a pronounced enrichment above the Younger Dryas Boundary. (A-H) SP-ICP-TOF-MS mass concentration profiles of PGE sum, Ir, Pt, Os, Pd, Ni, Co, and Re across the Bølling-Allerød (B/A), Younger Dryas (YD), and Holocene intervals. The YD interval is shaded in blue, and the impact-proxy-rich YDB layer is marked by the orange band at ~5.5 m. All eight profiles exhibit a pronounced peak centered near ~5.2 m, immediately above the YDB layer. Relative to the YDB layer at ~5.5 m, the overlying ~5.2 m interval is enriched by factors of ~4.2 for PGE sum, ~5.3 for Ir, ~5.9 for Pt, ~15.9 for Os, ~2.3 for Pd, ~3.8 for Ni, ~3.9 for Co, and ~5.5 for Re. For comparison, extraterrestrial materials are enriched relative to average crustal abundances by approximately 7,500× for total PGEs, 24,000× for Ir, 1,500× for Pt, 15,950× for Os, 1,100× for Pd, 331× for Ni, 34× for Co, and 143× for Re. These relationships highlight the strong siderophile affinity of these elements and their utility for identifying a potentially non-crustal or high-temperature nanoparticle component.

increase provides a sensitive indicator of a chemically distinct component. However, the observed concentrations do not suggest pure meteoritic material; rather, they are consistent with a dominantly terrestrial nanoparticle population containing a minor but detectable siderophile-rich or high-temperature fraction.

The stratigraphic position of the peak is important. The maximum occurs above, rather than within, the YDB layer, suggesting that the siderophile-rich nanoparticles were not deposited solely with the initial boundary material. Instead, the offset is consistent with short-lived delayed fallout of fine particles following atmospheric injection, vapor-phase fractionation, condensation, or prolonged suspension of nanoscale material after the initial event.

The coherence of the signal across PGEs and associated siderophile elements also distinguishes this pattern from ordinary terrestrial dust variation. A simple increase in crustal dust should not preferentially produce a sharp, coordinated enrichment in elements that are strongly depleted in average crust relative to extraterrestrial materials. The data are therefore consistent with introduction of a chemically distinct nanoparticle population formed or concentrated under elevated-temperature conditions, such as those expected in an impact-generated vapor plume or airburst-related atmospheric perturbation.

Taken together, these results indicate that the onset of the Younger Dryas was associated not only with increased atmospheric dust flux, but also with a discrete, short-lived

enrichment in PGE-bearing and siderophile nanoparticles. This pattern supports the presence of an event-driven, high-energy component superimposed on the broader climatic transition.

PGE ratio systematics reveal a stratigraphically confined enrichment near the YDB

To further evaluate whether the nanoparticle enrichment observed above the Younger Dryas Boundary (YDB) reflects simple increases in dust flux or the addition of a chemically distinct component, we examined platinum-group element (PGE) ratios normalized to the YDB layer at 5.5 m (Figure 22). This approach minimizes the local background signal and isolates relative changes in PGE composition across the stratigraphic sequence, allowing direct comparison between the nanoparticle peak interval (~5.2 m), the YDB layer (~5.5 m), and underlying samples.

Interpretation. The normalized PGE patterns reveal a clear and internally consistent stratigraphic structure. All measured PGEs are strongly enriched in samples above the YDB relative to the boundary layer itself and to underlying ice, while the YDB layer plots at or near baseline values. This confirms that the boundary layer does not represent the peak of siderophile deposition, but instead marks the onset of a subsequent enrichment phase.

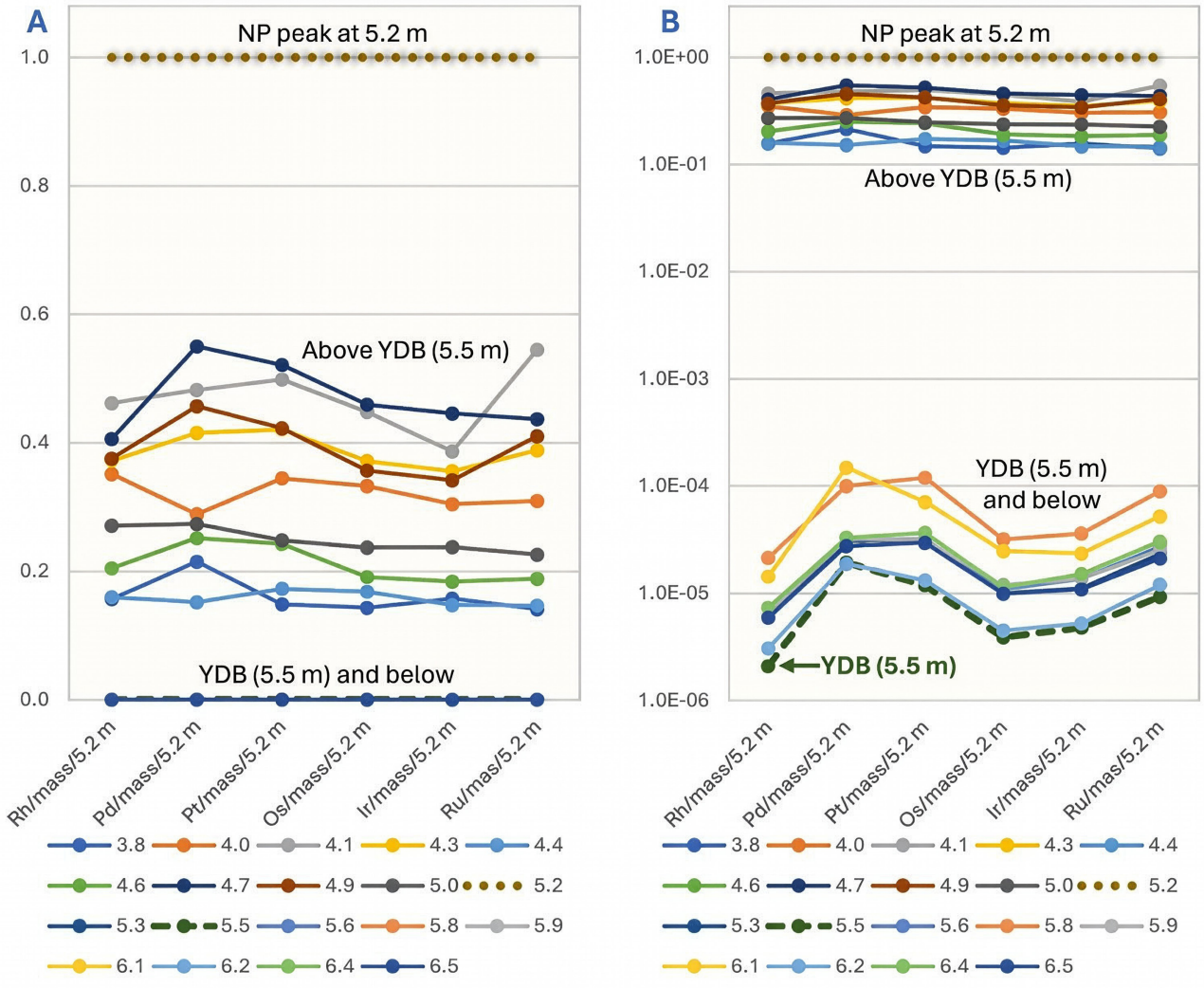


Figure 22: Stratigraphic PGE ratio patterns normalized to the Younger Dryas Boundary (YDB) layer. (A) Linear-scale comparison of PGE ratios (Rh, Pd, Pt, Os, Ir, Ru normalized to total mass) for samples above, within, and below the YDB. Values are normalized to the 5.2 m nanoparticle peak. The YDB layer at ~5.5 m and underlying samples plot near zero, whereas samples above the YDB show consistently elevated values. (B) Log-scale representation of the same data highlighting relative enrichment patterns. All PGEs exhibit enrichment above the YDB relative to the boundary layer and underlying samples. The enrichment is coherent across multiple elements and depths, with modest internal fractionation among individual PGEs. The nanoparticle peak at ~5.2 m is marked and represents the maximum expression of the signal.

The coherence of the enrichment across Rh, Pd, Pt, Os, Ir, and Ru indicates that the signal is not driven by variability in a single element or analytical noise. Rather, it reflects a multi-element siderophile enrichment affecting the nanoparticle population as a whole. This behavior is consistent with the introduction of a chemically distinct component superimposed on the background dust signal, rather than simple amplification of terrestrial material.

Importantly, the enrichment is expressed across multiple samples above the YDB, not solely at the peak interval (~5.2 m). This indicates that the process responsible for the PGE enrichment operated over a finite interval rather than as an instantaneous deposition event. The persistence of elevated values supports a temporally structured sequence involving atmospheric residence, transport, and delayed fallout of fine-grained material.

At the same time, the patterns are not perfectly flat across the PGE suite. Subtle differences among elements—such as relative suppression or enhancement of individual PGEs—indicate mild fractionation. This internal structure is consistent with high-temperature processes, including vaporization and condensation, in which PGEs partition according to volatility and nucleation behavior. Refractory PGEs (Os, Ir, Ru) tend to behave coherently, while more volatile or chalcophile-associated elements (e.g., Pd) may show relative deviation.

Taken together, these observations demonstrate that the PGE anomaly above the YDB reflects a coherent, stratigraphically confined enrichment in siderophile-bearing nanoparticles that is compositionally distinct from background dust. The normalization approach isolates this residual component and shows that it is best explained by the addition of material formed or modified under elevated-temperature conditions, consistent with atmospheric input from a possible airburst/impact superimposed on the broader Younger Dryas climate transition.

Platinum group element (PGE) nanoparticles in Greenland ice.

To investigate potential shifts in atmospheric ET input and dust provenance across both YD climatic transitions, we employed SP-ICP-TOF-MS to quantify and characterize PGE-rich nanoparticles preserved in Greenland ice. This high-resolution technique enables the detection of individual particles and the determination of their number, elemental composition, and mass on a per-particle basis. The resulting dataset provides a slope-distance-resolved record of PGE nanoparticle abundance and size distribution across the Holocene, YD, and Bølling-Allerød intervals. The PGE data exhibit a bimodal mass distribution: small-mass nanoparticles are dominated by Rh, Os, and Ir, while larger-mass nanoparticles are enriched in Pt, Pd, and Ru. The results are shown in Figure 23.

Interpretation. To investigate patterns in PGE behavior, we applied unsupervised k-means clustering (k = 2) to the mass distributions of PGE-bearing nanoparticles. For all six PGEs, clustering produced two statistically distinct and robust particle populations, each with high silhouette scores for k = 2. Rh, Os, and Ir form a smaller-mass population, whereas Pt, Ru, and Pd form a larger-mass population. For example, Pt nanoparticles partition into ~497 "small" particles (~4–6 × 10^{-16} g) and ~312 "large" particles (~6 × 10^{-16}–6 × 10^{-15} g). Ir, Os, and Rh show analogous bimodal distributions within similar mass ranges.

All measured PGEs also exhibit coherent enrichment relative to background levels: Pt (1.96×), Ir (1.82×), Rh (1.80×), Ru (1.78×), Os (1.74×), and Pd (1.44×). This coordinated behavior contrasts with typical terrestrial fractionation patterns [128, 129]. The iridium enrichment of 1.82× is noteworthy, given Ir's long-standing role as a sensitive indicator of extraterrestrial input since the K-Pg discovery [130]. Peak Ir concentrations reach 1.61 ppb near the YD onset, coinciding with maximum PGE abundances.

The observed bimodality (Figure 23) is consistent with fractionation during high-temperature condensation or nucleation, in which refractory PGEs (Ir, Os, Rh) condense first into small nuclei. In contrast, more volatile PGEs (e.g., Pd) condense later or aggregate onto existing particles. This pattern aligns with established condensation sequences in cosmochemical systems [131–133].

We also evaluated whether volcanism could account for these enrichments. No major eruptions are known for this region during the relevant interval [45, 83], and no volcanic tephra was detected in our samples or at numerous other YDB sites [59, 134]. While volcanic plumes can generate PGE-rich nanoparticles, their signatures typically include co-associated tephra and predictable PGE fractionation patterns. They also require a known eruptive source, which is absent here. Although high-temperature volcanic condensation could produce two size regimes, volcanism alone cannot account for the stratigraphically restricted peak or the accompanying suite of impact-related proxies.

The nanoparticle record reveals persistent bimodal PGE populations throughout the section, consistent with continuous background dust flux from terrestrial sources and steady-state cosmic dust deposition. During the late Bølling-Allerød, dust was primarily Saharan in origin [85]. During the YD, Saharan dust remained important (~50%), but East Asian deserts contributed substantially [86]; in the early Holocene, Saharan input declined while East Asian and local sources increased [85]. These shifts are consistent with the broader patterns of nanoparticle provenance observed in the sequence.

Cosmic dust provides an additional constant background source. ET nanoparticles, including siderophile metals and PGEs, are continuously delivered to polar ice sheets [135, 136], thereby producing a relatively stable baseline flux. The widespread presence of both PGE size classes throughout the record is consistent with this steady-state input.

However, the most prominent increases in both small and large PGE nanoparticles occur during the YD, forming a

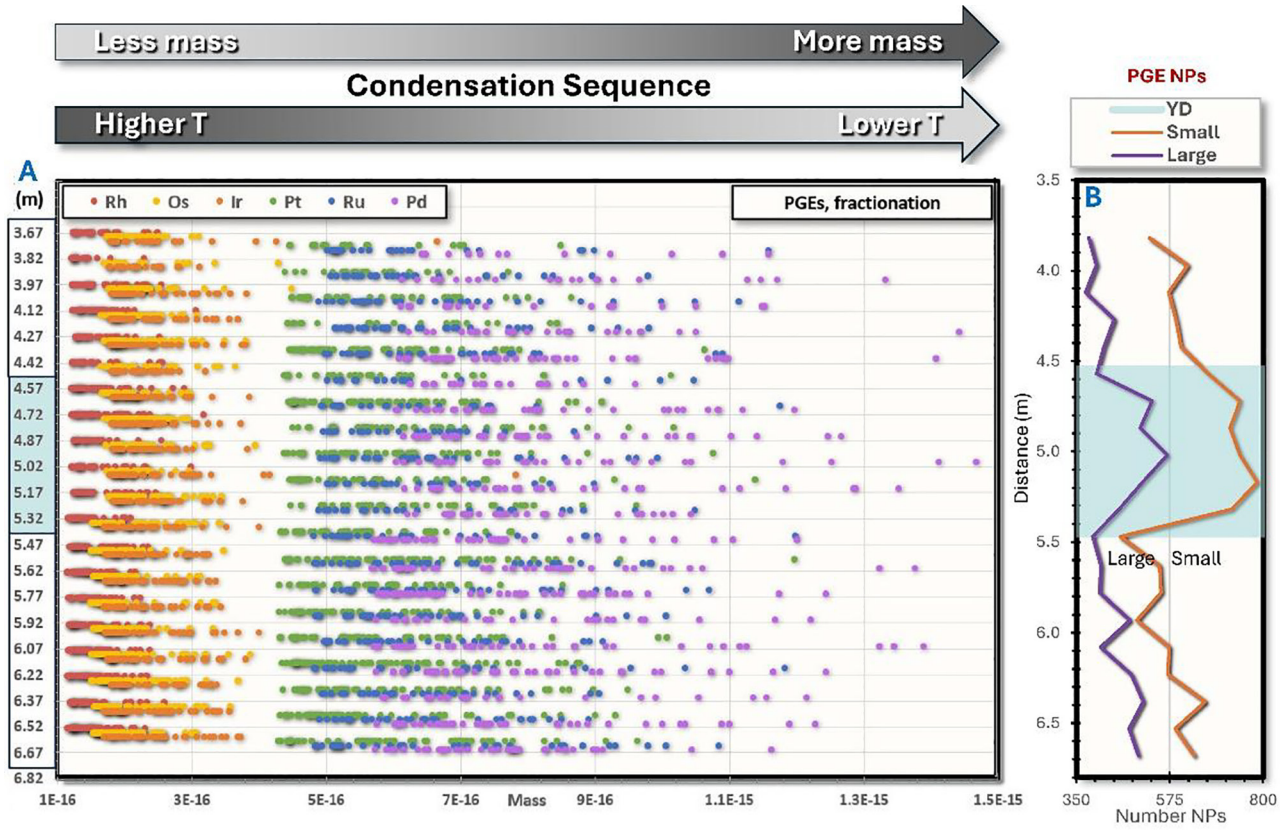


Figure 23: Bimodal mass distribution of platinum-group element (PGE) nanoparticles in Greenland ice. SP-ICP-TOF-MS analyses plotted against slope distance across the Bølling-Allerød, Younger Dryas, and early Holocene intervals reveal two distinct size populations of PGE-rich nanoparticles preserved in the Greenland Ice Sheet. Panel A: Individual nanoparticles are ranked by mass on the x-axis and depth on the y-axis. Particle mass increases from left to right (top arrow); inferred particle condensation temperatures decrease from left to right. Elemental values are offset slightly to enhance readability. Unsupervised k-means clustering (k = 2) applied to individual nanoparticle mass data confirms statistically robust bimodality for all six measured PGEs. Smaller-mass nanoparticles are dominated by refractory elements (Rh, Os, Ir), while larger-mass particles are enriched in more volatile PGEs (Pt, Pd, Ru). Panel B: The total number of nanoparticles was plotted against slope distance by bi-modal PGE population: Rh, Os, Ir in orange; Pt, Pd, Ru in purple. These results indicate that smaller PGE nanoparticles are approximately 50% more abundant than the larger nanoparticles, and the difference in number between them increases at the YD onset. This bimodal distribution likely reflects high-temperature fractionation during condensation or nucleation, consistent with cosmochemical condensation sequences. The most prominent enrichment occurs during the Younger Dryas interval (5.5–4.7 m), where coincident increases in particle number and mass suggest a transient influx of extraterrestrial material, superimposed on a continuous background of terrigenous and cosmic dust. The compositional coherence and size-based fractionation of PGEs within this interval are consistent with a high-energy airburst/impact event. Note the for any given depth, the plotted values for each PGE are offset to improve visualization.

broad peak between 5.5 and 4.7 m that exceeds expectations based on background terrestrial or cosmic dust fluxes. Two processes appear to have operated:

1. A short-lived increase at the YD onset, which may reflect a pulse of ET-derived material consistent with an airburst or impact event, an interpretation consistent with the behavior of PGEs in meteoritic debris, where vapor-phase condensation during hypervelocity impacts produces distinct size-separated populations [137, 138].

2. A more gradual decline through the YD, likely reflecting climate-driven changes in terrestrial dust sources and reworked ET material.

Large impacts are known to generate PGE-rich nanoparticles and spherules; for example, the Chicxulub impact produced a global Ir anomaly and nanocrystalline Pt-Ir particles within melt spherules [137]. A similar pulse, superimposed on a continuous background of inputs, could have generated the particle cluster observed in Greenland.

The anomalous PGE-rich interval at Kangerlussuaq is consistent with enrichments reported at other YDB sites worldwide, including GISP2 in Greenland [87], multiple sites in North America [42, 59, 134], and a site in South America [60]. The absence of corresponding increases in crustal-element proxies (e.g., K, Ba, Ti) and the decline in several lithophile ratios suggest that the PGE anomaly is not solely attributable to terrestrial dust sources [139, 140].

In summary, the bimodal PGE mass distributions, their coordinated enrichment, and their stratigraphic concentration near the YD onset are consistent with a two-stage signal: (1) a short-term input of PGE-rich material potentially derived from an ET airburst or impact, superimposed on (2) a variable but continuous flux from Saharan, East Asian, and local terrestrial sources, as well as steady cosmic dust accretion.

Residual PGE ratios are consistent with a metal-rich extraterrestrial component

To further constrain the nature of this enrichment, we estimated a first-order residual component by subtracting the background composition (GR-99) from the NP peak composition (GR-101) as a simple end-member approximation. PGE ratios calculated from this residual were then compared with reference fields for chondrites, iron meteorites, achondrites, and Martian meteorites (Figures 24 and 25).

In multiple independent ratio-ratio diagrams, the residual component plots distinctly outside the Greenland whole-ice data cluster and instead fall within or adjacent to meteorite fields. This systematic displacement indicates that the YDB signal cannot be explained solely by enhanced deposition of background atmospheric dust. Rather, it reflects the addition of a compositionally distinct, metal-rich, ET-like component to the background dust. Although the residual approach does not uniquely identify the source material and is sensitive to background selection and analytical uncertainty, the convergence of the residual composition toward meteorite-like ratios across several diagrams provides consistent evidence for a non-crustal contribution.

Interpretation. The ratio-ratio diagrams in Figures 24 and 25 provide a first-order assessment of the compositional character of the inferred YDB component by isolating a residual signal relative to the Greenland background. In all panels, the residual composition consistently shifts toward extraterrestrial reference fields, particularly those associated with iron meteorites and metal-rich ET materials.

This systematic displacement is significant for two reasons. First, it demonstrates that the YDB signal cannot be explained by enhanced deposition of background atmospheric dust alone. The residual component occupies a separate region of compositional space, consistent with the addition of a chemically distinct component. Second, the repeated convergence of the residual toward iron meteorite fields across multiple independent element ratios suggests enrichment in siderophile elements characteristic of metal-bearing extraterrestrial material.

At the same time, the residual does not fall exclusively within any single meteorite field. Instead, it occupies positions that vary between diagrams, sometimes overlapping irons and at other times approaching chondritic or mixed fields. This behavior indicates that the YDB component is unlikely to represent a single, homogeneous source. Rather, it is more consistent with a heterogeneous mixture of phases, including a metal-rich component and a more silicate- or volatile-influenced component. Such variability is expected if the material was modified by high-temperature processes, where differential volatilization and condensation can fractionate PGEs and redistribute them among multiple particle populations.

Importantly, the residual approach is inherently sensitive to background selection and analytical uncertainty and therefore does not uniquely identify the source material. However, the consistency of the displacement across multiple independent ratio-ratio spaces provides robust evidence that the YDB nanoparticle peak reflects the addition of a non-crustal, siderophile-enriched component to the Greenland system.

These results establish that the YDB signal is compositionally distinct from both the Greenland background and typical terrestrial reservoirs, and they suggest further evaluation using complementary metrics that integrate both elemental fractionation and absolute siderophile enrichment. This is addressed in the following analysis of PGE fractionation versus Ir/Fe, which provides an independent framework for comparing the Greenland nanoparticle population with terrestrial and extraterrestrial materials.

PGE fractionation and Ir/Fe constraints on the origin of the YDB nanoparticle population

To further constrain the origin of the platinum-group element (PGE)-bearing nanoparticle population identified near the Younger Dryas Boundary (YDB), we compare particle-resolved geochemical signatures with published compositional fields for terrestrial and extraterrestrial materials (Figure 26). This comparison uses two complementary metrics: (i) the ratio of refractory to more volatile PGEs, expressed as (Os+Ir+Ru)/(Rh+Pd+Pt), and (ii) Ir/Fe, a robust indicator of siderophile enrichment. Together, these parameters distinguish between crustal, mantle-derived, and extraterrestrial reservoirs and provide a framework for evaluating whether the Greenland nanoparticle population reflects background atmospheric dust, continuous extraterrestrial input, or a discrete event-related component.

This approach builds on earlier results demonstrating that the Greenland PGE nanoparticles form a distinct population that is compositionally and stratigraphically decoupled from the broader, climate-driven dust signal.

Interpretation. The PGE fractionation-Ir/Fe relationship provides a compact and diagnostic framework for evaluating the origin of the Greenland nanoparticle population. Several key features emerge.

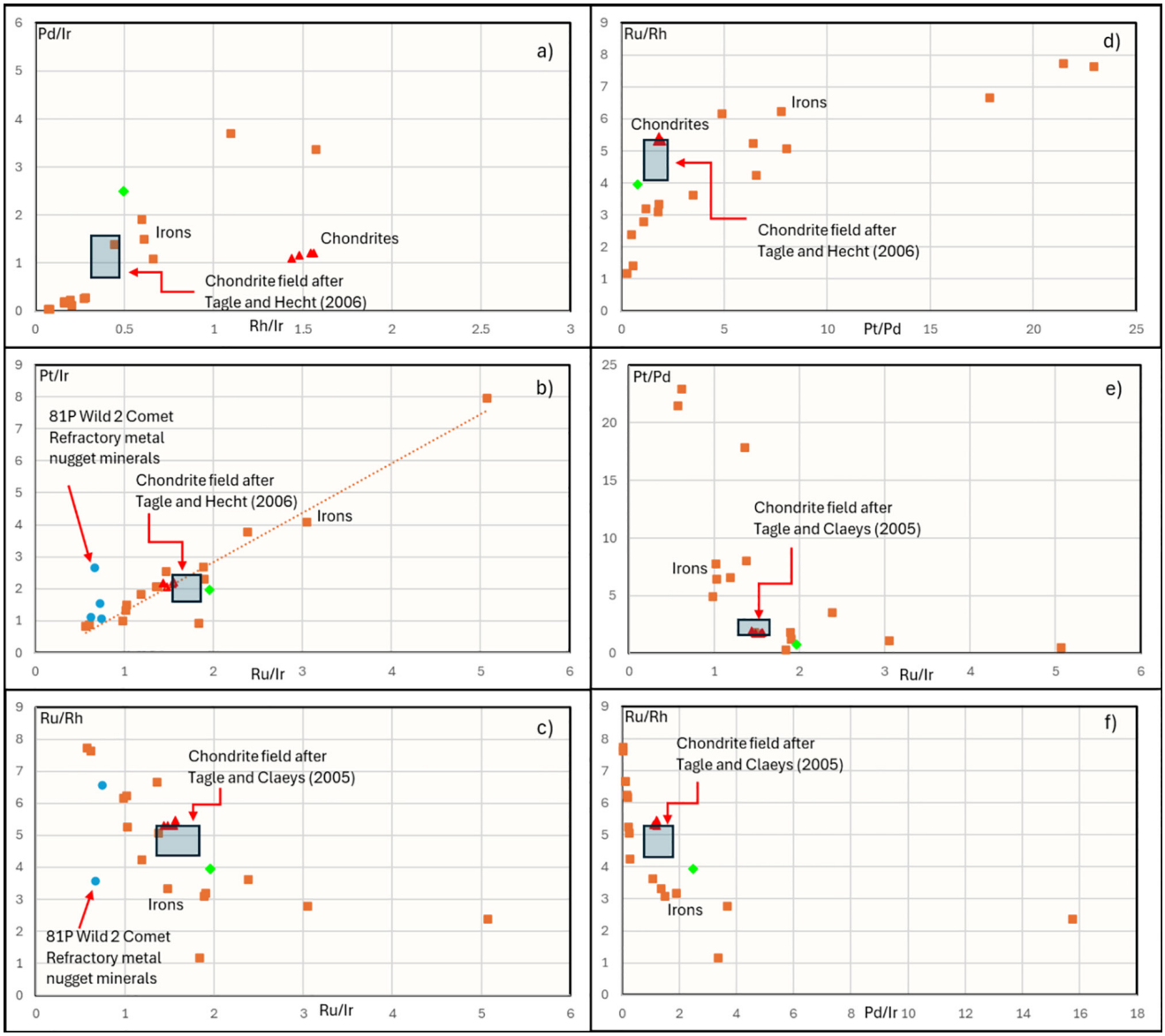


Figure 24: PGE ratio-ratio diagrams comparing the inferred residual YDB component with Greenland whole-ice data and reference extraterrestrial fields. The residual component was estimated by subtracting the YDB sample (GR-99) from the sample containing the NP peak (GR-101) -- this sample is bright green and diamond-shaped. Panels show (A) Pd/Ir versus Rh/Ir, (B) Pt/Ir versus Ru/Ir, (C) Ru/Rh versus Ru/Ir, (D) Ru/Rh versus Pt/Pd, (E) Pt/Pd versus Ru/Ir, and (F) Ru/Rh versus Pd/Ir. The inferred YDB residual component plots within or near the iron meteorite fields in multiple diagrams. Reference fields for chondrites and irons are shown for comparison. Note that these fields in this figure and the next are based on published third-party data but represent only approximate ranges for mixed particle populations. They are not intended to define strict compositional boundaries.

First, all Greenland samples plot far above terrestrial reservoirs in Ir/Fe. Mantle, crustal, and basaltic compositions are restricted to Ir/Fe values of ~10^{-10} to 10^{-8}, whereas the Greenland nanoparticles span ~10^{-5} to ~10^{-4}. This offset of several orders of magnitude precludes a purely terrestrial origin and indicates a persistent contribution from siderophile-enriched material.

Second, the Greenland data cluster exhibits consistently sub-chondritic (Os+Ir+Ru)/(Rh+Pd+Pt) ratios (~0.5–0.8), consistent with relative enrichment of Pt-Pd-Rh compared to Os-Ir-Ru. This behavior differs from unfractionated chondritic material, which typically plots near unity, and instead reflects fractionation processes affecting PGE distributions. Such fractionation is consistent with high-temperature vaporization and condensation, where more volatile PGEs are preferentially enriched in larger or later-forming particles, while refractory PGEs are concentrated in smaller or earlier condensates. This interpretation is independently

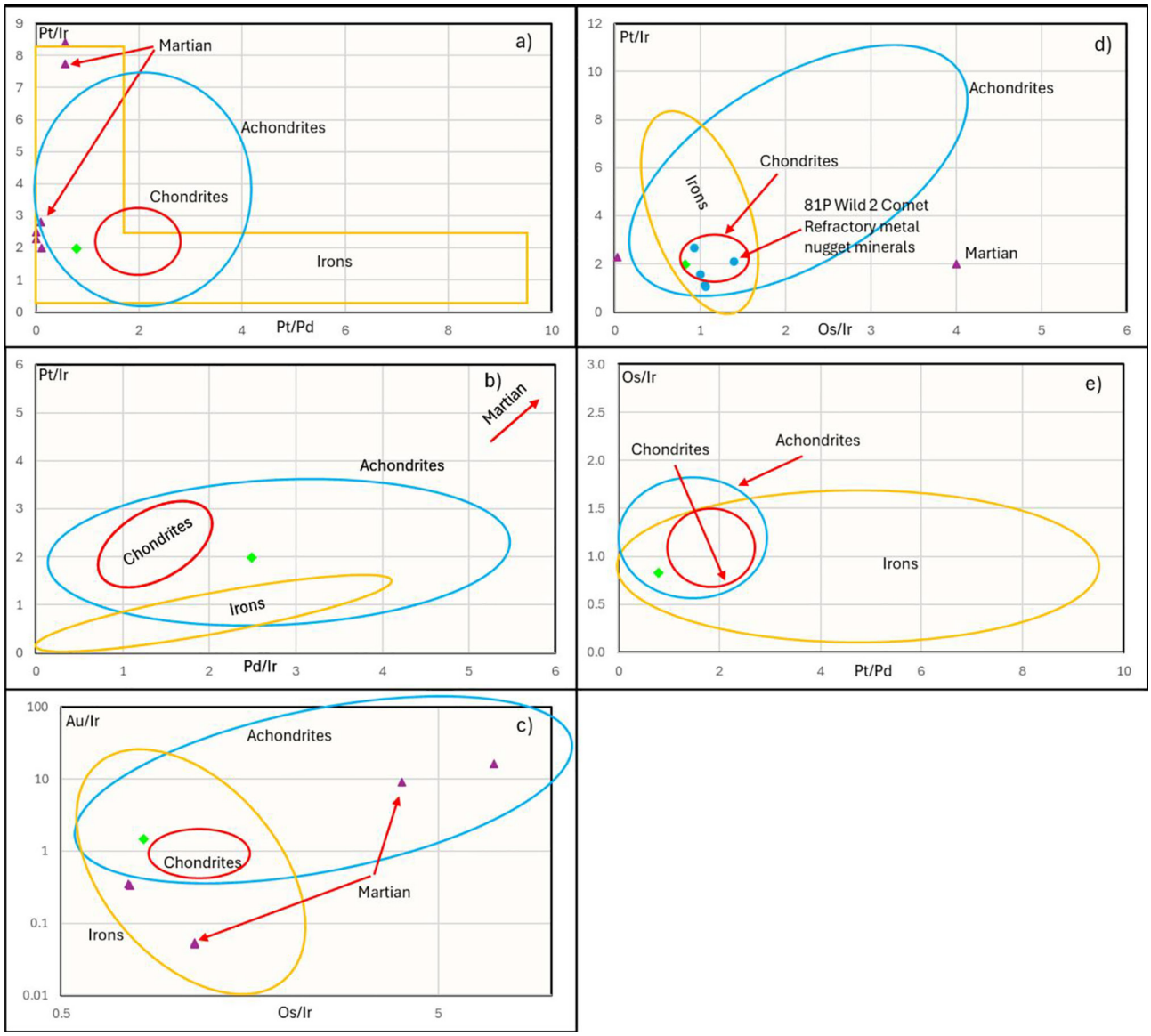


Figure 25: Additional PGE ratio-ratio diagrams comparing the inferred residual YDB component with Greenland whole-ice data and literature fields for extraterrestrial materials. Panels show (A) Pt/Ir versus Pt/Pd, (B) Pt/Ir versus Pd/Ir, (C) Au/Ir versus Os/Ir, (D) Pt/Ir versus Os/Ir, and (E) Os/Ir versus Pt/Pd. In these plots, the residual YDB component (NP peak; green diamond) falls within or close to the iron meteorite fields and remains distinct from the Greenland background data, supporting the interpretation that the added YDB component is compositionally different from normal atmospheric deposition and is consistent with a metal-rich, non-crustal component.

supported by the observed bimodal nanoparticle population, in which smaller particles are enriched in Rh-Os-Ir and larger particles in Pt-Pd-Ru.

Third, the majority of non-YDB samples define a relatively tight cluster, consistent with a background signal dominated by continuous extraterrestrial dust input ("cosmic rain") mixed with terrestrial material. This interpretation is consistent with the persistence of PGE-bearing nanoparticles across all stratigraphic intervals and their moderate enrichment relative to crustal compositions. The best way to differentiate the two is with the large peaks in mass concentrations at 5.2 m in sample GR-101, as shown in Figures 21 and 26.

In contrast, the YDB nanoparticle peak is distinct. It is shifted upward in Ir/Fe relative to the background cluster and overlaps fields associated with metal-rich extraterrestrial components, including iron meteorites and refractory metal-rich phases. Similar behavior is observed in independent ratio-ratio diagrams, where the inferred YDB component falls within or near iron meteorite fields and is compositionally distinct from the Greenland background population.

Importantly, the YDB point does not fall within any single reservoir field. Instead, it occupies a region consistent with a heterogeneous mixture of components, including (i) a refractory PGE-rich phase contributing elevated Ir and (ii) a more

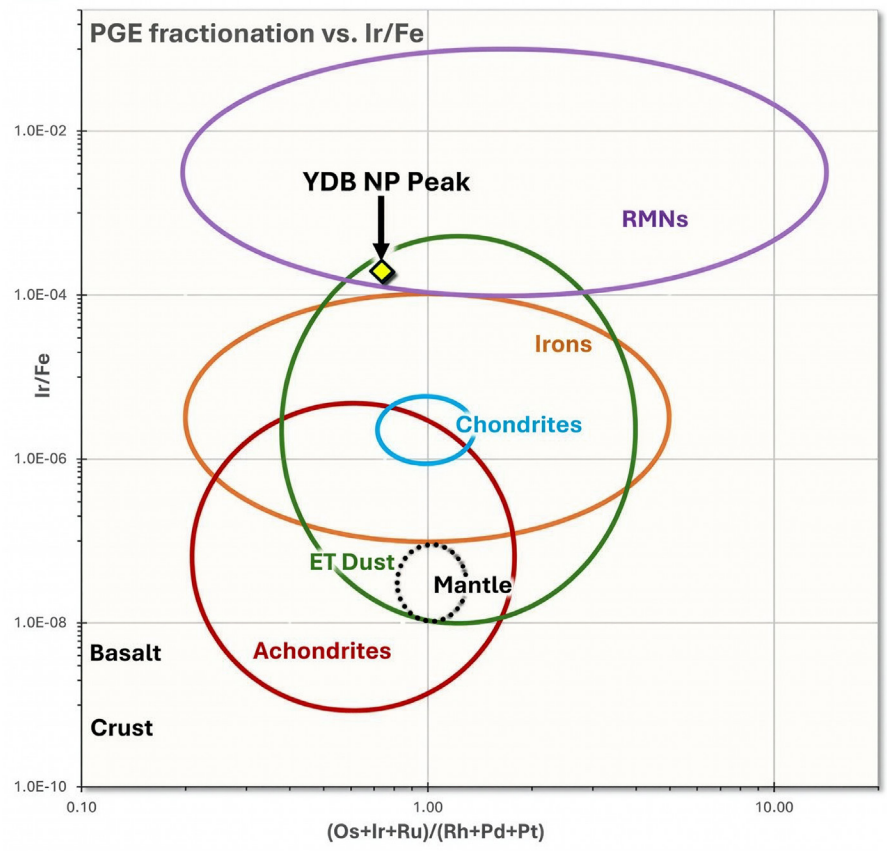


Figure 26: PGE fractionation versus Ir/Fe for Greenland nanoparticles compared with terrestrial and extraterrestrial compositional fields. The x-axis shows the ratio (Os+Ir+Ru)/(Rh+Pd+Pt), reflecting relative enrichment of refractory versus more volatile PGEs, and the y-axis shows Ir/Fe. Both axes are on logarithmic scales. Colored fields represent literature-derived compositional envelopes for chondrites, iron meteorites, achondrites, extraterrestrial dust (IDPs and micrometeorites), refractory metal nuggets (RMNs), and mantle (primitive upper mantle and cratonic mantle). Labels mark the approximate locations of values for the upper continental crust and basaltic melts. Yellow diamond marks the Younger Dryas Boundary (YDB) nanoparticle peak. The Greenland dataset forms a coherent cluster characterized by sub-chondritic PGE ratios and elevated Ir/Fe values relative to terrestrial reservoirs. The YDB peak lies above the background cluster in Ir/Fe and overlaps fields associated with metal-rich and highly fractionated extraterrestrial components, while remaining distinct from crustal, basaltic, and mantle compositions. Note that these fields are based on published third-party data but represent only approximate ranges for mixed particle populations. They are not intended to define strict compositional boundaries. Selected sources: Anders & Grevesse [141], Lodders [131], McDonough & Sun [142], Becker et al. [143], Peucker-Ehrenbrink & Jahn [129], Walker [144], Walker et al. [145], and Horan et al. [146].

volatile PGE-rich phase that lowers the overall (Os+Ir+Ru)/(Rh+Pd+Pt) ratio. This combination is most consistent with condensation from a high-temperature plume, in which PGEs partition into multiple phases with distinct transport and deposition behaviors.

Cumulatively, the data indicate that the Greenland nanoparticle population records two superimposed signals: a persistent background flux of extraterrestrial dust and a transient, compositionally distinct enrichment at the YDB. The magnitude, composition, and stratigraphic position of the YDB peak are consistent with a short-lived injection of siderophile-rich material into the atmosphere, followed by condensation, transport, and deposition of PGE-bearing nanoparticles. This interpretation is consistent with high-temperature processes associated with an airburst or impact event, although the data do not uniquely constrain the specific nature of the impactor.

Hydrocode modeling of a comet impact into Greenland ice sheet

The suite of YDB proxies found in the Greenland Ice Sheet may have resulted from an impact on the ice sheet, but this is not required; they may have been delivered from distal airbursts/impacts or through climate change. Nevertheless, to evaluate whether a high-energy impact into the Greenland Ice Sheet could account for the suite of high-temperature proxies in the YDB layer at Kangerlussuaq, we conducted numerical modeling of a hypothetical 1-km-diameter comet colliding with a 2-km-thick ice sheet. This approach builds upon validated hydrocode methodologies commonly used in planetary impact studies and terrestrial analogs [147–149]. Our intention is to assess whether such an impact could generate pressure-temperature regimes sufficient to account for

the observed formation of shocked quartz, nanodiamonds, vesicular meltglass, amorphous silica, and other high-energy materials in the YDB layer.

We employed a two-step modeling protocol. First, we used the Earth Impact Effects Program (EIEP) [150, 151] to derive first-order estimates of transient crater dimensions, shock pressures, thermal radiation, and ejecta dispersal patterns based on defined input parameters. These parameters included an impactor diameter of 1 km and an initial bulk density of 0.5 g cm^{-3}, representative of a porous cometary nucleus, an impact velocity of 30 km s^{-1}, and a 45° incidence angle, considered statistically the most probable angle for planetary impacts [152]. Atmospheric entry and aerodynamic disruption were explicitly accounted for in the model, resulting in partial fragmentation and lateral spreading of the impactor before surface contact. As a consequence, the effective impact density at the surface was reduced to ~0.25 g cm^{-3}, and the impactor diameter increased to ~1.27 km at the point of impact. The impact location was modeled as a 2-km-thick ice sheet overlying crystalline basement rock. EIEP modeling parameters are detailed in SI, Text S1.

These EIEP outputs were used to initialize a second-stage hydrocode simulation using Autodyn-2D, a well-established Eulerian finite-difference code developed by Ansys Inc. and widely employed in impact physics [153, 154]. The code allows for material heterogeneity, fragmentation, and phase transitions under shock-loading conditions. Ice was modeled using the Tillotson equation of state for water ice, calibrated for high-velocity impacts, and the comet was treated as a porous, low-strength ice-rock mixture. The selection of equations of state and constitutive models follows standard practice in hypervelocity impact modeling and is consistent with prior peer-reviewed studies of impacts into ice and ice-covered targets [155–158].

Energy partitioning into kinetic, internal, and vaporization modes was tracked throughout the simulation. The model images are visual representations of materials composited with the internal energy component, which refers to the total energy stored within a material, excluding kinetic and gravitational components. Reported temperatures, therefore, reflect localized, transient shock states rather than equilibrium or bulk melt temperatures, and are used to evaluate exceedance of known melting, vaporization, and shock-metamorphic thresholds. Autodyn modeling parameters are detailed in SI, Text S2.

The hydrocode results shown in Figure 27 represent a single non-unique realization of a comet-ice impact among many physically plausible configurations; they are not intended as an exact reconstruction of a YDB impact event. Impact outcomes are highly sensitive to parameters such as impact angle, velocity, impactor density and internal structure, fragmentation behavior, and ice thickness. Varying these inputs would yield different quantitative results while preserving the qualitative pressure-temperature regime illustrated here. Accordingly, this modeling should be interpreted as a feasibility test demonstrating physical plausibility, rather than as a best-fit or preferred solution.

Video of a hydrocode simulation of a comet impact into an ice sheet

Video available at https://player.vimeo.com/video/1101075566?app_id=122963.

Interpretation. The modeled impact parameters produce a transient cavity in the ice approximately 2.5 km wide and ~1 km deep (Figure 27). Despite the high impact energy, the underlying bedrock is not excavated; instead, it undergoes transient shock-related fracturing and deformation, including temporary vertical displacement exceeding ~600 m beneath the impact site. Shockwave propagation fractures the ice sheet radially to distances greater than 15 km, consistent with large-scale mechanical disruption. Modeled peak shock temperatures, derived from internal energy, locally exceed 10,000 K, well above the vaporization thresholds of ice and silicate materials. However, these values represent short-duration shock states rather than equilibrium temperatures. Rapid vaporization of the impactor and surrounding ice generates a steam-rich plume rising more than 3 km into the atmosphere. At the same time, debris, including molten silica, shocked quartz grains, and cometary fragments, is lofted and dispersed laterally over distances exceeding 15 km, consistent with airborne deposition of impact-related proxies.

Crucially, the modeled pressure-temperature conditions overlap those required for the production of the key proxies observed in the YDB layer: (1) shocked quartz (either entrained as detritus in the ice sheet or delivered as proximal/distal ejecta), which requires peak pressures >5 GPa and microsecond-scale dynamic loading; (2) nanodiamond polymorphs such as lonsdaleite and cubic diamond, derived from carbonaceous material exposed to extreme pressures and temperatures during shock compression; and (3) vesicular meltglass containing relict mineral inclusions, consistent with partial melting followed by rapid quenching. The modeled ejecta velocity field is also compatible with the observed lateral distribution of particles and their incorporation into overlying ice strata.

Hydrocode modeling of a cometary impact onto a thick ice sheet therefore supports the physical plausibility of generating shocked quartz, melt products, and widespread nanoparticle dispersal without forming a preserved bedrock crater. This outcome is consistent with modeling of the much larger impact that formed the Hiawatha crater beneath >1.5 km of ice in northern Greenland, which similarly predicts limited rocky ejecta despite extreme energy release [158]. In such scenarios, large volumes of ice melt and entrain terrestrial dust, which, if exposed to transient high pressures and temperatures and mixed with

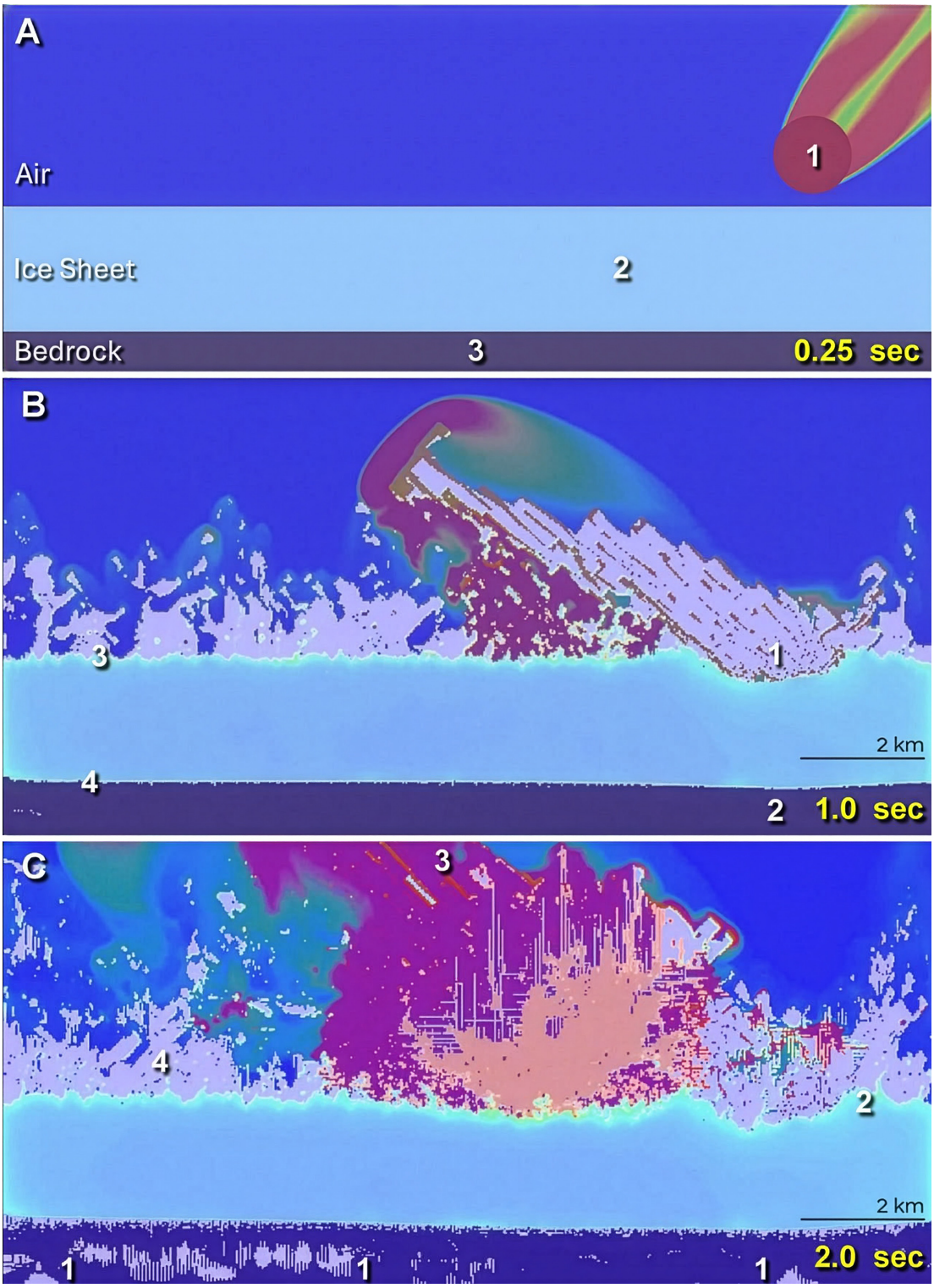


Figure 27: Hydrocode simulation of a comet impact into an ice sheet. (A) 0.25 s: A 1-km-scale comet impacts a ~2 km thick ice sheet at 45° and 30 km s^{-1}. Color contours represent shock-derived internal energy, expressed as an equivalent temperature (not actual temperature), with red indicating the highest transient values. (B) 1.0 s: Formation of an elongated transient cavity (~2.5 × 1 km) within the ice, without excavation of underlying bedrock. Shock waves propagate through the ice and into the substrate, producing transient fracturing and deformation over lateral distances exceeding ~15 km. (C) 2.0 s: The continued propagation and release of shock energy result in temporary vertical displacement of the substrate and ice surface, while impact-generated vapor and fragmented material are lofted several kilometers above the surface and dispersed laterally across the impact zone.

extraterrestrial material, can contribute to the formation of shocked quartz, PGE-bearing nanoparticles, nanodiamonds, and related proxies.

Within this framework, the absence of an identified YDB bedrock crater in Greenland is consistent with an ice-sheet impact scenario. Taken together, these results indicate that impacts into thick ice sheets can reproduce many proxy signatures commonly associated with impacts into terrestrial rock and represent a viable mechanism for delivering impact-related materials to polar ice archives. While the proxy assemblage is temporally related to the onset of Younger Dryas cooling, this study does not claim that such an event was the sole or primary trigger of the stadial; instead, it evaluates whether the Greenland ice record preserves material consistent with a short-duration, high-energy process coincident with that transition.

Hydrocode modeling represents one possible impact-on-ice configuration and does not preclude alternative scenarios involving airbursts or impacts into marine or terrestrial environments. At a broader scale, evidence from multiple YDB sites worldwide is consistent with models proposing multiple impactors derived from a fragmented extraterrestrial object, although the present study does not attempt to resolve the number, distribution, or relative importance of such events.

Numerical scope and limitations. As with all hydrocode simulations, the results presented here are limited by assumptions of material homogeneity, equation-of-state formulations, numerical resolution, and dimensionality, and are therefore intended to evaluate the physical plausibility and order-of-magnitude pressure-temperature regimes of a comet-ice impact rather than to provide a unique, high-fidelity reconstruction of a specific historical event.

Summary of Greenland ice sheet findings

To synthesize the multidisciplinary results of this study, Figures 28 and 29 below summarize the primary Younger Dryas Boundary (YDB) impact-related proxies preserved in the Greenland Ice Sheet, along with supporting information from oxygen-isotopic records and hydrocode modeling. For each proxy, we list the analytical methods employed and the principal observations that are consistent with formation under high-energy conditions. Taken together, these proxies define a stratigraphically coherent, multi-proxy signal composed of both climate-driven and event-driven components. The nanoparticle record, in particular, indicates a multi-phase atmospheric process involving (1) an abrupt increase in background dust flux driven by climatic deterioration, (2) injection of high-temperature

Proxy Type	Analytical Method	Key Finding
Dark YDB Dust Layer	Visual Stratigraphy, Dust Geochemistry	Distinct, dust-rich YD interval underlain and overlain by clear ice; changes in elemental geochemistry and ratios beginning at YD onset.
$\delta^{18}O$ Profile for Ice Sequence	Stable Isotope Mass Spectrometry	The onset of Younger Dryas cooling appears temporally associated with peak impact proxy abundances at ~5.0 m.
Nanodiamonds	TEM, SAED, SEM	Sharp abundance peak of cubic, lonsdaleite, and i-carbon types; morphologies consistent with vapor condensation.
Shocked Quartz	Optical Microscopy, TEM, EBSD	Planar deformation features (PDFs) consistent with shock metamorphism during a high-energy impact.
Meltglass and Glass-filled Lithic Aggregates	SEM, Optical Microscopy	Glassy fragments with high-temperature mineral inclusions; lithic aggregates suggest mechanical/thermal disruption.
Fe- and Si-rich Spherules	SEM-EDS, SP-ICP-TOF-MS	Abundant iron- and silica-rich microspherules consistent with melting and quenching in an impact plume.
Carbon Spherules	SEM, Optical Microscopy	Rounded, carbon-rich spheres found in peak layer; consistent with biomass combustion or carbon condensation.
Glass-like Carbon	SEM, TEM	Amorphous carbonaceous material with tektite-like textures; consistent with formation under oxygen-deficient high-T conditions.
Charcoal and Soot	Light Microscopy, Stratigraphic Correlation	Elevated concentrations coeval with impact proxies; consistent with extensive biomass burning outside Greenland.
PGEs, Ni, Co	SP-ICP-TOF-MS	Distinct peak in PGEs, Ni, and Co nanoparticles at ~5.5 m; alloyed and multi-element forms resemble impact ejecta.
Hydrocode Modeling	ANSYS Autodyn	Modeled comet impact into ice sheet generates temperatures and pressures consistent with observed suite of impact proxies.

Figure 28: Key cosmic impact proxies identified in the Younger Dryas Boundary layer at the edge of the Greenland Ice Sheet near Kangerlussuaq, Greenland. For each proxy, this Figure-table lists the analytical method(s) used with key findings. Collectively, these data document mineralogical, geochemical, and structural features that are consistent with a short-duration, high-energy event coincident with the onset of the Younger Dryas (~12.8 ka).

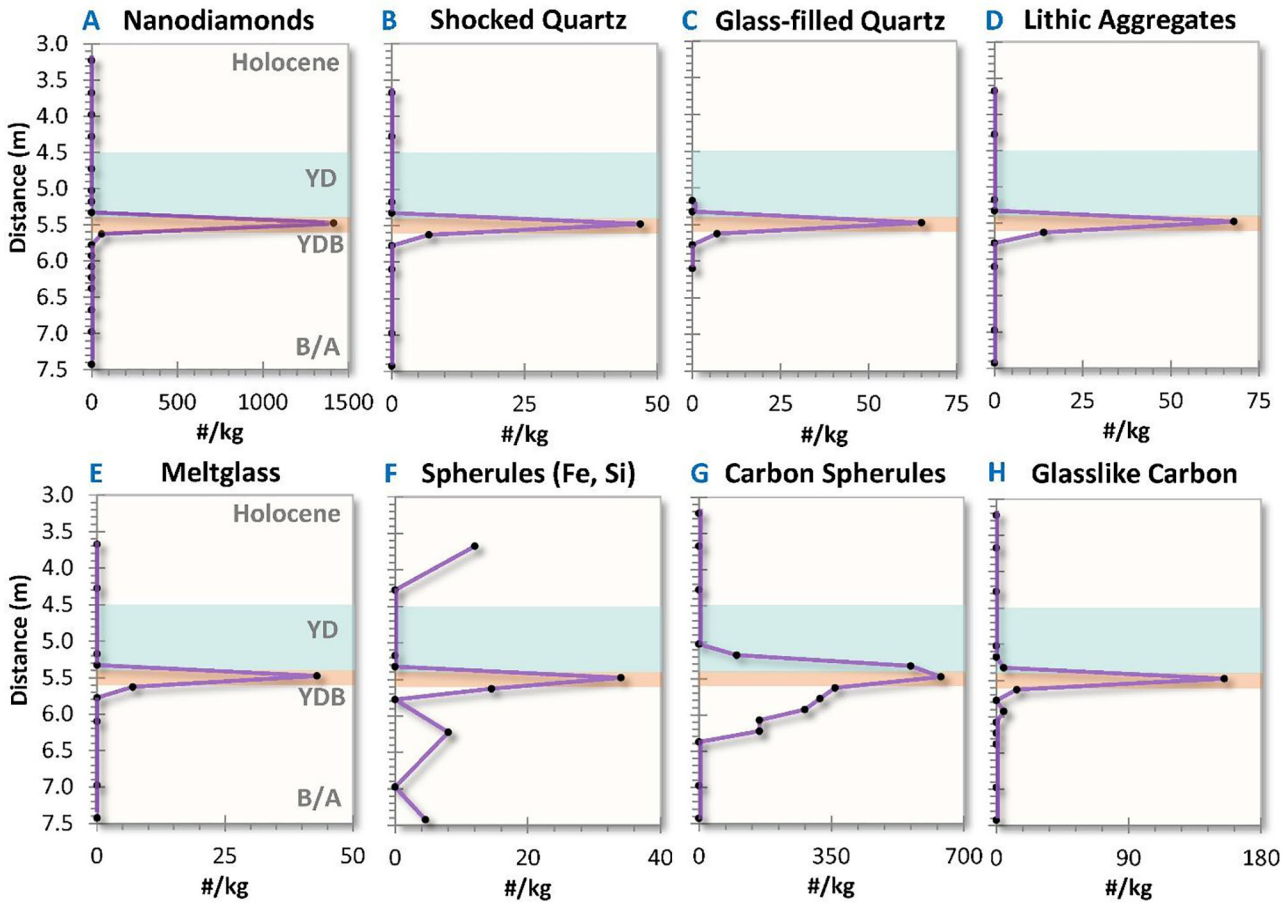


Figure 29: Distributions of the YD dust layer (A) and key impact-related proxies measured across the YDB in the Greenland Ice Sheet near Kangerlussuaq (B-J). Panels show the concentrations or abundances of (A) nanodiamonds, (B) shocked quartz, (C) glass-filled quartz, (D) lithic aggregates, (E) meltglass, (F) Fe- and Si-rich spherules, (G) carbon spherules, and (H) glass-like carbon. The shaded blue band marks the YDB interval, which coincides with a pronounced, stratigraphically confined enrichment across multiple independent proxy classes. The coherence, sharp onset, and short vertical extent of these peaks are consistent with deposition during a brief, high-energy episode; they contrast with background glacial and Holocene intervals. While individual proxies may derive from multiple formation pathways, their co-occurrence and synchronicity at the YDB are consistent with interpreting the YDB as a single, short-duration event rather than a prolonged or gradual process.

material forming a transient plume-derived nanoparticle population, and (3) subsequent condensation and delayed settling of finer particles. This combination is consistent with a short-duration, high-energy atmospheric disturbance superimposed on the broader Younger Dryas climate transition. This concise overview highlights the dataset's internal consistency and compatibility with known high-temperature and high-pressure processes associated with cosmic impacts or airbursts, while not excluding alternative mechanisms where applicable.

Limitations and uncertainties

The Greenland ice-margin setting provides a unique archive of atmospheric deposition across the Younger Dryas transition, but several factors introduce uncertainty into interpretation of the proxy record.

First, sampling at the ice margin is inherently subject to potential contamination. During fieldwork, meltwater flowed across the ice collection surface, and material entrained in upslope runoff could have been transported across the sampling area. Fracture networks within the ice also allow meltwater to infiltrate and refreeze, potentially introducing or redistributing particulate material from upslope sources. These processes may locally concentrate or dilute nanoparticles and macro-particles, analogous to lag deposits, and could partially blur the original depositional signal.

Second, the sampling strategy spanned multiple expeditions between 2008 and 2014 along a retreating ice margin. Because the ice sheet at Kangerlussuaq is actively ablating, with retreat rates across Greenland ranging from meters to approximately one kilometer per year, different field seasons sampled ice that had shifted relative to the original exposure. Although datasets were aligned using internal stratigraphic markers, including $\delta^{18}O$ and dust geochemistry, this introduces positional uncertainty and limits precise distance correlation, estimated at <5 cm.

Third, the ice-margin sequence represents a compressed and dynamically modified equivalent of central Greenland stratigraphy. Whereas the Younger Dryas interval spans tens of meters in inland ice cores, such as GISP2, it is reduced to approximately one meter at Kangerlussuaq, due to deformation during ice flow. As a result, the stratigraphic record integrates material over broader temporal intervals and may obscure fine-scale depositional structure.

Fourth, interpretation of the nanoparticle dataset carries inherent analytical and statistical uncertainties. Nanoparticles represent a very small fraction of total sample mass, and abundances are inferred from particle counts rather than bulk concentrations. The dataset is therefore sensitive to counting statistics, detection limits, particle-size-dependent transport efficiency, and instrumental calibration. Stochastic variability between adjacent samples can produce apparent fluctuations that do not necessarily reflect bulk compositional changes. Although large particle counts provide strong overall statistical power, individual ratios and peaks should be interpreted as population-level trends rather than precise concentrations.

Fifth, geochemical interpretation is complicated by variability in background dust composition. The insoluble fraction in Greenland ice reflects changing contributions from multiple source regions, and any extraterrestrial component is superimposed on this variable lithogenic background. As a result, geochemical anomalies are expressed as boundary-adjacent intervals rather than single-sample spikes.

Sixth, continuous background influx of extraterrestrial dust provides a persistent non-terrestrial component independent of any discrete event. Micrometeorites, interplanetary dust particles, and associated refractory phases contribute to baseline PGE and siderophile abundances. Distinguishing an event-related signal in an ice matrix therefore depends on stratigraphic clustering, relative enrichment, and multiproxy co-occurrence rather than absolute concentrations.

Seventh, the absence of a single-sample, uniquely diagnostic nanoparticle spike at the Younger Dryas Boundary may appear counterintuitive. However, this observation does not exclude an extraterrestrial component. Highly siderophile elements can be distributed across an interval and fractionated during atmospheric transport, condensation, and post-depositional processes, such that the record reflects a geochemically complex interval rather than a discrete layer. This interpretation is supported by the 21-year deposition of platinum independently observed in the GISP2 ice core.

Eighth, PGE fractionation during high-temperature processes, atmospheric transport, and condensation introduces additional uncertainty in source interpretation. Partitioning among vapor, melt, and particulate phases depends on temperature, oxidation state, and cooling history, and ratios such as (Os+Ir+Ru)/(Rh+Pd+Pt) and Ir/Fe may reflect secondary fractionation rather than primary source composition. This limits the ability to uniquely identify a specific impactor type from PGE systematics alone.

Ninth, interpretation of elemental ratios requires caution. Moderately siderophile elements such as Ni and Co may have significant terrestrial contributions, whereas refractory highly siderophile elements (e.g., Os, Ir, Ru, Rh) provide more robust constraints but remain subject to fractionation. No single ratio or proxy is definitive in isolation.

Tenth, identification of several key proxy classes remains uncertain. Nanocarbon particles interpreted as nanodiamonds, shock-related planar features in quartz, and certain high-temperature melt products may be mimicked by non-impact processes or require additional crystallographic confirmation. Interpretations therefore rely on the combined presence of multiple proxy types rather than any single indicator.

Eleventh, the temporal resolution of the ice-margin sequence limits interpretation of event duration and structure. Each sample integrates deposition over multi-decadal to centennial timescales, and compressed stratigraphy further reduces resolution relative to central ice cores. Short-lived depositional pulses may therefore be averaged within individual samples, obscuring finer-scale variability.

Despite these limitations, several features of the Greenland record are robust at the scale resolved by the data. Multiple independent proxies, including nanocarbon particles, shocked quartz, melt products, spherules, and PGE-bearing nanoparticles, co-occur within a narrowly defined stratigraphic interval at the onset of the Younger Dryas. While individual proxies remain subject to uncertainty and non-unique interpretation, their stratigraphic convergence, combined with coherent geochemical and nanoparticle-scale patterns, supports interpretation of a real and unusual depositional episode rather than analytical artifact or background variability. Accordingly, the evidence is most compelling when evaluated within this integrated multiproxy framework rather than as isolated observations.

Discussion

The ice-margin sequence at Kangerlussuaq preserves a sharply defined, dark, dust-filled boundary ice layer marking the onset of the Younger Dryas (YD) at ~12,800 cal BP. This boundary is characterized by a shift in $\delta^{18}O$ values and a concentrated suite of high-temperature and high-pressure proxies, including enrichments in platinum-group elements (Ir, Pt, Os) and associated siderophiles (Ni, Co), multiple carbon allotropes, shocked quartz with planar deformation features (PDFs), meltglass and glass-filled lithic aggregates, Fe- and Si-rich microspherules, carbon spherules, glasslike carbon, soot, charcoal, and a dark, dust-rich post-boundary interval. The direct deposition of these materials onto an ice-sheet surface minimizes sedimentary reworking and strengthens stratigraphic interpretation.

Because stratigraphic compression, localized deformation, and heterogeneous snow accumulation can influence

layer continuity at ice margins, interpretations focus on stratigraphic patterns rather than on the assumption of perfectly undisturbed layering. No individual proxy is interpreted as diagnostic in isolation; instead, interpretation rests on the co-occurrence of independent indicators within a stratigraphically confined interval.

Nanoparticle measurements provide an additional level of resolution that complements these bulk and micro-scale proxies. The nanoparticle-derived climate signal closely parallels the bulk ICP-MS results, demonstrating that particle-resolved measurements reproduce the same large-scale geochemical shift while additionally resolving superimposed high-temperature components that are muted or averaged in bulk analyses. Elemental ratios in the nanoparticle dataset were normalized primarily to Si, rather than the more conventional Al, because Si constitutes ~46% of total nanoparticle mass and yields lower-variance stratigraphic profiles; however, equivalent patterns are obtained using Al or Fe normalization, indicating that the observed enrichments are independent of denominator choice.

Across all 45 elements measured by SP-ICP-TOF-MS, nanoparticle ratio profiles consistently fall into one of three categories: (1) a broad, sustained enrichment reflecting climate change-driven dust flux; (2) a sharp, high-amplitude peak centered immediately above the boundary, consistent with a high-temperature plume-derived nanoparticle population; and (3) intermediate or offset enrichments consistent with a lower-temperature or more dispersed plume component. This internally consistent behavior across the full elemental dataset indicates that the observed patterns reflect distinct particle populations and formation pathways rather than element-specific effects.

Chronological control and proxy uncertainties at an ice-margin exposure

Interpretation of event timing at an ice-margin exposure relies primarily on two stratigraphic markers: (a) an abrupt $\delta^{18}O$ shift that identifies the onset of Younger Dryas cooling, and (b) a visually prominent dust-rich layer that enables field alignment among sampling seasons. Both markers are robust at the scale of the major Younger Dryas transition, but each carries site-specific uncertainties inherent to ice-margin settings. Such exposures commonly occur on sloping ablation surfaces, where lateral ice transport, compression, localized deformation, and heterogeneous accumulation histories can distort stratigraphic thickness. These factors can complicate the direct interpretation of observed distances as accurate vertical deposition rates. Accordingly, $\delta^{18}O$ and dust stratigraphy were used to locate the Younger Dryas onset horizon and to align samples stratigraphically, while recognizing that fine-scale fluctuations within the interval may not represent true climate variability.

For $\delta^{18}O$, the key chronological signal is the directional shift toward more negative values across the inferred Younger Dryas onset, which parallels reference ice-core records and supports the correlation of the dust-rich unit with Greenland Stadial 1. However, brief returns toward less-negative $\delta^{18}O$ values within the mid-Younger Dryas interval are interpreted as artifacts rather than climatic reversals. Such excursions can arise from post-depositional modification at ice margins, including localized meltwater infiltration and refreezing along cracks, isotopic diffusion or fractionation, and the effects of initial deposition at lower elevation followed by lateral transport toward the margin. The dust layer, while a valuable stratigraphic marker for correlating samples across field seasons, may also exhibit variable apparent thickness and internal structure due to ablation, surface relief, and deformation; it is therefore treated as a positional marker rather than as a precise measure of event duration.

These uncertainties primarily affect inferences about duration and synchronicity. Apparent thickness of the dust-rich interval and spacing of features along an ablation slope may not scale linearly with elapsed time, such that event duration inferred from thickness or slope distance should be regarded as approximate. Similarly, post-depositional processes may introduce minor offsets among $\delta^{18}O$ features, dust intensity, and individual proxy peaks at centimeter-to-decimeter scales. As a result, the strongest chronological conclusion supported by an ice-margin exposure is that the multi-proxy peak occurs within the stratigraphic interval that brackets the Younger Dryas onset transition, rather than that all features are exactly synchronous at sub-annual to decadal resolution. These caveats do not weaken the interpretation of a sharply defined boundary layer at the onset of Younger Dryas cooling; instead, they reflect the appropriate level of temporal precision that ice-margin stratigraphy can support.

The Younger Dryas attribution of the dust-rich interval at this exposure is not based solely on elevated dust concentrations, which characterize multiple stadials in Greenland ice-core records, but on the co-occurrence of several independent stratigraphic features. These include the magnitude and direction of the $\delta^{18}O$ shift into a prolonged cold interval, the position of the dust-rich layer within that shift, and the presence of a distinctive suite of high-temperature particulate and geochemical proxies confined to the same stratigraphic horizon. No other stadial in Greenland ice cores is known to exhibit this specific combination of proxy signatures. While absolute dating is unavailable at the ice margin, the integrated proxy assemblage provides a constrained correlation with Greenland Stadial 1 rather than with earlier stadials. A related issue concerns the pronounced thinning of the Younger Dryas interval at the ice margin relative to interior Greenland cores and its implications for temporal resolution.

Ice-margin thinning and implications for temporal resolution

The markedly reduced thickness of the Younger Dryas interval at the ice margin relative to central Greenland cores reflects expected ice-dynamical effects, including lateral flow, compression, and ablation, rather than a simple

reduction in deposition rate. Such thinning implies that the stratigraphic interval corresponding to the Younger Dryas may represent a temporally compressed record, potentially integrating deposition over longer time spans than in interior ice cores. Consequently, the nanodiamond- and spherule-bearing layer documented here should not be interpreted as resolving event duration at annual or decadal scales. Instead, its significance lies in confining impact-related proxies to the stratigraphic interval correlated with the Younger Dryas onset, rather than in the layer's thickness. A related issue concerns the origin and transport of sand-sized quartz grains exhibiting shock features within an ice-margin setting.

Origin and transport of coarse quartz grains

To our knowledge, there are no published peer-reviewed reports of millimeter-scale quartz grains preserved within Younger Dryas ice cores from any ice sheet. Particle studies of high-resolution Greenland and Antarctic ice cores document fine dust and volcanic glass shards but not coarse, sand- or pebble-sized quartz inclusions (e.g., Ruth et al. [159]). Consistent with this broader ice-core literature, we did not observe mm-sized detrital quartz grains in the Kangerlussuaq ice samples outside of the YDB layer, which also contains large-diameter meltglass and spherules.

Several quartz grains exhibiting interpreted shock features are sand-sized (0.3–1 mm), exceeding the grain sizes typically transported as background atmospheric dust and making long-range aeolian suspension unlikely. However, the presence of sand-sized mineral clasts within ice-margin exposures does not require atmospheric dust transport. Ice sheets commonly entrain sand- and gravel-sized debris at their beds and margins, and such material can be transported both englacially and supraglacially, later exposed or concentrated in ablation zones. Local aeolian processes, including short-range saltation from nearby ice-free or seasonally exposed sediment surfaces, can also deliver sand-sized grains to ice surfaces over limited distances.

Alternatively, these large grains may represent locally available detrital quartz present on or within near-surface ice that was subsequently modified by an impact- or airburst-related shock wave. The absence of similar grains outside the YDB layer does not imply that such detrital material was absent from the ice system before the event. Coarse debris in ice is typically distributed heterogeneously, occurring in localized debris-rich lenses, basal or marginal zones, or cryoconite-rich horizons that may remain cryptic until mobilized or concentrated by a transient disturbance. A high-energy impact or airburst into or near an ice margin could mechanically liberate, thermally modify, and rapidly concentrate such material into a thin surface or near-surface layer, producing a discrete stratigraphic horizon.

At the same time, large hypervelocity impacts are known to eject target material over a broad spectrum of velocities, including a high-energy fraction entrained within expanding vapor plumes rather than following simple ballistic trajectories [160]. Observational evidence from the global K-Pg boundary layer confirms the presence of impact meltglass, spherules, and shocked minerals, including quartz, at sites many thousands of kilometers from Chicxulub; planar deformation features in quartz grains have been documented in distal boundary clays in Europe, the Pacific, and other regions, consistent with ejection and long-distance transport of shock-metamorphosed material from the Chicxulub impact [161–163]. Distal ejecta layers often exhibit systematic decreases in maximum and mean grain sizes with increasing distance from the source crater, consistent with selective transport and atmospheric sorting controlled by ejection velocity and atmospheric residence times [164–166]. Tektite and microtektite strewn fields likewise indicate that mm- to cm-scale molten droplets and rock fragments can be distributed over hemispheric to near-global scales following large impacts (e.g., Australasian and other tektite fields [167–170]). Importantly, relict shocked mineral fragments, including shocked quartz, have been reported within microtektites derived from target rocks subjected to extreme shock conditions (e.g., Glass & Wu [171]; Folco et al. [172]).

The combined evidence from ejecta modeling, global impact horizons, and tektite distributions establishes the physical plausibility of long-range dispersal under exceptional impact conditions. In the Greenland case, the key observation is that shocked quartz grains are confined to the YDB layer and co-occur with micro-scale meltglass and spherules, an association not readily explained by routine ice-margin sedimentary processes alone. This co-occurrence is consistent with an event-related origin, whether through *in situ* shock modification of locally available detrital grains, incorporation of impact-derived ejecta, or a combination of both mechanisms.

Interpretation of high-temperature and shock-related proxy assemblage

The PGE data indicate a coherent, multi-element siderophile enrichment at the YDB, and ratio systematics show that this signal cannot be explained solely by background atmospheric dust. Instead, the data are consistent with the addition of a compositionally distinct, non-crustal component. Many of the observed materials are most consistent with formation under extreme physical conditions not characteristic of known terrestrial surface processes. Nanodiamonds display rounded morphologies compatible with vapor-phase condensation. Meltglass contains mineral inclusions that indicate temperatures exceeding ~2,200 °C, significantly above those produced by wildfires. Shocked quartz grains exhibit planar deformation features (PDFs) and planar fractures (PFs) that are identified using optical microscopy, TEM, and EBSD; these features are widely regarded as diagnostic of hypervelocity impact processes when confirmed by crystallographic criteria. Although some natural carbonaceous particles or tectonically deformed quartz can display partial

overlap in texture or chemistry, the combined presence of features interpreted as PFs and PDFs, oxygen-deficient amorphous silica, and melt textures is consistent with an interpretation involving extreme, short-duration pressures and temperatures.

Patterns in the Kangerlussuaq sequence closely resemble those reported from more than 50 YDB sites across at least four continents, including Abu Hureyra (Syria), Lommel (Belgium), Pilauco (Chile), and multiple localities in North America, all of which contain synchronous peaks in PGEs, nanodiamonds, shocked quartz, microspherules, meltglass, and charcoal. While precise global synchronicity cannot be fully established without additional radiometrically constrained records, the recurrence of these independent proxies in stratigraphically coeval layers is consistent with the interpretation of a large-scale, possibly hemispheric phenomenon.

Accumulating evidence suggests that the YDB event coincided with a rapid increase in atmospheric dust and soot from both terrestrial and extraterrestrial sources, potentially contributing to short-term radiative forcing or an "impact winter" at the onset of Younger Dryas cooling [16, 30, 45, 46, 97]. Analog studies provide useful context: the ~72 ka Toba eruption generated prolonged cooling detectable in Greenland ice cores [83], and recent analyses indicate that fine silicate dust from the Chicxulub impact may have been a primary driver of global cooling at the K-Pg boundary [173–176]. Together, these examples highlight plausible mechanisms through which the rapid injection of fine particulate material at the YDB could have influenced the climate.

Alternative terrestrial explanations for the Greenland proxy assemblage, such as volcanism, lightning, anthropogenic activity, or authigenic mineral formation, are difficult to reconcile with the observed combination of features. No volcanic tephra was observed in the examined boundary samples, and volcanic glasses typically exhibit microlites, bubble-wall shards, and chemical compositions that differ from the oxygen-deficient FeO and amorphous-silica phases documented here. Lightning can generate localized melting, but it is not known to account for the associated PGE enrichments and PDFs in quartz observed here, particularly within a stratigraphically confined multi-proxy horizon.

A recent Os-isotope and highly siderophile element (HSE) study has proposed volcanic aerosol input as an alternative explanation for Younger Dryas onset signals at several North American sites [177]. However, unradiogenic osmium is not uniquely diagnostic of volcanism, as mantle-derived volcanic aerosols and extraterrestrial materials can occupy overlapping low $^{187}Os/^{188}Os$ isotopic fields [178, 179]. In addition, the absence of strictly chondritic compositions in bulk sediments does not preclude an extraterrestrial contribution, because mixing with terrestrial material and high-temperature vapor plume fractionation processes can produce non-chondritic HSE signatures [180, 181]. More importantly, the Greenland ice-margin record differs from a volcanic-aerosol-only model because the YDB interval preserves a stratigraphically confined assemblage of particle-scale and mineralogical proxies, including shocked quartz, meltglass, spherules, nanocarbon particles, soot/charcoal, and PGE-bearing nanoparticles [17, 45, 46]. Volcanic aerosol deposition may contribute to regional trace-metal or dust signals, but it does not readily account for the co-occurrence of high-temperature, shock-related, carbonaceous, siderophile-enriched, and PGE-bearing particles within the same narrow onset interval. Thus, while volcanic forcing cannot be excluded as part of the broader Younger Dryas climate system, volcanic aerosols alone are insufficient to explain the full proxy assemblage preserved at Kangerlussuaq.

Authigenic processes lack the capacity to generate high-temperature melt products or shock features, and human activity is anachronistic for this interval. We are not aware of a volcanic, diagenetic, or anthropogenic process that has been demonstrated to generate this specific combination of microstructural (planar lamellae/PDF-like features), CL response, and oxygen-depleted amorphous silica in near-surface ice, particularly when co-occurring with the broader proxy suite in the same stratigraphically confined horizon; accordingly, the combined assemblage is most consistent with a high-energy, short-duration process.

Crater absence and implications for Younger Dryas impact scenarios

A frequent counterargument to the Younger Dryas impact hypothesis is the absence of a confirmed, contemporaneous impact crater. However, the lack of a preserved crater does not preclude an impact or airburst origin for the Younger Dryas Boundary (YDB) proxy assemblage. Many impact events are recognized primarily through laterally extensive "spherule datum layers", stratigraphically discrete horizons enriched in microtektites, microkrystites, and related high-temperature condensates, rather than through the discovery of an identifiable crater. A well-known example is the Australasian tektite strewn field (~0.79 Ma), which covers a substantial fraction of Earth's surface yet lacks an unequivocally identified source crater; its recognition instead relies on widespread tektites and microtektites that form a coherent regional-to-hemispheric spherule datum layer (e.g., Glass et al. [168]; Simonson et al. [170, 182]. Such layers are widely accepted as diagnostic indicators of hypervelocity impacts, even in the absence of preserved crater morphology.

In the case of the Younger Dryas Impact Hypothesis, several plausible impact scenarios would favor the formation of a spherule datum layer while minimizing or eliminating long-lived crater expression. Low-altitude airbursts, oblique impacts, or impacts into ice sheets or ice-covered marine surfaces are expected to disperse impact energy laterally and vertically into the atmosphere, promoting the production and wide distribution of melt droplets, vapor condensates, and fine particulate ejecta. Ice sheets, in particular, act as efficient

energy absorbers and dispersal media, inhibiting the excavation of bedrock and favoring the preservation of sharp geochemical and particulate horizons rather than durable geomorphic structures. Within this framework, the Greenland Ice Sheet represents a plausible impact surface where the primary record of such an event would be a stratigraphically discrete spherule datum layer enriched in platinum-group elements, microspherules, and other high-temperature proxies. The coherent YDB layer documented here, together with comparable spherule-bearing horizons reported from marine and terrestrial archives, is therefore consistent with a craterless impact or airburst scenario and aligns with established modes of impact recognition in the geologic record.

Analytical considerations must also be acknowledged. Although SP-ICP-TOF-MS provides uniquely high-resolution nanoparticle data, uncertainties in absolute particle mass, detection efficiency, and counting statistics should be considered when interpreting sharp stratigraphic excursions. These limitations do not diminish the observed coherence of the proxy suite but highlight the importance of integrating multiple independent lines of evidence.

Taken together, the geochemical, mineralogical, and physical indicators suggest that the Kangerlussuaq sequence records a short-duration, high-energy event coincident with the onset of the Younger Dryas. The presence of biomass-burning indicators, such as carbon spherules and glasslike carbon, is consistent with widespread wildfire and atmospheric disturbance. The proxy assemblage aligns with interpretations from numerous YDB sites worldwide that favor deposition from a cosmic impact or atmospheric airburst. While additional work is required to refine the event magnitude and mechanisms, the Greenland record provides unusually well-preserved evidence consistent with a rapid, high-energy event at the YD onset. While the proxy assemblage is temporally associated with the onset of Younger Dryas cooling, this study does not claim to resolve whether the inferred high-energy event was the sole or primary trigger of the stadial. Instead, it evaluates whether the Greenland ice record preserves material consistent with a short-duration, high-energy process coincident with that transition.

The nanoparticle dataset provides a direct bridge between bulk geochemical trends and discrete impact proxies. The consistent classification of all measured elements into three particle populations, climate-driven dust, high-temperature plume condensates, and lower-temperature plume derivatives, indicates that the Younger Dryas onset reflects a coupled system in which atmospheric circulation changes and a transient high-energy event both contributed to the observed geochemical record.

Conclusions

The ice-margin sequence at Kangerlussuaq in western Greenland preserves a dark, sharply defined, dust-rich interval correlated with the onset of the Younger Dryas (YD) at ~12,800 cal BP. This correlation is supported by visible stratigraphy, $\delta^{18}O$ trends, and dust-related geochemical changes. However, the ice-margin setting requires caution because stratigraphic compression, ablation, meltwater infiltration, heterogeneous snow accumulation, and multi-season sample alignment introduce uncertainty at fine spatial and temporal scales. For that reason, the principal interpretation does not depend on centimeter-scale synchronicity, but on stratigraphic clustering and multiproxy co-occurrence across the YD onset interval.

The first major result is that the Kangerlussuaq sequence records a sustained YD-scale change in atmospheric dust composition and provenance. Bulk ICP-MS ratios and SP-ICP-TOF-MS nanoparticle phase associations indicate a shift in mineral-dust delivery at the BA-YD transition, including increased dust loading and a change in the relative abundance of quartz-, chromite-, and zircon-associated particles compared with Fe-oxide-rich, Al-rich, and mica-amphibole-associated particles. This broader dust signal is consistent with intensified atmospheric circulation, stronger winds, greater aridity, and changing source-region contributions beginning at the onset of the YD climate interval and continuing for ~1,200–1,300 years.

The second major result is that the broader climate-driven dust signal is superimposed by a narrower proxy-rich horizon at the YDB layer. This horizon contains peak abundances of multiple macro- and nano-scale proxies, including nanocarbon particles previously interpreted as nanodiamonds, quartz grains with shocked planar microstructures, meltglass, glass-filled lithic aggregates, Fe- and Si-rich spherules, carbon-rich spherules, glasslike carbon, charcoal, soot, and PGE-associated materials. These proxy classes are not all uniquely diagnostic in isolation, and some remain debated; however, their co-occurrence within a narrow stratigraphic interval is unusual and is consistent with a short-duration, high-energy depositional episode.

The third major result is that SP-ICP-TOF-MS reveals a delayed nanoparticle maximum above the YDB layer. Predominantly terrestrial elements, including Nb, Ta, U, As, Pb, and Sb, and siderophile- and PGE-bearing nanoparticles, including Ir, Pt, Os, Pd, Ni, Co, and Re, reach peak concentrations near ~5.2 m, above the proxy-rich YDB layer at ~5.5 m. This offset is important because the YDB layer itself contains local minima for several of these nanoparticle components. The pattern indicates that nanoparticle deposition was not a single instantaneous pulse but a temporally structured, multi-phase process, likely involving initial boundary-layer deposition followed by delayed atmospheric transport, settling, scavenging, or redistribution of finer particles. The structure closely parallels the previously reported GISP2 platinum anomaly [87], which rose gradually for 14 years to a delayed peak and declined over an approximately 21-year interval at the onset of YD

cooling. Those independent authors directly linked the onset of the Pt signal to a decline in $\delta^{18}O$ values, signaling the onset of YD cooling. This correspondence is consistent with a causal link between the influx of inferred impact-related proxies and YD climate change.

The fourth major result is that the PGE-bearing nanoparticle population is compositionally distinct from normal Greenland background dust. PGE sum, Ir, Pt, Os, Pd, Ni, Co, and Re are strongly enriched at the nanoparticle peak, and ratio–ratio comparisons show that the inferred YDB component plots outside the Greenland background cluster and shifts toward extraterrestrial or metal-rich reference fields. The PGE fractionation and Ir/Fe systematics indicate that the Greenland YDB signal is not consistent with a single ET source. Its sub-chondritic (Os+Ir+Ru)/(Rh+Pd+Pt) ratio, combined with elevated Ir/Fe, is best explained by a heterogeneous, fractionated mixture comprising (i) a refractory PGE-rich component, consistent with RMN-like material, and (ii) a more volatile PGE-bearing component, consistent with fine-grained extraterrestrial dust such as IDPs or cometary material. Micrometeorite populations provide a plausible carrier for such mixed signatures, as they can incorporate both refractory condensates and volatile-enriched phases and undergo further fractionation during atmospheric entry. Bulk chondritic or iron meteorite compositions alone do not reproduce the observed combination of PGE fractionation and Ir/Fe. Accordingly, the Greenland YDB signal is most consistent with a mixed, particle-scale extraterrestrial dust population, potentially derived from cometary or meteoritic sources, rather than a single, homogeneous impactor class.

The fifth major result is that hydrocode modeling supports the physical plausibility of a high-velocity impact into an ice-sheet target as a mechanism for generating shock pressures, high temperatures, melt products, spherules, shocked quartz, and widespread nanoparticle dispersal. The model is not a unique reconstruction of the Greenland event, but it demonstrates that an ice-sheet impact or airburst-related scenario can plausibly produce the types of materials observed in the Kangerlussuaq record. The absence of a confirmed crater does not by itself preclude such a scenario, particularly if the event involved an airburst, an impact into ice, or dispersed deposition from a larger event.

The Kangerlussuaq record is best explained by a coupled depositional model involving (i) sustained climate-driven dust enrichment throughout the YD interval, (ii) a narrow YDB layer containing high-temperature, shocked, carbonaceous, and melt-related proxies, and (iii) a delayed, boundary-adjacent nanoparticle pulse enriched in crustal, siderophile, and PGE-bearing material. Volcanism, biomass burning, authigenesis, anthropogenic contamination, or ordinary terrestrial dust transport may explain individual components of the assemblage, but no single terrestrial process readily accounts for the full combination of stratigraphic, mineralogical, carbonaceous, and siderophile-enriched proxies. Conversely, no single proxy or ratio proves an impact origin. The strongest conclusion is therefore not that any individual proxy is definitive, but that the multiproxy assemblage, its narrow stratigraphic clustering, its preservation in ice with limited sedimentary reworking, its delayed nanoparticle structure, and its PGE systematics are collectively consistent with a short-duration, high-energy airburst or impact-related depositional episode at the onset of the YD.

The Greenland sequence provides an unusually well-preserved atmospheric record showing that a distinct high-energy depositional episode, potentially involving extraterrestrial material, coincided with the onset of the YD and was superimposed on the broader climatic transition into colder, dustier conditions. Further work, especially isotopic measurements of Os, Cr, or other source-sensitive systems, higher-resolution ice-core comparisons, and additional particle-scale analyses, will be required to more precisely constrain the source, magnitude, and mechanism of the event.

METHODS

Oxygen isotope analysis

Stable oxygen isotope ratios ($\delta^{18}O$) were measured at 10-cm resolution using isotope-ratio mass spectrometry (IRMS), with an analytical precision of ±0.1‰ (1σ). The resulting profile was aligned with the GISP2 and GRIP ice-core records [22, 81] to assist in identifying the Younger Dryas (YD) onset in the Kangerlussuaq sequence. Slope-distance estimates for the YD boundary are accurate to within ±0.1 m (95% CI), accounting for layer thinning, compression, and tilting near the ice margin [19].

Shock-fractured and shocked quartz grains

Thin section preparation of quartz grains was performed by Spectrum Petrographics (Vancouver, Washington, USA) following standard petrographic procedures optimized for the preservation of shock microstructures. Individual grains and grain mounts were vacuum-impregnated with low-viscosity epoxy to stabilize fragile microfractures and planar deformation features before cutting. Initial trimming and sectioning were performed using diamond saws under continuous fluid lubrication to minimize frictional heating and mechanical stress.

Grinding and polishing were carried out in progressive stages using fine-grit diamond abrasives, with careful control of applied pressure, rotation speed, and contact time. Throughout preparation, particular attention was paid to limiting temperature increases and vibrational stress to prevent the introduction of preparation-induced microfractures or spurious planar features. Final polishing was

performed under low-load conditions to achieve optical transparency while preserving the primary crystallographic shock features.

These procedures are specifically designed to ensure that observed planar deformation features, mosaicism, and related microstructures in quartz are primary and not artifacts of sample preparation.

Shocked-quartz candidate grains were first recognized under petrographic microscopy and subsequently examined using a universal stage, standardless scanning electron microscopy (SEM), high-resolution TEM (HRTEM), and electron backscatter diffraction (EBSD). Criteria for planar deformation features (PDFs) follow established protocols, with uncertainties largely governed by counting statistics and preservation of diagnostic lamellae. We estimate a ±10% uncertainty (95% CI) in identifying PDFs and shock-related microstructures.

Nanodiamonds

Previously, two studies [19, 23] extracted nanodiamonds using the standard protocol [23], described in their Appendix A [23]. Using their extracted residues, we identified additional nanodiamonds by high-resolution transmission electron microscopy (TEM), scanning TEM (STEM), and selected-area electron diffraction (SAED). Nanodiamond identification was based on characteristic lattice spacings and established morphologies of known cubic and hexagonal polytypes.

Mineralogical and structural analysis

Cathodoluminescence (CL) imaging was used as a supplementary technique to evaluate lattice damage in selected quartz grains. CL observations were made using SEM-based CL imaging under standard accelerating voltages and beam currents. Quartz containing planar deformation features (PDFs) and related lattice damage commonly exhibits reduced or quenched luminescence due to the disruption of crystal defects that act as luminescence centers. Non-luminescent (dark) domains observed under CL are therefore consistent with shock-related lattice disorder; however, non-luminescence is not unique to shock metamorphism and may also characterize low-temperature authigenic (diagenetic) quartz. Accordingly, CL observations are not interpreted as diagnostic of shock in isolation; instead, they are evaluated in conjunction with optical petrography, the crystallographic orientation of lamellae, and independent confirmation of PDFs by TEM and EBSD.

Meltglass, glass-filled lithic aggregates, Fe- and Si-rich spherules, carbon spherules, and glasslike carbon were analyzed using SEM and energy-dispersive spectroscopy (EDS), following the standard protocols of Firestone et al. [16], Bunch et al. [42], LeCompte et al. [40], and Wittke et al. [18]. Elemental and textural measurements typically show a standard deviation of <5% for major compositional components.

Single particle inductively coupled plasma time-of-flight mass spectrometry (SP-ICP-TOF-MS)

This study applies SP-ICP-TOF-MS to Greenland ice and dust samples, representing a novel use of this technique for assessing potential impact-related signatures in an ice-core context. For analysis, 100-mg aliquots of sediment were suspended in 10 mL of ultrapure water (Millipore Advantage System, Merck Millipore) in acid-washed 15-mL centrifuge tubes.

SP-ICP-TOF-MS enables the enumeration of individual nanoparticles and the simultaneous measurement of transient mass signals for selected elements in particles ranging in diameter from ~20 nm to ~2 μm. This approach provides high time-resolution elemental data at the single-particle scale, allowing characterization of particle populations that include likely Fe phases (e.g., magnetite, wüstite), Al phases (e.g., sillimanite, spinel), mixed Al-Si-Fe phases (e.g., mica, amphibole), Zr-Si phases (e.g., zircon), Cr-Fe phases (e.g., chromite, chromian magnetite), Al-Si phases (e.g., feldspars), Si phases (e.g., quartz, feldspar), and Ti-Fe phases (e.g., ilmenite). However, the technique does not directly identify specific minerals.

Nanoparticles were analyzed from three stratigraphic intervals: the Bølling-Allerød (BA; 5.63–6.68 m), the Younger Dryas (YD; 4.57–5.47 m), and the Holocene (3.82–4.42 m). Across these intervals, more than 1.2 million individual nanoparticles were quantified (averaging ~60,000 per sample across 20 samples). The resulting elemental distributions were used to evaluate changes in dust provenance, atmospheric circulation, and compositional shifts associated with the Younger Dryas onset.

Nanoparticle quality assurance and detection limits. Analyses were conducted under clean laboratory conditions, with procedural and field blanks prepared using identical reagents and containers. Blank particle counts for elements central to this study (e.g., Pt, Ir, Ni, Co, Fe) were consistently at or below single-digit counts per analytical run, well below the particle abundances observed within the dust-rich YD interval. Instrument performance (mass calibration, sensitivity drift, and count-rate stability) was monitored by repeated measurement of multi-element standards and internal controls. Element-specific detection limits were derived from blank-corrected background signals and Poisson counting statistics. Particles were classified as containing a given element when transient signals exceeded background by ≥3σ. Because cross-laboratory SP-ICP-TOF-MS datasets for glacial materials are not yet available, the results presented here should be regarded as a first-order, internally consistent assessment

of nanoparticle compositional variation across the BA-YD-Holocene sequence.

Hydrocode modeling

To investigate plausible cosmic impact scenarios, we performed numerical modeling using ANSYS Autodyn to simulate a cometary impact into an ice sheet. The modeling was designed to evaluate the physical feasibility of generating extreme pressure-temperature conditions, rather than to reconstruct a unique impact event. Initial conditions included a kilometer-scale impactor traveling at ~30 km s^{-1} with an entry angle of 45°. The simulations tracked shock pressure, internal energy, and material dispersal to assess whether conditions consistent with the formation of observed proxies could be produced. Modeled peak pressures exceeded several gigapascals, and transient shock temperatures exceeded melting and vaporization thresholds for ice and silicate materials, conditions sufficient to account for the formation of nanodiamonds, shocked quartz, meltglass, and associated high-temperature particles. Because impact outcomes are highly sensitive to parameters such as impact angle, velocity, impactor structure, and target properties, the results are non-unique and represent only one of many physically plausible scenarios. Detailed descriptions of model setup, material properties, and parameter selection are provided in Supporting Information Texts S1 and S2.

Supporting information

SI. Supporting information. Additional figures, tables, and methods.
https://zenodo.org/records/19956672.

Acknowledgements

We are grateful for the hospitality and assistance of the people of Greenland and Denmark. We also appreciate the invaluable assistance of J.P. Steffenson from the Centre for Ice and Climate at the Niels Bohr Institute, University of Copenhagen, Denmark. We thank Luis Costa, Metin Ozen, and Chris Cowan of Ozen Engineering, Inc. for their assistance with Autodyn programming. We are also grateful for the assistance of Eugene Jhong and Brian Muraresku, provided through the Athanatos Foundation, which helped make this research possible. During the preparation of this manuscript, the authors used ChatGPT (GPT-4 and GPT-5, OpenAI, https://chat.openai.com) to improve grammar, clarity, and conciseness. After using this tool, the authors reviewed and edited all content to ensure accuracy and adherence to scientific standards, following the journal's ethical guidelines. We take full responsibility for the content of this publication.

Ethics statement/compliance with Greenland regulations

Fieldwork and sampling in western Greenland were carried out under the required permits issued by relevant Greenlandic and Danish authorities and in accordance with institutional and national guidelines. No Indigenous knowledge or culturally sensitive information was used without appropriate consultation or permission.

Author contributions

P.A.M., A.V.K., J.P.K., W.S.W., and A.W. conceived and directed aspects of the project. All co-authors contributed data and/or technical analysis for the paper and wrote, edited, reviewed, and/or approved the manuscript.

Funding

The study was funded mainly by the Comet Research Group (CRG) and with the generous support of Eugene Jhong and Brian Muraresku through the Athanatos Foundation, who provided substantial research gifts to the University of California, Santa Barbara (J.P.K.) and the University of South Carolina through the South Carolina Institute for Archaeology and Anthropology (C.R.M.). G.K. was funded by the Czech Science Foundation (Grant 23-06075S) and by the Ministry of Education, Youth and Sport of the Czech Republic (project No. LUAUS25082).

Data availability

All data files are available in this manuscript and the Supporting Information.

https://zenodo.org/records/19956672.

A video of the hydrocode simulation is available on Vimeo (https://player.vimeo.com/video/1101075566?app_id=122963).

Sample availability

All samples for this study have been processed, and no unprocessed material is available, except for the ice-sheet margin in Greenland.

Competing interests

J.P.K., M.A.L., C.R.M., and A.W. volunteer their time as co-founders and directors of CRG. No co-author receives a salary, compensation, stock, or any other financial benefit from CRG, except for tax deductions for

CRG donations by co-authors A.W., M.A.L., and T.W. All co-authors may receive reimbursements from their respective organizations for attending symposia on the research presented in this paper. A.W. is a co-author of a book about the Younger Dryas Impact Hypothesis; he donates all proceeds to the non-profit Comet Research Group. The authors declare no other potential competing interests.

Declaration of AI assistance in the manuscript preparation process

During the preparation of this work, the author(s) used ChatGPT (GPT-4 and GPT-5, OpenAI, https://chat.openai.com) to improve grammar, clarity, and conciseness. After using this tool/service, the authors reviewed and edited the content as needed and take full responsibility for the content of the published article.

References

1. Alley, R.B.; Meese, D.A.; Shuman, C.A.; Gow, A.J.; Taylor, K.C.; Grootes, P.M.; White, J.W.C.; Ram, M.; Waddington, E.D.; Mayewski, P.A.; Zielinski, G.A. Abrupt Increase in Greenland Snow Accumulation at the End of the Younger Dryas Event. *Nature* **1993**, *362*, 527–529, doi:10.1038/362527a0.
2. Dansgaard, W.; Johnsen, S.J.; Clausen, H.B.; Dahl-Jensen, D.; Gundestrup, N.S.; Hammer, C.U.; Hvidberg, C.S.; Steffensen, J.P.; Sveinbjörnsdottir, A.E.; Jouzel, J.; et al. Evidence for General Instability of Past Climate From a 250-kyr Ice-Core Record. *Nature* **1993**, *364*, 218–220, doi:10.1038/364218a0.
3. Bond, G.; Showers, W.; Cheseby, M.; Lotti, R.; Almasi, P.; deMenocal, P.; Priore, P.; Cullen, H.; Hajdas, I.; Bonani, G. A Pervasive Millennial-Scale Cycle in North Atlantic Holocene and Glacial Climates. *Science* **1997**, *278*, 1257–1266, doi:10.1126/science.278.5341.1257.
4. Broecker, W.S.; Andree, M.; Wolfli, W.; Oeschger, H.; Bonani, G.; Kennett, J.; Peteet, D. The Chronology of the Last Deglaciation: Implications to the Cause of the Younger Dryas Event. *Paleoceanography* **1988**, *3*, 1–19, doi:10.1029/PA003i001p00001.
5. Broecker, W.S.; Kennett, J.P.; Flower, B.P.; Teller, J.T.; Trumbore, S.; Bonani, G.; Wolfli, W. Routing of Meltwater from the Laurentide Ice Sheet During the Younger Dryas Cold Episode. *Nature* **1989**, *341*, 318–321, doi:10.1038/341318a0.
6. Broecker, W.S. Geology. Was the Younger Dryas Triggered by a Flood? *Science* **2006**, *312*, 1146–1148, doi:10.1126/science.1123253.
7. McManus, J.F.; Francois, R.; Gherardi, J.M.; Keigwin, L.D.; Brown-Leger, S. Collapse and Rapid Resumption of Atlantic Meridional Circulation Linked to Deglacial Climate Changes. *Nature* **2004**, *428*, 834–837, doi:10.1038/nature02494.
8. Bakke, J.; Lie, Ø.; Heegaard, E.; Dokken, T.; Haug, G.H.; Birks, H.H.; Dulski, P.; Nilsen, T. Rapid Oceanic and Atmospheric Changes During the Younger Dryas Cold Period. *Nat. Geosci.* **2009**, *2*, 202–205, doi:10.1038/Ngeo439.
9. Blunier, T.; Brook, E.J. Timing of Millennial-Scale Climate Change in Antarctica and Greenland During the Last Glacial Period. *Science* **2001**, *291*, 109–112, doi:10.1126/science.291.5501.109.
10. WAIS Divide Project Members. Precise Interpolar Phasing of Abrupt Climate Change During the Last Ice Age. *Nature* **2015**, *520*, 661–665, doi:10.1038/nature14401.
11. Rasmussen, S.O.; Andersen, K.K.; Svensson, A.M.; Steffensen, J.P.; Vinther, B.M.; Clausen, H.B.; Siggaard-Andersen, M.L.; Johnsen, S.J.; Larsen, L.B.; Dahl-Jensen, D.; et al. A New Greenland Ice Core Chronology for the Last Glacial Termination. *J. Geophys. Res. Atmos.* **2006**, *111*, doi:10.1029/2005JD006079.
12. Steffensen, J.P.; Andersen, K.K.; Bigler, M.; Clausen, H.B.; Dahl-Jensen, D.; Fischer, H.; Goto-Azuma, K.; Hansson, M.; Johnsen, S.J.; Jouzel, J.; et al. High-Resolution Greenland Ice Core Data Show Abrupt Climate Change Happens in Few Years. *Science* **2008**, *321*, 680–684, doi:10.1126/science.1157707.
13. Svensson, A.; Andersen, K.K.; Bigler, M.; Clausen, H.B.; Dahl-Jensen, D.; Davies, S.M.; Johnsen, S.J.; Muscheler, R.; Parrenin, F.; Rasmussen, S.O.; et al. A 60 000 Year Greenland Stratigraphic Ice Core Chronology. *Clim. Past* **2008**, *4*, 47–57, doi:10.5194/cp.4.47.2008.
14. Baldini, L.M.; McDermott, F.; Baldini, J.U.L.; Arias, P.; Cueto, M.; Fairchild, I.J.; Hoffmann, D.L.; Mattey, D.P.; Müller, W.; Nita, D.C.; et al. Regional Temperature, Atmospheric Circulation, and Sea-Ice Variability Within the Younger Dryas Event Constrained Using a Speleothem from Northern Iberia. *Earth Planet. Sci. Lett.* **2015**, *419*, 101–110, doi:10.1016/j.epsl.2015.03.015.
15. Condron, A.; Winsor, P. Meltwater Routing and the Younger Dryas. *Proc. Natl. Acad Sci. U. S. A.* **2012**, *109*, 19928–19933, doi:10.1073/pnas.1207381109.
16. Firestone, R.B.; West, A.; Kennett, J.P.; Becker, L.; Bunch, T.E.; Revay, Z.S.; Schultz, P.H.; Belgya, T.; Kennett, D.J.; Erlandson, J.M.; et al. Evidence for an Extraterrestrial Impact 12,900 Years Ago that Contributed to the Megafaunal Extinctions and the Younger Dryas Cooling. *Proc. Natl. Acad. Sci. U. S. A.* **2007**, *104*, 16016–16021, doi:10.1073/pnas.0706977104.
17. Kennett, J.P.; Kennett, D.J.; Culleton, B.J.; Aura Tortosa, J.E.; Bischoff, J.L.; Bunch, T.E.; Randolph Daniel, I., Jr.; Erlandson, J.M.; Ferraro, D.; Firestone, R.B.; et al. Bayesian Chronological Analyses Consistent with Synchronous Age of 12,835-12,735 Cal B.P. for Younger Dryas Boundary on Four Continents. *Proc. Natl. Acad. Sci. U. S. A.* **2015**, *112*, E4344–E4353, doi:10.1073/pnas.1507146112.
18. Wittke, J.H.; Weaver, J.C.; Bunch, T.E.; Kennett, J.P.; Kennett, D.J.; Moore, A.M.; Hillman, G.C.; Tankersley, K.B.; Goodyear, A.C.; Moore, C.R.; et al. Evidence for Deposition of 10 Million Tonnes of Impact Spherules Across Four Continents 12,800 y Ago. *Proc. Natl. Acad. Sci. U. S. A.* **2013**, *110*, E2088–E2097, doi:10.1073/pnas.1301760110.
19. Kurbatov, A.V.; Mayewski, P.A.; Steffensen, J.P.; West, A.; Kennett, D.J.; Kennett, J.P.; Bunch, T.E.; Handley, M.; Introne, D.S.; Que Hee, S.S.; et al. Discovery of a Nanodiamond-Rich Layer in the Greenland Ice Sheet. *J. Glaciol.* **2010**, *56*, 747–757, doi:10.3189/002214310794457191.
20. Yates, P.D.; Arden, J.W.; Wright, I.P.; Pillinger, C.T.; Hutchison, R. A Search for Pre-Solar Material Within an Acid-Resistant Residue of Greenland Cryoconite. *Meteoritics* **1992**, *27*(3), 309.
21. Dansgaard, W.; Clausen, H.B.; Gundestrup, N.; Hammer, C.U.; Johnsen, S.F.; Kristinsdottir, P.M.; Reeh, N. A New Greenland Deep Ice Core. *Science* **1982**, *218*, 1273–1277, doi:10.1126/science.218.4579.1273.
22. Stuiver, M.; Grootes, P.M. GISP2 Oxygen Isotope Ratios. *Quat. Res.* **2000**, *53*, 277–284, doi:10.1006/qres.2000.2127.
23. Kinzie, C.R.; Que Hee, S.S.; Stich, A.; Tague, K.A.; Mercer, C.; Razink, J.J.; Kennett, D.J.; DeCarli, P.S.; Bunch, T.E.; Wittke, J.H.; et al. Nanodiamond-Rich Layer Across Three Continents Consistent with Major Cosmic Impact at 12,800 cal BP. *J. Geol.* **2014**, *122*, 475–506, doi:10.1086/677046.
24. DeCarli, P.S.; Bowden, E.; Jones, A.P.; Price, G.D. Laboratory Impact Experiments Versus Natural Impact Events. *Geo. S. Am. S.* **2002**, *356*, 595–605.

25. Maruyama, K.; Makino, M.; Kikukawa, N.; Shiraishi, M. Synthesis of Hexagonal Diamond in a Hydrogen Plasma Jet. *J. Mater. Sci. Lett.* **1992**, *11*, 116–118, doi:10.1007/BF00724617.
26. Hanneman, R.E.; Strong, H.M.; Bundy, F.P. Hexagonal Diamonds in Meteorites: Implications. *Science* **1967**, *155*, 995–997, doi:10.1126/science.155.3765.995.
27. Koeberl, C.; Masaitis, V.L.; Shafranovsky, G.I.; Gilmour, I.; Langenhorst, F.; Schrauder, M. Diamonds from the Popigai Impact Structure, Russia. *Geology* **1997**, *25*, 967–970, doi:10.1130/0091.7613(1997)025[[0967:DFTPIS]]2.3.CO;2.
28. West, A.; Kennett, J.; Kennett, D.J.; Bunch, T.E.; Stafford Jr, T.W.; Wolbach, W.S. Are Nanodiamonds Evidence for a Younger Dryas Impact Event? In *AGU Fall Meeting Abstracts*; 2009; Volume 2009, PP33B–02.
29. Sweatman, M.B.; Powell, J.L.; West, A. Rebuttal of Holliday et al.'s Comprehensive Gish Gallop of the Younger Dryas Impact Hypothesis. *Airburs. Crater. Imp.* **2024**, *2*, doi:10.14293/ACI.2024.0007.
30. Sweatman, M.B. The Younger Dryas Impact Hypothesis: Review of the Impact Evidence. *Earth Sci. Rev.* **2021**, *218*, 103677, doi:10.1016/j.earscirev.2021.103677.
31. Powell, J.L. Premature Rejection in Science: The Case of the Younger Dryas Impact Hypothesis. *Sci. Prog.* **2022**, *105*, 368504211064272, doi:10.1177/00368504211064272.
32. Bement, L.C.; Madden, A.S.; Carter, B.J.; Simms, A.R.; Swindle, A.L.; Alexander, H.M.; Fine, S.; Benamara, M. Quantifying the Distribution of Nanodiamonds in Pre-Younger Dryas to Recent Age Deposits Along Bull Creek, Oklahoma Panhandle, USA. *Proc. Natl. Acad. Sci. U. S. A.* **2014**, *111*, 1726–1731, doi:10.1073/pnas.1309734111.
33. Kennett, D.J.; Kennett, J.P.; West, A.; West, G.J.; Bunch, T.E.; Culleton, B.J.; Erlandson, J.M.; Que Hee, S.S.; Johnson, J.R.; Mercer, C.; et al. Shock-Synthesized Hexagonal Diamonds in Younger Dryas Boundary Sediments. *Proc. Natl. Acad. Sci. U. S. A.* **2009**, *106*, 12623–12628, doi:10.1073/pnas.0906374106.
34. Israde-Alcántara, I.; Bischoff, J.L.; Domínguez-Vázquez, G.; Li, H.C.; DeCarli, P.S.; Bunch, T.E.; Wittke, J.H.; Weaver, J.C.; Firestone, R.B.; West, A.; et al. Evidence from Central Mexico Supporting the Younger Dryas Extraterrestrial Impact Hypothesis. *Proc. Natl. Acad. Sci. U. S. A.* **2012**, *109*, E738–E747, doi:10.1073/pnas.1110614109.
35. Tankersley, K. Evidence of the Clovis Age Comet at Sheriden Cave, Ohio. In *Midwest Chapter of the Friends of Mineralogy Symposium and Field Conference*; Geology Department of Miami University: Oxford, Ohio, USA, 2009.
36. West, A. Nanodiamonds as Evidence for a Younger Dryas Cosmic Impact Event. *Quat. Int.* **2012**, *279–280*, 531, doi:10.1016/j.quaint.2012.08.1855.
37. Tian, H.; Schryvers, D.; Claeys, P. Nanodiamonds do not Provide Unique Evidence for a Younger Dryas Impact. *Proc. Natl. Acad. Sci. U. S. A.* **2011**, *108*, 40–44, doi:10.1073/pnas.1007695108.
38. van Hoesel, A.; Hoek, W.Z.; Braadbaart, F.; van der Plicht, J.; Pennock, G.M.; Drury, M.R. Nanodiamonds and Wildfire Evidence in the Usselo Horizon Postdate the Allerod-Younger Dryas Boundary. *Proc. Natl. Acad. Sci. U. S. A.* **2012**, *109*, 7648–7653, doi:10.1073/pnas.1120950109.
39. Moore, A.M.T.; Kennett, J.P.; Napier, W.M.; Bunch, T.E.; Weaver, J.C.; LeCompte, M.A.; Victor Adedeji, A.; Kletetschka, G.; Hermes, R.E.; Wittke, J.H.; et al. Abu Hureyra, Syria, Part 2: Additional Evidence Supporting the Catastrophic Destruction of this Prehistoric Village by a Cosmic Airburst ~12,800 Years Ago. *Airburs. Crater. Imp.* **2023**, *1*, 1–36, doi:10.14293/ACI.2023.0002.
40. LeCompte, M.A.; Goodyear, A.C.; Demitroff, M.N.; Batchelor, D.; Vogel, E.K.; Mooney, C.; Rock, B.N.; Seidel, A.W. Independent Evaluation of Conflicting Microspherule Results from Different Investigations of the Younger Dryas Impact Hypothesis. *Proc. Natl. Acad. Sci. U. S. A.* **2012**, *109*, E2960–E2969, doi:10.1073/pnas.1208603109.
41. LeCompte, M.A.; West, A.; Adedeji, A.V.; Demitroff, M.; Witwer, T.; Langenburg, R.A. The Bowser Road Mastodon and the Younger Dryas Impact Hypothesis. In *The Archaeological Recovery of the Bowser Road Mastodon, Orange County, New York*; Gramly, R.M., Ed.; ASAA/Persimmon Press: North Andover, MA, USA, 2017; pp. 57–76.
42. Bunch, T.E.; Hermes, R.E.; Moore, A.M.; Kennett, D.J.; Weaver, J.C.; Wittke, J.H.; DeCarli, P.S.; Bischoff, J.L.; Hillman, G.C.; Howard, G.A.; et al. Very High-Temperature Impact Melt Products as Evidence for Cosmic Airbursts and Impacts 12,900 Years Ago. *Proc. Natl. Acad. Sci. U. S. A.* **2012**, *109*, E1903–E1912, doi:10.1073/pnas.1204453109.
43. Moore, A.M.T.; Kennett, J.P.; Napier, W.M.; Bunch, T.E.; Weaver, J.C.; LeCompte, M.; Adedeji, A.V.; Hackley, P.; Kletetschka, G.; Hermes, R.E.; et al. Evidence of Cosmic Impact at Abu Hureyra, Syria at the Younger Dryas Onset (~12.8 ka): High-Temperature Melting at >2200 °C. *Sci. Rep.* **2020**, *10*, 4185, doi:10.1038/s41598.020.60867.w.
44. Ballard, J.P.; Bijkerk, A.K. Quartz Melt Structures in European Coversands May Support Younger Dryas Extraterrestrial Impact Hypothesis. In *UT Geography Research Symposium 2014 "Mapping Outside the Lines: Geography as a Nexus for Interdisciplinary and Collaborative Research"*; 2014.
45. Wolbach, W.S.; Ballard, J.P.; Mayewski, P.A.; Adedeji, V.; Bunch, T.E.; Firestone, R.B.; French, T.A.; Howard, G.A.; Israde-Alcántara, I.; Johnson, J.R.; et al. Extraordinary Biomass-Burning Episode and Impact Winter Triggered by the Younger Dryas Cosmic Impact ~12,800 Years Ago. 1. Ice Cores and Glaciers. *J. Geol.* **2018**, *126*, 165–184, doi:10.1086/695703.
46. Wolbach, W.S.; Ballard, J.P.; Mayewski, P.A.; Parnell, A.C.; Cahill, N.; Adedeji, V.; Bunch, T.E.; Domínguez-Vázquez, G.; Erlandson, J.M.; Firestone, R.B.; et al. Extraordinary Biomass-Burning Episode and Impact Winter Triggered by the Younger Dryas Cosmic Impact ~12,800 Years Ago. 2. Lake, Marine, and Terrestrial Sediments. *J. Geol.* **2018**, *126*, 185–205, doi:10.1086/695704.
47. Mahaney, W.C.; Kalm, V.; Krinsley, D.H.; Tricart, P.; Schwartz, S.; Dohm, J.; Kim, K.J.; Kapran, B.; Milner, M.W.; Beukens, R.; et al. Evidence from the Northwestern Venezuelan Andes for Extraterrestrial Impact: The Black Mat Enigma. *Geomorphology* **2010**, *116*, 48–57, doi:10.1016/j.geomorph.2009.10.007.
48. Mahaney, W.C.; Keiser, L.; Krinsley, D.H.; Pentlavalli, P.; Allen, C.C.R.; Somelar, P.; Schwartz, S.; Dohm, J.M.; Dirszowsky, R.; West, A.; et al. Weathering Rinds as Mirror Images of Palaeosols: Examples from the Western Alps with Correlation to Antarctica and Mars. *J. Geol. Soc.* **2013**, *170*, 833–847, doi:10.1144/jgs2012.150.
49. Mahaney, W.C.; Krinsley, D.H.; Milner, M.W.; Fischer, R.; Langworthy, K. Did the Black-Mat Impact/Airburst Reach the Antarctic? Evidence from New Mountain Near the Taylor Glacier in the Dry Valley Mountains. *J. Geol.* **2018**, *126*, 285–305, doi:10.1086/697248.
50. Mahaney, W.C.; West, A.; Milan, A.; Krinsley, D.H.; Somelar, P.; Schwartz, S.; Milner, M.W.; Allen, C.C.R. Cosmic Airburst on Developing Allerød Substrates (Soils) in the Western Alps, Mt. Viso Area. *Stud. Quat.* **2018**, *35*, 3–23, doi:10.2478/squa.2018.0001.
51. Mahaney, W.C. The Younger Dryas Boundary (YDB): Terrestrial, Cosmic, or Both? *Int. J. Earth Sci.* **2023**, *112*, 791–804, doi:10.1007/s00531-022-02287-x.
52. Mahaney, W.C.; Keiser, L.; Krinsley, D.; Kalm, V.; Beukens, R.; West, A. New Evidence from a Black Mat Site in the Northern Andes Supporting a Cosmic Impact 12,800 Years Ago. *J. Geol.* **2013**, *121*, 309–325.
53. Mahaney, W.C.; Keiser, L.; Krinsley, D.H.; West, A.; Dirszowsky, R.; Allen, C.C.R.; Costa, P. Recent Developments in the Analysis of the Black Mat Layer and Cosmic Impact at 12.8 ka. *Geogr. Ann. Ser. A* **2014**, *96*, 99–111, doi:10.1111/geoa.12033.
54. Mahaney, W.C.; Krinsley, D.; Kalm, V. Evidence for a Cosmogenic Origin of Fired Glaciofluvial Beds in the Northwestern Andes:

Correlation with Experimentally Heated Quartz and Feldspar. *Sediment. Geol.* **2010**, *231*, 31–40, doi:10.1016/j.sedgeo.2010.08.004.

55. Mahaney, W.C.; Somelar, P. The Encke Comet Impact/Airburst and the Younger Dryas Boundary: Testing the Impossible Hypothesis (YDIH). *Geologos* **2024**, *30*, doi:10.21203/rs.3.rs.2880031/v1.
56. Mahaney, W.C.; Somelar, P.; Allen, C.C.R. Late Pleistocene Glacial-Paleosol-Cosmic Record of the Viso Massif—France and Italy: New Evidence in Support of the Younger Dryas Boundary (12.8 ka). *Int. J. Earth Sci.* **2023**, *112*, 217–242, doi:10.1007/s00531-022-02243-9.
57. Fitzenreiter, R.; Ernstson, K.; Kletetschka, G.; LeCompte, M.A.; Moore, C.R.; Kennett, J.P.; Bizimis, M.; Hofmann, F.; Takac, M.; Adedeji, A.V.; et al. Evidence of a 12,800-Year-Old Shallow Airburst Depression in Louisiana with Large Deposits of Shocked Quartz and Melted Materials. *Airburs. Crater. Imp.* **2025**, *3*, 20250004, doi:10.14293/ACI.2025.0004.
58. Moore, C.R.; LeCompte, M.A.; Kennett, J.P.; Brooks, M.J.; Firestone, R.B.; Ivester, A.H.; Ferguson, T.A.; Lane, C.S.; Duernberger, K.A.; Feathers, J.K.; et al. Platinum, Shock-Fractured Quartz, Microspherules, and Meltglass Widely Distributed in Eastern USA at the Younger Dryas Onset (12.8 ka). *Airburs. Crater. Imp.* **2024**, *2*, 1–31, doi:10.14293/ACI.2024.0003.
59. Moore, C.R.; West, A.; LeCompte, M.A.; Brooks, M.J.; Daniel, I.R., Jr.; Goodyear, A.C.; Ferguson, T.A.; Ivester, A.H.; Feathers, J.K.; Kennett, J.P.; et al. Widespread Platinum Anomaly Documented at the Younger Dryas Onset in North American Sedimentary Sequences. *Sci. Rep.* **2017**, *7*, 44031, doi:10.1038/srep44031.
60. Pino, M.; Abarzúa, A.M.; Astorga, G.; Martel-Cea, A.; Cossio-Montecinos, N.; Navarro, R.X.; Lira, M.P.; Labarca, R.; LeCompte, M.A.; Adedeji, V.; et al. Sedimentary Record from Patagonia, Southern Chile Supports Cosmic-Impact Triggering of Biomass Burning, Climate Change, and Megafaunal Extinctions at 12.8 ka. *Sci. Rep.* **2019**, *9*, 4413, doi:10.1038/s41598-018-38089-y.
61. Boslough, M.; Nicoll, K.; Holliday, V.T.; Daulton, T.L.; Meltzer, D.J.; Pinter, N.; Scott, A.C.; Surovell, T.A.; Claeys, P.; Gill, J.L.; et al. Arguments and Evidence Against a Younger Dryas Impact Event. In *Climates, Landscapes, and Civilizations*; Giosan, L., Fuller, D.Q., Nicoll, K., Flad, R.K., Clift, P.D., Eds.; Geophysical Monograph Series 198; American Geophysical Union: Washington, DC, USA, 2012; pp. 13–26, doi:10.1029/2012GM001209.
62. Holliday, V.T.; Daulton, T.; Bartlein, P.; Boslough, M.B.; Breslawski, R.P.; Fisher, A.; Jorgeson, I.; Scott, A.; Koeberl, C.; Marlon, J.R.; et al. Comprehensive Refutation of the Younger Dryas Impact Hypothesis (YDIH). *Earth Sci. Rev*. **2023**, *247*, 104502, doi:10.1016/j.earscirev.2023.104502.
63. Higgins, M.D.; Lajeunesse, P.; St-Onge, G.; Locat, J.; Duchesne, M.; Ortiz, J.; Sanfaçon, R. Bathymetric and Petrological Evidence for a Young (Pleistocene?) 4-km Diameter Impact Crater in the Gulf of Saint Lawrence, Canada. In *42nd Annual Lunar and Planetary Science Conference*; 2011; 1504.
64. Holcombe, T.L.; Warren, J.S.; Reid, D.F.; Virden, W.T.; Divins, D.L. Small Rimmed Depression in Lake Ontario: An Impact Crater? *J. Gt. Lakes Res.* **2001**, *27*, 510–517, doi:10.1016/S0380.1330(01)70664.8.
65. Spooner, I.; Stevens, G.; Morrow, J.; Pufahl, P.; Grieve, R.; Raeside, R.; Pilon, J.; Stanley, C.; Barr, S.; McMullin, D. Identification of the Bloody Creek Structure, a Possible Impact Crater in Southwestern Nova Scotia, Canada. *Meteorit. Planet. Sci.* **2009**, *44*, 1193–1202, doi:10.1111/j.1945.5100.2009.tb01217.x.
66. Herr, A.A.; Karunatillake, S.; Hood, D.R.; Heinrich, P.; Horn, M.; Webb, A. Investigating the Brushy Creek Suspected Impact Crater, St. Helena Parish, Louisiana. In *52nd Lunar and Planetary Science Conference*; 2021; 2737.
67. Malkova, K.; Kletetschka, G.; West, A.; Bunch, T.; Witke, J. Soil Composition Inside the Possible Crater in Bolivia, Iturralde: Material Implying Impact Event of Low Density Meteorite. In *44th Annual Lunar and Planetary Science Conference*; 2013; pp. 1705.
68. Melosh, H.J. The Australasian Tektite Source Crater: Found at Last? *Proc. Natl. Acad. Sci. U. S. A.* **2020**, *117*, 1252–1253, doi:10.1073/pnas.1920576117.
69. Koeberl, C.; Ferrière, L. Libyan Desert Glass Area in Western Egypt: Shocked Quartz in Bedrock Points to a Possible Deeply Eroded Impact Structure in the Region. *Meteorit. Planet. Sci.* **2019**, *54*, 2398–2408, doi:10.1111/maps.13250.
70. Gilmour, I.; Russell, S.S.; Arden, J.W.; Lee, M.R.; Franchi, I.A.; Pillinger, C.T. Terrestrial Carbon and Nitrogen Isotopic Ratios from Cretaceous-Tertiary Boundary Nanodiamonds. *Science* **1992**, *258*, 1624–1626, doi:10.1126/science.258.5088.1624.
71. Hough, R.M.; Gilmour, I.; Pillinger, C.T.; Langenhorst, F.; Montanari, A.; Koeberl, C. Carbon Isotope Study of Impact Diamonds in Chicxulub Ejecta at Cretaceous–Tertiary Boundary Sites in Mexico and the Western Interior of the United States. In *Large Meteorite Impacts and Planetary Evolution II*; Dressler, B.O., Sharpton, V.L., Eds.; Geological Society of America Special Paper 339; Geological Society of America: Boulder, CO, USA, 2000; pp. 215–222.
72. Kjær, K.H.; Larsen, N.K.; Binder, T.; Bjørk, A.A.; Eisen, O.; Fahnestock, M.A.; Funder, S.; Garde, A.A.; Haack, H.; Helm, V.; et al. A Large Impact Crater Beneath Hiawatha Glacier in Northwest Greenland. *Sci. Adv.* **2018**, *4*, eaar8173, doi:10.1126/sciadv.aar8173.
73. Hyde, W.R.; Garde, A.A.; Keulen, N.; Malkki, S.N.; Jaret, S.J.; Waight, T.; Beck, P.; McDonald, I.; Larsen, N.K. Impact Melt Rocks from the Late Paleocene Hiawatha Impact Structure, Northwest Greenland. *Meteorit. Planet. Sci.* **2023**, *58*, 789–814, doi:10.1111/maps.13987.
74. Yde, J.C.; Anderson, N.J.; Post, E.; Saros, J.E.; Telling, J. Environmental Change and Impacts in the Kangerlussuaq Area, West Greenland. *Arct. Antarct. Alp. Res.* **2018**, *50*, S100001, doi:10.1080/15230430.2018.1433786.
75. Taylor, K.C.; Mayewski, P.A.; Twickler, M.S.; Whitlow, S.I. Biomass Burning Recorded in the GISP2 Ice Core: A Record from Eastern Canada? *Holocene* **1996**, *6*, 1–6, doi:10.1177/095968369600600101.
76. Mayewski, P.A.; Meeker, L.D.; Twickler, M.S.; Whitlow, S.; Yang, Q.; Lyons, W.B.; Prentice, M. Major Features and Forcing of High-Latitude Northern Hemisphere Atmospheric Circulation Using a 110,000-Year-Long Glaciochemical Series. *J. Geophys. Res.* **1997**, *102*, 26345–26366, doi:10.1029/96JC03365.
77. Petrenko, V.V.; Severinghaus, J.P.; Brook, E.J.; Reeh, N.; Schaefer, H. Gas Records from the West Greenland Ice Margin Covering the Last Glacial Termination: A Horizontal Ice Core. *Quat. Sci. Rev.* **2006**, *25*, 865–875.
78. Reeh, N.; Oerter, H.; Thomsen, H.H. Comparison Between Greenland Ice-Margin and Ice-Core Oxygen-18 Records. *Ann. Glaciol.* **2002**, *35*, 136–144, doi:10.3189/172756402781817365.
79. Mayewski, P.A.; Meeker, L.D.; Whitlow, S.; Twickler, M.S.; Morrison, M.C.; Alley, R.B.; Bloomfield, P.; Taylor, K. The Atmosphere During the Younger Dryas. *Science* **1993**, *261*, 195–197, doi:10.1126/science.261.5118.195.
80. MacGregor, J.A.; Fahnestock, M.A.; Colgan, W.T.; Colgan, W.T.; Larsen, N.K.; Kjeldsen, K.K.; Welker, J.M. The Age of Surface-Exposed Ice Along the Northern Margin of the Greenland Ice Sheet. *J. Glaciol.* **2020**, *66*, 667–684, doi:10.1017/jog.2020.62.
81. Rasmussen, S.O.; Seierstad, I.K.; Andersen, K.K.; Bigler, M.; Dahl-Jensen, D.; Johnsen, S.J. Synchronization of the NGRIP, GRIP, and GISP2 Ice Cores Across MIS 2 and Palaeoclimatic Implications. *Quat. Sci. Rev.* **2008**, *27*, 18–28, doi:10.1016/j.quascirev.2007.01.016.
82. Lehmann, M.; Siegenthaler, U. Equilibrium Oxygen- and Hydrogen-Isotope Fractionation Between Ice and Water. *J. Glaciol.* **1991**, *37*, 23–26, doi:10.3189/S0022143000042751.
83. Zielinski, G.A.; Mayewski, P.A.; Meeker, L.D.; Whitlow, S.; Twickler, M.S. A 110,000-yr Record of Explosive Volcanism from the GISP2 (Greenland) Ice Core. *Quat. Res.* **1996**, *45*, 109–118, doi:10.1006/qres.1996.0013.

84. Biscaye, P.E.; Grousset, F.E.; Revel, M.; Van der Gaast, S.; Zielinski, G.A.; Vaars, A.; Kukla, G. Asian Provenance of Glacial Dust (Stage 2) in the Greenland Ice Sheet Project 2 Ice Core, Summit, Greenland. *J. Geophys. Res.* **1997**, *102*, 26765–26781, doi:10.1029/97JC01249.
85. Han, C.; Do Hur, S.; Han, Y.; Lee, K.; Hong, S.; Erhardt, T.; Fischer, H.; Svensson, A.M.; Steffensen, J.P.; Vallelonga, P. High-Resolution Isotopic Evidence for a Potential Saharan Provenance of Greenland Glacial Dust. *Sci. Rep*. **2018**, *8*, 15582, doi:10.1038/s41598-018-33859-0.
86. Bory, A.; Biscaye, P.E.; Grousset, F.E. Two Distinct Seasonal Asian Source Regions for Mineral Dust Deposited in Greenland (NorthGRIP). *Geophys. Res. Lett.* **2003**, *30*, doi:10.1029/2002GL016446.
87. Petaev, M.I.; Huang, S.; Jacobsen, S.B.; Zindler, A. Large Pt Anomaly in the Greenland Ice Core Points to a Cataclysm at the Onset of Younger Dryas. *Proc. Natl. Acad. Sci. U. S. A.* **2013**, *110*, 12917–12920, doi:10.1073/pnas.1303924110.
88. Boslough, M.B. Impact-Induced Climate Change Due to an Orbiting Debris Ring. In *ISDC 2001: The National Space Society's 20 th Annual International Space Development Conference*; 2001.
89. Herr, A.A.; Karunatillake, S.; Hood, D.R.; Heinrich, P.; Horn, M.; Webb, A. Investigating the Brushy Creek Suspected Impact Crater, St. Helena Parish, Louisiana. In *52nd Lunar and Planetary Science Conference*; 2021; 2737.
90. Bunch, T.; et al. *AGU Fall Meeting Abstracts.* PP13C–1476.
91. Schmitt, R.T.; Lapke, C.; Lingemann, C.M.; Siebenschock, M.; Stöffler, D. *Distribution and Origin of Impact Diamonds in the Ries Crater, Germany*; Geological Society of America, 2005; Volume 384, doi:10.1130/0.8137.2384.1.299.
92. Kennett, J.P.; LeCompte, M.A.; Moore, C.R.; Kletetschka, G.; Johnson, J.R.; Wolbach, W.S.; Mitra, S.; Maiorana-Boutilier, A.; Adedeji, V.; Young, M.D.; et al. RETRACTED: Shocked Quartz at the Younger Dryas Onset (12.8 ka) Supports Cosmic Airbursts/Impacts Contributing to North American Megafaunal Extinctions and Collapse of the Clovis Technocomplex. *PLoS One* **2025**, *20*, e0319840, doi:10.1371/journal.pone.0319840.
93. Van Hoesel, A.; Hoek, W.Z.; Pennock, G.M.; Kaiser, K.; Plümper, O.; Jankowski, M.; Hamers, M.F.; Schlaak, N.; Küster, M.; Andronikov, A.V. A Search for Shocked Quartz Grains in the Allerød-Younger Dryas Boundary Layer. *Meteorit. Planet. Sci.* **2015**, *50*, 483–498, doi:10.1111/maps.12435.
94. Moore, A.M.T.; Kennett, J.P.; LeCompte, M.A.; Moore, C.R.; Li, Y.-Q.; Kletetschka, G.; Langworthy, K.; Razink, J.J.; Brogden, V.; van Devener, B.; et al. Abu Hureyra, Syria, Part 1: Shock-Fractured Quartz Grains Support 12,800-Year-Old Cosmic Airburst at the Younger Dryas Onset. *Airburs. Crater. Imp.* **2023**, *1*, 1–28, doi:10.14293/ACI.2023.0003.
95. Ferrière, L.; Morrow, J.R.; Amgaa, T.; Koeberl, C. Systematic Study of Universal-Stage Measurements of Planar Deformation Features in Shocked Quartz: Implications for Statistical Significance and Representation of Results. *Meteorit. Planet. Sci.* **2009**, *44*, 925–940, doi:10.1111/j.1945-5100.2009.tb00778.x.
96. LeCompte, M.A.; Collins, S.; Silvia, P.J.; Kletetschka, G.; Witwer, T.; Hermes, R.E.; Moore, C.R.; Wolbach, W.S.; Howard, G.A.; Adedeji, A.V.; et al. A Tunguska Sized Airburst Destroyed Tall el-Hammam a Middle Bronze Age City in the Jordan Valley Near the Dead Sea (Expanded). *Airburst. Crater. Imp*. **2025**, *3*(1), 20250003.
97. Moore, A.M.T.; Kennett, J.P.; Napier, W.M.; Bunch, T.E.; Weaver, J.C.; LeCompte, M.A.; Adedeji, A.V.; Kletetschka, G.; Hermes, R.E.; Wittke, J.H.; et al. Abu Hureyra, Syria, Part 2: Additional Evidence Supporting the Catastrophic Destruction of this Prehistoric Village by a Cosmic Airburst ~12,800 Years Ago, Supplementary Data. *Zenodo. org* **2023**, 1–25.
98. West, A.; Young, M.D.; Costa, L.; Kennett, J.P.; Moore, C.R.; LeCompte, M.A.; Kletetschka, G.; Hermes, R.E. Modeling Airbursts by Comets, Asteroids, and Nuclear Detonations: Shock Metamorphism, Meltglass, and Microspherules. *Airburst. Crater. Imp.* **2024**, *2*, 1–30.
99. Hamers, M.F.; Drury, M.R. Scanning Electron Microscope-Cathodoluminescence (SEM-CL) Imaging of Planar Deformation Features and Tectonic Deformation Lamellae in Quartz. *Meteorit. Planet. Sci.* **2011**, *46*, 1814–1831, doi:10.1111/j.1945-5100.2011.01295.x.
100. Hamers, M.F. *Identifying Shock Microstructures in Quartz from Terrestrial Impacts: New Scanning Electron Microscopy Methods*; UU Department of Earth Sciences, 2013.
101. Hamers, M.F.; Pennock, G.M.; Herwegh, M.; Drury, M.R. Distinction Between Amorphous and Healed Planar Deformation Features in Shocked Quartz Using Composite Color Scanning Electron Microscope Cathodoluminescence (SEM-CL) Imaging. *Meteorit. Planet. Sci.* **2016**, *51*, 1914–1931, doi:10.1111/maps.12711.
102. Hamers, M.F.; Pennock, G.M.; Drury, M.R. Scanning Electron Microscope Cathodoluminescence Imaging of Subgrain Boundaries, Twins and Planar Deformation Features in Quartz. *Phys. Chemf. Minerals* **2017**, *44*, 263–275, doi:10.1007/s00269.016.0858.x.
103. Kieffer, S.W.; Phakey, P.P.; Christie, J.M. Shock Processes in Porous Quartzite: Transmission Electron Microscope Observations and Theory. *Contr. Mineral. Petrol.* **1976**, *59*, 41–93, doi:10.1007/BF00375110.
104. Wakita, S.; Johnson, B.C.; Denton, C.A.; Davison, T.M. Jetting During Oblique Impacts of Spherical Impactors. *Icarus* **2021**, *360*, 114365, doi:10.1016/j.icarus.2021.114365.
105. Ernstson, K. Meteorite Impact Spallation: From Mega- to Micro-Scale. 2014. Available online: https://www.impact-structures.com/impact-educational/meteorite-impact-spallation-from-mega-to-micro-scale/.
106. Ernstson, K. Shock Metamorphism. 2020. Available online: https://www.impact-structures.com/shock-metamorphism-page/.
107. Ernstson, K. Evidence of Meteorite Impact-Induced Thermal Shock in Quartz. In *Modern Problems of Theoretical, Experimental and Applied Mineralogy, Yushkin Readings*; 2020; pp. 361–362.
108. Schmieder, M.; Reimold, W.U.; Buchner, E.; Khirfan, M.; Salameh, E.; Khoury, H. Shock-Metamorphic Microfeatures in Chert from the Jebel Waqf as Suwwan Impact Structure, Jordan. *Meteorit. Planet. Sci*. **2011**, *46*, 574–586, doi:10.1111/j.1945-5100.2011.01175.x.
109. Hermes, R.E.; Wenk, H.-R.; Kennett, J.P.; Bunch, T.E.; Moore, C.R.; LeCompte, M.A.; Kletetschka, G.; Victor Adedeji, A. Langworthy, K.; Razink, J.J.; et al. Microstructures in Shocked Quartz: Linking Nuclear Airbursts and Meteorite Impacts. *Airburs. Crater. Imp.* **2023**, *1*, 1–40, doi:10.14293/ACI.2023.0001.
110. French, B.M. *Traces of Catastrophe: A Handbook of Shock-Metamorphic Effects in Terrestrial Meteorite Impact Structures*; Lunar and Planetary Institute, 1998; pp. 120.
111. French, B.M.; Koeberl, C. The Convincing Identification of Terrestrial Meteorite Impact Structures: What Works, what Doesn't, and Why. *Earth Sci. Rev.* **2010**, *98*, 123–170, doi:10.1016/j.earscirev.2009.10.009.
112. Heaney, P.J. Structure and Chemistry of the Low-Pressure Silica Polymorphs. *Rev. Mineral. Geochem.* **1994**, *29*, 1–40, doi:10.1515/9781501509698.
113. Stöffler, D.; Ewald, U.; Ostertag, R.; Reimold, W. Research Drilling Noerdlingen 1973 (Ries): Composition and Texture of Polymict Impact Breccias. *Geol. Bavarica* **1977**, *75*, 443–458.
114. Kring, D.A. The Chicxulub Impact Event and its Environmental Consequences at the Cretaceous–Tertiary Boundary. *Palaeogeogr. Palaeoclimatol. Palaeoecol.* **2007**, *255*, 4–21, doi:10.1016/j.palaeo.2007.02.037.
115. Masaitis, V.L. Popigai Crater: Origin and Distribution of Diamond-Bearing Impactites. *Meteorit. Planet. Sci*. **1998**, *33*, 349–359, doi:10.1111/j.1945-5100.1998.tb01639.x.

116. Cas, R.; Wright, J. *Volcanic Successions Modern and Ancient: A Geological Approach to Processes, Products and Successions*; Springer Science & Business Media, 2012.
117. Fisher, R.V.; Schmincke, H.-U. *Pyroclastic Rocks*; Springer: Berlin, Heidelberg, Germany, 1984; pp. 383–409, doi:10.1007/978-3-642-74864-6.
118. Sibson, R.H. Fault Rocks and Fault Mechanisms. *J. Geol. Soc.* **1977**, *133*, 191–213, doi:10.1144/gsjgs.133.3.0191.
119. Swanson, M.T. Fault Structure, Wear Mechanisms and Rupture Processes in Pseudotachylyte Generation. *Tectonophysics* **1992**, *204*, 223–242, doi:10.1016/0040-1951(92)90309-T.
120. Uman, M.A. *The Lightning Discharge*; Courier Corporation, 2001.
121. Genge, M.J.; Davies, B.; Suttle, M.D.; van Ginneken, M.; Tomkins, A.G. The Mineralogy and Petrology of I-Type Cosmic Spherules: Implications for Their Sources, Origins and Identification in Sedimentary Rocks. *Geochim. Cosmochim. Acta* **2017**, *218*, 167–200, doi:10.1016/j.gca.2017.09.004.
122. Genge, M.J.; Engrand, C.; Gounelle, M.; Taylor, S. The Classification of Micrometeorites. *Meteorit. Planet. Sci.* **2008**, *43*, 497–515, doi:10.1111/j.1945-5100.2008.tb00668.x.
123. Genge, M.J.; Grady, M.M. The Fusion Crusts of Stony Meteorites: Implications for the Atmospheric Reprocessing of Extraterrestrial Materials. *Meteorit. Planet. Sci.* **1999**, *34*, 341–356, doi:10.1111/j.1945-5100.1999.tb01344.x.
124. Genge, M.J.; Grady, M.M.; Hutchison, R. The Textures and Compositions of Fine-Grained Antarctic Micrometeorites: Implications for Comparisons with Meteorites. *Geochim. Cosmochim. Acta* **1997**, *61*, 5149–5162, doi:10.1016/S0016-7037(97)00308-6.
125. Scott, A.C.; Pinter, N.; Collinson, M.E.; Hardiman, M.; Anderson, R.S.; Brain, A.P.R.; Smith, S.Y.; Marone, F.; Stampanoni, M. Fungus, not Comet or Catastrophe, Accounts for Carbonaceous Spherules in the Younger Dryas "Impact Layer". *Geophys. Res. Lett.* **2010**, *37*, 1–5, doi:10.1029/2010GL043345.
126. Legrand, M.; De Angelis, M.; Staffelbach, T.; Neftel, A.; Stauffer, B. Large Perturbations of Ammonium and Organic Acids Content in the Summit-Greenland Ice Core. Fingerprint from Forest Fires? *Geophys. Res. Lett.* **1992**, *19*, 473–475, doi:10.1029/91GL03121.
127. Fischer, H.; Schüpbach, S.; Gfeller, G.; Bigler, M.; Röthlisberger, R.; Erhardt, T.; Stocker, T.F.; Mulvaney, R.; Wolff, E.W. Millennial Changes in North American Wildfire and Soil Activity Over the Last Glacial Cycle. *Nat. Geosci.* **2015**, *8*, 723–727, doi:10.1038/ngeo2495.
128. Barnes, S.J.; Naldrett, A.J.; Gorton, M.P. The Origin of the Fractionation of Platinum-Group Elements in Terrestrial Magmas. *Chem. Geol.* **1985**, *53*, 303–323, doi:10.1016/0009-2541(85)90076-2.
129. Peucker-Ehrenbrink, B.; Jahn, B.m. Rhenium-Osmium Isotope Systematics and Platinum Group Element Concentrations: Loess and the Upper Continental Crust. *Geochem. Geophys. Geosyst.* **2001**, *2*, doi:10.1029/2001GC000172.
130. Alvarez, L.; Alvarez, W.; Asaro, F.; Michel, H. Extraterrestrial Cause for the Cretaceous-Tertiary Extinction. *Science* **1980**, *208*, 1095–1108, doi:10.1126/science.208.4448.1095.
131. Lodders, K. Solar System Abundances and Condensation Temperatures of the Elements. *Astrophysical. J.* **2003**, *591*, 1220–1247, doi:10.1086/375492.
132. Palme, H. Meteorites and Their Components. *Geochem. Perspect.* **2018**, *7*, 49–66.
133. Palme, H.; Hutcheon, I.D.; Spettel, B. Composition and Origin of Refractory-Metal-Rich Assemblages in a Ca, Al-Rich Allende Inclusion. *Geochim. Cosmochim. Acta* **1994**, *58*, 495–513, doi:10.1016/0016-7037(94)90479-0.
134. Moore, C.R.; Brooks, M.J.; Goodyear, A.C.; Ferguson, T.A.; Perrotti, A.G.; Mitra, S.; Listecki, A.M.; King, B.C.; Mallinson, D.J.; Lane, C.S.; et al. Sediment Cores from White Pond, South Carolina, Contain a Platinum Anomaly, Pyrogenic Carbon Peak, and Coprophilous Spore Decline at 12.8 ka. *Sci. Rep*. **2019**, *9*, 15121, doi:10.1038/s41598.019.51552.8.
135. Gabrielli, P.; Barbante, C.; Plane, J.M.; Varga, A.; Hong, S.; Cozzi, G.; Gaspari, V.; Planchon, F.A.; Cairns, W.; Ferrari, C.; et al. Meteoric Smoke Fallout Over the Holocene Epoch Revealed by Iridium and Platinum in Greenland Ice. *Nature* **2004**, *432*, 1011–1014, dot:10.1038/nature03137.
136. Lanci, L.; Delmonte, B.; Salvatore, M.C.; Baroni, C. Insight Into Provenance and Variability of Atmospheric Dust in Antarctic Ice Cores During the Late Pleistocene from Magnetic Measurements. *Front. Earth Sci.* **2020**, *8*, 258, doi:10.3389/feart.2020.00258.
137. Vajda, V.; Nehzati, S.; Kenny, G.; Bermúdez, H.D.; Krüger, A.; Björling, A.; Ocampo, A.; Cui, Y.; Sigfridsson Clauss, K.G.V. Nanoparticles of Iridium and other Platinum Group Elements Identified in Chicxulub Asteroid Impact Spherules–Implications for Impact Winter and Profound Climate Change. *Glob. Planet. Change* **2025**, *245*, 104659, doi:10.1016/j.gloplacha.2024.104659.
138. Glikson, A.Y. Identification of Impact Structures. In *The Asteroid Impact Connection of Planetary Evolution: With Special Reference to Large Precambrian and Australian Impacts*; Springer: Dordrecht, The Netherlands, 2013; pp. 35–47.
139. Berezhnaya, E.; Dubinin, A. Platinum Group Element Geochemistry in the Ocean. *Geochem. Int.* **2024**, *62*, 327–343, doi:10.1134/S0016702923700106.
140. Rudnick, R.L.; Gao, S. Composition of the Continental Crust. In *Treatise on Geochemistry*; Rudnick, R.L., Ed.; Elsevier: Oxford, UK, 2003; pp. 1–64, doi:10.1016/B0-08-043751-6/03016-4.
141. Anders, E.; Grevesse, N. Abundances of the Elements: Meteoritic and Solar. *Geochim. Cosmochim. Acta* **1989**, *53*, 197–214, doi:10.1016/0016.7037(89)90286.X.
142. McDonough, W.F.; Sun, S.-s. The Composition of the Earth. *Chem. Geol*. **1995**, *120*, 223–253, doi:10.1016/0009-2541(94)00140-4.
143. Becker, H.; Horan, M.F.; Walker, R.J.; Gao, S.; Lorand, J.-P.; Rudnick, R.L. Highly Siderophile Element Composition of the Earth's Primitive Upper Mantle: Constraints from New Data on Peridotite Massifs and Xenoliths. *Geochim. Cosmochim. Acta* **2006**, *70*, 4528–4550, doi:10.1016/j.gca.2006.06.004.
144. Walker, R.J. Siderophile Elements in Tracing Planetary Formation and Evolution. *Geochem. Perspect.* **2016**, *5*, 1–145, doi:10.7185/geochempersp.5.1.
145. Walker, R.; Horan, M.; Shearer, C.; Papike, J. *Lunar and Planetary Science Conference*; 1579.
146. Horan, M.F.; Walker, R.J.; Morgan, J.W.; Grossman, J.N.; Rubin, A.E. Highly Siderophile Elements in Chondrites. *Chem. Geol.* **2003**, *196*, 27–42. doi:10.1016/S0009-2541(02)00405-9.
147. Boslough, M. Computational Modeling of Low-Altitude Airbursts. In *AGU Fall Meeting Abstracts, #U21E-03*; 2007.
148. Artemieva, N.; Shuvalov, V. Atmospheric Shock Waves after Impacts of Cosmic Bodies up to 1000 m in Diameter. *Meteorit. Planet. Sci.* **2019**, *54*, 592–608, doi:10.1111/maps.13229.
149. Collins, G.S.; Lynch, E.; McAdam, R.; Davison, T.M. A Numerical Assessment of Simple Airblast Models of Impact Airbursts. *Meteorit. Planet. Sci.* **2017**, *52*, 1542–1560, doi:10.1111/maps.12873.
150. Marcus, R.; Melosh, H.J.; Collins, G.S. Earth Impact Effects Program. 2004. Available online: https://impact.ese.ic.ac.uk/ImpactEarth/ImpactEffects/.
151. Collins, G.S.; Melosh, H.J.; Marcus, R.A. Earth Impact Effects Program: A Web-Based Computer Program for Calculating the Regional Environmental Consequences of a Meteoroid Impact on Earth. *Meteorit. Planet. Sci*. **2005**, *40*, 817–840, doi:10.1111/j.1945-5100.2005.tb00157.x.
152. Pierazzo, E.; Melosh, H.J. Understanding Oblique Impacts from Experiments, Observations, and Modeling. *Annu. Rev. Earth Planet. Sci.* **2000**, *28*, 141–167, doi:10.1146/annurev.earth.28.1.141.

153. Robertson, D.K.; Mathias, D.L. Hydrocode Simulations of Asteroid Airbursts and Constraints for Tunguska. *Icarus* **2019**, *327*, 36–47, doi:10.1016/j.icarus.2018.10.017.
154. Deller, J.F.; Lowry, S.C.; Snodgrass, C.; Price, M.C.; Sierks, H. A New Approach to Modelling Impacts on Rubble Pile Asteroid Simulants. *Mon. Not. R. Astron. Soc.* **2016**, *455*, 3752–3762, doi:10.1093/mnras/stv2584.
155. Sherburn, J.A.; Horstemeyer, M.F. Hydrodynamic Modeling of Impact Craters in Ice. *Int. J. Impact Eng.* **2010**, *37*, 27–36, doi:10.1016/j.ijimpeng.2009.07.001.
156. Pierazzo, E.; Collins, G. *Cratering in Marine Environments and on Ice*; Springer, 2004; pp. 323–340.
157. Miljković, K.; Jones, A.P.; Price, M.C. High Velocity Impact Modelling of Ice Into Ice: Application to Outer Solar System Landers and Penetrators. In *European Planetary Science Congress Abstracts*; 2010; Volume 5, pp. 321.
158. Silber, E.A.; Johnson, B.C.; Bjonnes, E.; MacGregor, J.A.; Larsen, N.K.; Wiggins, S.E. Effect of Ice Sheet Thickness on Formation of the Hiawatha Impact Crater. *Earth Planet. Sci. Lett.* **2021**, *566*, 116972, doi:10.1016/j.epsl.2021.116972.
159. Ruth, U.; Wagenbach, D.; Steffensen, J.P.; Bigler, M. Continuous Record of Microparticle Concentration and Size Distribution in The Central Greenland Ngrip Ice Core During the Last Glacial Period. *J. Geophys. Res. Atmos.* **2003**, *108*, doi:10.1029/2002JD002376.
160. Kring, D.A.; Durda, D.D. Trajectories and Distribution of Material Ejected from the Chicxulub Impact Crater: Implications for Postimpact Wildfires. *J. Geophys. Res. Planets* **2002**, *107*, 6–1–6–22, doi:10.1029/2001JE001532.
161. Bohor, B.F. *Global Catastrophes in Earth History: An Interdisciplinary Conference on Impacts, Volcanism, and Mass Mortality*; Sharpton, V.L., Ward, P.D., Eds.; Geological Society of America, 1990.
162. Bohor, B.F.; Modreski, P.J.; Foord, E.E. Shocked Quartz in the Cretaceous-Tertiary Boundary Clays: Evidence for a Global Distribution. *Science* **1987**, *236*, 705–709, doi:10.1126/science.236.4802.705.
163. Alvarez, W.; Claeys, P.; Kieffer, S.W. Emplacement of Cretaceous-Tertiary Boundary Shocked Quartz from Chicxulub Crater. *Science* **1995**, *269*, 930–935, doi:10.1126/science.269.5226.930.
164. Johnson, B.C.; Melosh, H.J. Formation of Spherules in Impact Produced Vapor Plumes. *Icarus* **2012**, *217*, 416–430, doi:10.1016/j.icarus.2011.11.020.
165. Johnson, B.C.; Melosh, H.J. Impact Spherules as a Record of an Ancient Heavy Bombardment of Earth. *Nature* **2012**, *485*, 75–77, doi:10.1038/nature10982.
166. Shuvalov, V.; Dypvik, H. Distribution of Ejecta from Small Impact Craters. *Meteorit. Planet. Sci.* **2013**, *48*, 1034–1042, doi:10.1111/maps.12127.
167. Glass, B.P.; Pizzuto, J.E. Geographic Variation in Australasian Microtektite Concentrations: Implications Concerning the Location and Size of the Source Crater. *J. Geophys. Res. Planets* **2012**, *99*, 19075–19081, doi:10.1029/94je01866.
168. Glass, B.P.; Simonson, B.M. Distal Impact Ejecta Layers: Spherules and More. *Elements* **2012**, *8*, 43–48, doi:10.2113/gselements.8.1.43.
169. Glass, B.P.; Simonson, B.M. Modeling Variations in Distal Impact Ejecta/Spherule Layers Through Space and Time. In *Distal Impact Ejecta Layers: A Record of Large Impacts in Sedimentary Deposits*; Springer: Berlin, Heidelberg, Germany, 2013; pp. 533–594.
170. Simonson, B.M.; Glass, B.P. Spherule Layers—Records of Ancient Impacts. *Annu. Rev. Earth Planet. Sci.* **2004**, *32*, 329–361, doi:10.1146/annurev.earth.32.101802.120458.
171. Glass, B.; Wu, J. Coesite and Shocked Quartz Discovered in the, Australasian and North American, Microtektite Layers. *Geology* **1993**, *21*, 435–438, doi:10.1130/0091.7613(1993)021[[0435:CASQDI]]2.3.CO;2.
172. Folco, L.; Perchiazzi, N.; D'Orazio, M.; Frezzotti, M.L.; Glass, B.P.; Rochette, P. Shocked Quartz and other Mineral Inclusions in Australasian Microtektites. *Geology* **2010**, *38*, 211–214, doi:10.1130/G30512.1.
173. Senel, C.B.; Kaskes, P.; Temel, O.; Vellekoop, J.; Goderis, S.; DePalma, R.; Prins, M.A.; Claeys, P.; Karatekin, Ö. Chicxulub Impact Winter Sustained by Fine Silicate Dust. *Nat. Geosci.* **2023**, *16*, 1033–1040, doi:10.1038/s41561-023-01290-4.
174. Wolbach, W.S.; Gilmour, I.; Anders, E. Major Wildfires at the Cretaceous/Tertiary Boundary. *Geol. Soc. Am. Spec. Pap.* **1990**, *247*, 391–400, doi:10.1130/SPE247.p391.
175. Wolbach, W.S.; Gilmour, I.; Anders, E.; Orth, C.J.; Brooks, R.R. Global Fire at the Cretaceous-Tertiary Boundary. *Nature* **1988**, *335*, 744, doi:10.1038/335744e0.
176. Lewis, R.S.; Anders, E. Cretaceous Extinctions: Evidence for Wildfires and Search for Meteoritic Material. *Science* **1985**, *230*, 167–170, doi:10.1126/science.230.4722.167.
177. Nana Yobo, L.; Brandon, A.D.; O'Brien, S.; Halligan, J.J.; Waters, M.R. Volcanic Forcing of Global Climate Cooling at the Younger Dryas Onset Preserved in North American Sediments. *Sci. Adv.* **2026**, *12*, eaec9030, doi:10.1126/sciadv.aec9030
178. Peucker-Ehrenbrink, B.; Ravizza, G.; Winckler, G. Geochemical Tracers of Extraterrestrial Matter in Sediments. *Elements* **2016**, *12*, 191–196, doi:10.2113/gselements.12.3.191.
179. Sharma, M.; Chen, C.; Jackson, B.P.; Abouchami, W. High-Resolution Osmium Isotopes in Deep-Sea Ferromanganese Crusts Reveal a Large Meteorite Impact in the Central Pacific at 12 ± 4 ka. In *AGU Fall Meeting Abstracts*; 2009; pp. PP13B-1454.
180. Brownlee, D.E.; Bates, B.A.; Wheelock, M.M. Extraterrestrial Platinum Group Nuggets in Deep-Sea Sediments. *Nature* **1984**, *309*, 693–695, doi:10.1038/309693a0.
181. Wasson, J.T.; Kallemeyn, G.W.; Runcorn, S.K.; Turner, G.; Woolfson, M.M. Compositions of Chondrites. *Phil. Trans. R. Soc. Lond. A Math. Phys. Sci.* **1988**, *325*, 535–544, doi:10.1098/rsta.1988.0066.
182. Simonson, B.M.; McDonald, I.; Shukolyukov, A.; Koeberl, C.; Reimold, W.U.; Lugmair, G.W. Geochemistry of 2.63–2.49 Ga Impact Spherule Layers and Implications for Stratigraphic Correlations and Impact Processes. *Precambrian Res.* **2009**, *175*, 51–76, doi:10.1016/j.precamres.2009.08.004.

Appendix

To evaluate the stratigraphic distribution of impact-related proxies across the Greenland section, we compiled depth-resolved measurements of isotopic composition ($\delta^{18}O$) and multiple high-temperature and shock-related indicators, including nanodiamonds, microspherules, shocked quartz, meltglass, carbon spherules, glasslike carbon, and lithic aggregates (Appendix Figure A1). These datasets provide a multi-proxy framework for identifying intervals of anomalous deposition and for assessing whether the Younger Dryas Boundary (YDB) signal reflects a discrete event or background variability.

By presenting all proxies on a common depth scale, this table allows direct comparison of proxy abundance peaks with climatic transitions recorded by $\delta^{18}O$, facilitating evaluation of synchronicity among independent indicators.

The datasets reveal a pronounced clustering of several proxies within a narrow depth interval (~5.2–5.6 m), corresponding to the Younger Dryas Boundary (YDB). Outside this interval, most proxies are absent or occur at background levels, suggesting that the observed enrichment is stratigraphically localized rather than continuous.

The combined proxy dataset shows a clear and coherent stratigraphic pattern. Most high-temperature and shock-related proxies are either absent or present at low background levels throughout the section but exhibit a pronounced and co-occurring peak within a restricted depth interval centered at ~5.2–5.6 m. This interval includes elevated abundances of nanodiamonds, carbon spherules, glasslike carbon, meltglass, and lithic aggregates, along with the appearance of shocked quartz and Fe-Si spherules.

The co-occurrence of these proxies is significant because they represent independent indicators of extreme thermal and/or pressure conditions. Their simultaneous enrichment within a narrow stratigraphic horizon argues against gradual climatic or sedimentary processes and instead supports a short-duration depositional event. The absence of comparable peaks elsewhere in the section further reinforces this interpretation.

In contrast, the $\delta^{18}O$ record shows broader variability across the profile, reflecting longer-term climatic changes rather than discrete events. The alignment of the proxy-rich interval with a shift in $\delta^{18}O$ values indicates that the depositional event occurred near the onset of the Younger Dryas but is not simply a function of climate-driven dust variability.

The data indicate that the Greenland section records a transient influx of high-temperature and shock-related materials superimposed on background atmospheric deposition. This stratigraphically confined, multi-proxy enrichment is consistent with a discrete event capable of generating and dispersing a diverse suite of impact-related materials.

$\delta^{18}O$	
Dist. (m)	‰
2.90	-31.9
3.10	-32.0
3.30	-31.9
3.50	-32.2
3.90	-31.3
4.10	-33.0
4.30	-32.5
4.50	-31.8
4.70	-32.8
4.90	-33.3
5.10	-31.8
5.30	-31.7
5.50	-32.1
5.70	-31.9
5.90	-31.9
6.10	-32.5
6.30	-31.9
6.50	-32.8
6.70	-33.8
6.90	-33.0
7.10	-32.9
7.30	-31.8
7.50	-32.1
7.70	-33.5
7.90	-33.5
8.10	-32.0
8.30	-32.3
8.50	-33.7

Glass-filled Quartz	
Dist. (m)	#/kg
5.2	0
5.3	0
5.5	65.0
5.6	7.0
5.8	0
6.1	0

Nanodiamonds	
Dist. (m)	10^6/mL
3.22	0
3.67	0.00679
3.97	0
4.27	0
4.72	0
5.02	0.00054
5.17	0.00529
5.32	0.00052
5.48	1414.73
5.63	56.9830
5.78	0.00012
5.93	0.00069
6.08	0.00113
6.23	0.00063
6.38	0.00117
6.68	0
6.98	0.00059
7.43	0.00008

Meltglass	
Dist. (m)	#/kg
3.7	0
4.3	0
5.2	0
5.3	0
5.5	43.0
5.6	7.0
5.8	0
6.1	0
7.0	0
7.4	0

Spherules, Fe and Si	
Dist. (m)	#/kg
3.67	12
4.27	0
5.17	0
5.32	0
5.48	34
5.63	14
5.78	0
6.23	8
6.98	0
7.43	5

Shocked Quartz	
Dist. (m)	#/kg
3.7	0
4.3	0
5.2	0
5.3	0
5.5	47
5.6	7
5.8	0
6.1	0
7.0	0
7.4	0

Lithic Aggregates	
Dist. (m)	#/kg
3.7	0
4.3	0
5.2	0
5.3	0
5.5	68.0
5.6	14.0
5.8	0
6.1	0
7.0	0
7.4	0

Carbon Spherules	
Dist. (m)	#/kg
3.22	0
3.67	0
4.27	0
5.02	0
5.17	100
5.32	560
5.48	640
5.63	360
5.78	320
5.93	280
6.08	160
6.23	160
6.38	0
6.98	0
7.43	0

Glasslike Carbon	
Dist. (m)	#/kg
3.2	0
3.7	0
4.3	0
5.0	0
5.2	0
5.3	5
5.5	155
5.6	14
5.8	0
5.9	5
6.1	0
6.2	0
6.4	0
7.0	0
7.4	0

Appendix Figure A1: Depth distributions of $\delta^{18}O$ and multiple impact-related proxies from the Greenland section. Columns list sample depth (m) and measured values for each proxy, including nanodiamonds (10^6/mL), spherules (Fe- and Si-rich; #/kg), carbon spherules (#/kg), shocked quartz (#/kg), meltglass (#/kg), glasslike carbon (#/kg), glass-filled quartz (#/kg), and lithic aggregates (#/kg).